

**SPECTROSCOPIC AND THEORETICAL INVESTIGATION OF
SELECTED CYCLIC AND BICYCLIC MOLECULES IN THEIR
GROUND AND EXCITED ELECTRONIC STATES**

A Dissertation

by

MOHAMED ZUHAIR MOHAMED RISHARD

Submitted to the Office of Graduate Studies of
Texas A&M University
in partial fulfillment of the requirements for the degree of

DOCTOR OF PHILOSOPHY

December 2007

Major Subject: Chemistry

**SPECTROSCOPIC AND THEORETICAL INVESTIGATION OF
SELECTED CYCLIC AND BICYCLIC MOLECULES IN THEIR
GROUND AND EXCITED ELECTRONIC STATES**

A Dissertation

by

MOHAMED ZUHAIR MOHAMED RISHARD

Submitted to the Office of Graduate Studies of
Texas A&M University
in partial fulfillment of the requirements for the degree of

DOCTOR OF PHILOSOPHY

Approved by:

Chair of Committee,
Committee Members,

Head of Department,

Jaan Laane
Paul S. Cremer
Robert R. Lucchese
George W. Kattawar
David H. Russell

December 2007

Major Subject: Chemistry

ABSTRACT

Spectroscopic and Theoretical Investigation of Selected Cyclic and Bicyclic Molecules
in Their Ground and Excited Electronic States. (December 2007)

Mohamed Zuhair Mohamed Rishard, B.S., University of Colombo, Sri Lanka

Chair of Advisory Committee: Dr. Jaan Laane

The structures, vibrational frequencies, and potential energy functions of several molecules in their ground and excited electronic states were determined using various spectroscopic and theoretical methods.

High-level *ab initio* and density functional theory (DFT) calculations were utilized to investigate the previously reported structures and vibrational spectra of 1,3-disilacyclobutane (13DSCB) and its 1,1,3,3- d_4 (13DSCB- d_4) isotopomer. These calculations confirmed the finding from earlier microwave work that the CSiC angles of the 13DSCB ring are unexpectedly larger than the SiCSi angles. The calculated vibrational spectra using density functional theory agreed well with the experimental data and showed CH₂ modes to have unusually low values. The calculations also confirmed that the individual molecules in the vapor phase are puckered whereas in the solid they become planar.

The one-dimensional potential energy surfaces (PESs) for the ring inversion vibration of 2-cyclohexen-1-one and its 2,6,6- d_3 isotopomer in its ground and singlet S₁(n,π^{*}) electronic states were determined using ultraviolet cavity ringdown spectroscopy (CRDS). The CRDS data allowed several of the quantum states of the ring inversion vibration to be determined for both the ground and excited electronic states, and the data were fit very well with PESs with high barriers to inversion. The infrared and Raman spectra and DFT calculations were utilized to complete a vibrational assignment of 2CHO and 2CHO- d_3 . A remarkable agreement was seen between the experimental and calculated spectra.

The fluorescence excitation spectra (FES) and the single-vibronic level fluorescence (SVLF) spectra of jet-cooled 1,4-dihydronaphthalene (14DHN) were

acquired to determine its ring-puckering potential energy function for the ground and singlet $S_1(\pi, \pi^*)$ electronic states. Ultraviolet, infrared, and Raman spectra were also recorded to complement the analysis. The potential energy functions showed that the molecule is planar in both the ground and $S_1(\pi, \pi^*)$ states. A complete vibrational assignment was carried out for 14DHN using the infrared and Raman data and aided by DFT calculations.

The *ab initio* calculations carried out on 2-methyl-2-cyclopenten-1-one (2MCP) showed that the molecule can have 3 different conformers. Infrared and Raman spectra of the liquid-phase molecule were recorded and analyzed to complement the theoretical calculations.

DEDICATION

To the Almighty, the most beneficent, and the most merciful.

ACKNOWLEDGEMENTS

I would like to acknowledge the following people without whom this work wouldn't have been possible.

First and foremost, I must show my sincere gratitude to my research advisor Professor Jaan Laane for all of his support, patience and insight. He has been a wonderful mentor and I consider that it's been a great honor to have been a student of his. Also, I like to thank Professors Paul Cremer, Robert Lucchese, and George Kattawar for serving as members of my Ph.D. committee.

There were several research associates who deserve my sincere appreciation. They are Dr. Martin Wagner, who recorded the LIF spectra for 14DHN, Professor Stephen Drucker of the University Wisconsin, who acquired the cavity ringdown spectra of 2CHO, Professor Jaeboom Choo, who carried out *ab initio* calculations to complement some of the experimental data presented here, and Dr. Lisa M. Perez who taught me the principles of computational chemistry. I also enjoyed working with the former and current members of the research group of Dr. Laane, namely Dr. Abdulaziz Al-Saadi, Dr. Juan Yang, Dr. Daniel Autrey, and Kathleen McCann. I must also not forget Mrs. Linda Redd who helped me correct my papers and articles.

Last but not least, I cannot forget my beloved wife Minna and my daughter Asma whose sacrifices were a reason for this work to be completed. My parents also made a great contribution to this work by encouraging me with their words of support, and I must show my heartfelt gratitude to them too.

TABLE OF CONTENTS

	Page
ABSTRACT	iii
DEDICATION.....	v
ACKNOWLEDGEMENTS.....	vi
TABLE OF CONTENTS	vii
LIST OF TABLES.....	xi
LIST OF FIGURES	xiii
 CHAPTER	
I INTRODUCTION	1
1,3-Disilacyclobutane	3
2-Cyclohexen-1-one	3
1,4-Dihydronaphthalene	4
2-Methyl-2-cyclopenten-1-one.....	5
II EXPERIMENTAL METHODS	6
Infrared and Raman spectroscopy	6
Jet-cooled laser-induced fluorescence (LIF) spectroscopy ...	9
Electronic absorption spectroscopy	10
Cavity ringdown spectroscopy	10
III THEORETICAL METHODS	12
Introduction	12
Computational chemistry.....	12
Kinetic and potential energy operators.....	14
The kinetic energy operator	15
The potential energy operator.....	17

CHAPTER	Page
IV	VIBRATIONAL SPECTRA AND THEORETICAL CALCULATIONS OF 1,3-DISILACYCLOBUTANE 19
	Introduction 19
	Experimental..... 19
	Computations..... 20
	Structure of 13DSCB..... 20
	Assignment of spectra 23
	Anomalous CH ₂ wagging and twisting frequencies 34
	Structural conversion in the solid phase 36
	Conclusions 43
V	EXPERIMENTAL AND CALCULATED VIBRATIONAL FREQUENCIES OF THE ELECTRONIC GROUND STATE OF 2-CYCLOHEXEN-1-ONE AND ITS 2,6,6- <i>d</i> ₃ ISOTOPOMER 44
	Introduction 44
	Experimental..... 47
	Computations..... 48
	Molecular vibrations..... 48
	Results and discussion..... 49
	Conclusions 63
VI	ULTRAVIOLET CAVITY RINGDOWN SPECTRA OF 2- CYCLOHEXEN-1-ONE AND ITS POTENTIAL ENERGY FUNCTION FOR THE ELECTRONIC GROUND STATE 65
	Introduction 65
	Experimental and computational 65
	Results and discussion 66
	Cavity ringdown (CRD) spectra 66
	Raman spectra..... 72
	DFT calculations..... 74
	Kinetic energy functions..... 78
	Ring-inversion potential energy function 79
	Conclusions 79
VII	ULTRAVIOLET CAVITY RINGDOWN SPECTRA AND THE S ₁ (n,π*) RING-INVERSION POTENTIAL ENERGY FUNCTION FOR 2-CYCLOHEXEN-1-ONE- <i>d</i> ₀ AND ITS 2,6,6- <i>d</i> ₃ ISOTOPOMER..... 83

CHAPTER	Page
Introduction	83
Experimental and computational	84
Results and discussion	84
Vibronic analysis	84
Potential energy functions for ring inversion	91
Comparisons with DFT results	104
Conclusions	104
 VIII THE RING-PUCKERING POTENTIAL ENERGY FUNCTION OF 1,4-DIHYDRONAPHTHALENE IN ITS GROUND AND S ₁ (π, π^*) ELECTRONIC STATES	106
Introduction	106
Experimental.....	107
Experimental results	107
Computations.....	112
Conclusions	119
 IX VIBRATIONAL ASSIGNMENTS OF 1,4- DIHYDRONAPHTHALENE IN ITS GROUND AND S ₁ (π, π^*) STATES.....	120
Introduction	120
Experimental.....	120
Computations.....	121
Results and discussion	122
Infrared and Raman spectra.....	122
FES spectra	128
SVLF spectra	132
UV spectra and the energy level diagrams	143
Conclusions	146
 X STRUCTURE AND VIBRATIONAL FREQUENCIES OF 2- METHYL-2-CYCLOPENTEN-1-ONE IN ITS ELECTRONIC GROUND STATE.....	147
Introduction	147
Computations.....	147
Experimental.....	147
Results and discussion.....	148

CHAPTER	Page
Structure and conformations of 2MCP	148
Vibrational frequencies.....	150
Conclusions	155
XI CONCLUSIONS	156
REFERENCES	160
VITA.....	165

LIST OF TABLES

TABLE	Page
1	Rotational constants (in GHz) and structural parameters of $^{13}\text{DSCB-}h_4$ and $^{13}\text{DSCB-}d_4$ 24
2	Vibrational assignment (in cm^{-1}) of $^{13}\text{DSCB-}h_4$ (vapor and liquid)..... 30
3	Vibrational assignment (in cm^{-1}) of $^{13}\text{DSCB-}d_4$ (vapor and liquid)..... 32
4	Vibrational assignment (in cm^{-1}) of $^{13}\text{DSCB-}h_4$ (solid)..... 37
5	Vibrational assignment (in cm^{-1}) of $^{13}\text{DSCB-}d_4$ (solid) 39
6	Vibrational assignment (in cm^{-1}) of 2-cyclohexen-1-one..... 52
7	Vibrational assignment (in cm^{-1}) of 2-cyclohexen-1-one $-d_3$ 61
8	Selected assignments for the CRD spectrum (in cm^{-1}) of 2CHO 69
9	Relative out-of-plane displacements of C1, C4, C5, and C6 (in Angstroms) 76
10	Rotational constants (in GHz) of 2-cyclohexen-1-one 77
11	Observed and calculated frequencies (in cm^{-1}) for the vibration of 2-cyclohexen-1-one in its S_0 state..... 81
12	CRD transition frequencies (in cm^{-1}) and assignments for 2CHO 87
13	CRD transition frequencies (in cm^{-1}) and assignments for 2-CHO- d_3 89
14	Calculated relative out-of-plane displacements (\AA) of C1, C4, and C6 atoms of 2CHO in its S_0 and $S_1(n,\pi^*)$ states 97
15	Calculated kinetic energy coefficients of 2CHO and 2CHO- d_3 98
16	Observed and calculated frequencies (in cm^{-1}) for the ν_{39} vibration of 2CHO- d_0 and 2CHO- d_3 in their S_0 state..... 100

TABLE	Page
17 Observed and calculated frequencies (in cm^{-1}) for the ν_{39} vibration of 2CHO- d_0 and 2CHO- d_3 in their $S_1(\pi, \pi^*)$ states	102
18 Fluorescence excitation (FES) and ultraviolet (UV) absorption bands (in cm^{-1}) of 14DHN involving the ring puckering (ν_{54}) vibration	111
19 Observed and calculated ring-puckering transitions (in cm^{-1}) of 14DHN in its S_0 ground and $S_1(\pi, \pi^*)$ excited states.....	116
20 Vibrational assignment (in cm^{-1}) of 1,4-dihydronaphthalene.....	125
21 FES spectrum of 14DHN compared to some selected UV bands	130
22 SVLF bands (in cm^{-1}) observed from some excitations of 14DHN	140
23 Some selected UV bands (in cm^{-1}) of 14DHN	145
24 Experimental and calculated vibrational frequencies (in cm^{-1}) of 2MCP ..	153

LIST OF FIGURES

FIGURE		Page
1	The transitions of the various spectroscopic techniques used	7
2	Calculated structures of puckered (C_{2v}) and planar (D_{2h}) 13DSCB	21
3	Dihedral angle of puckered 13DSCB	22
4	Infrared spectrum of liquid 13DSCB compared to its calculated spectrum	25
5	Raman spectrum of liquid 13DSCB compared to its calculated spectrum.	26
6	Infrared spectrum of liquid 13DSCB- d_4 compared to its calculated spectrum.....	28
7	Raman spectrum of liquid 13DSCB- d_4 compared to its calculated spectrum.....	29
8	CH_2 twisting and wagging vibrations of 13DSCB and the partial charges calculated for each atom	35
9	Raman spectra of 13DSCB- h_4 and - d_4 for its vapor, liquid, and solid (77 K) in the 200-600 cm^{-1} region	41
10	Correlation diagram for ν_6 (ring-angle bending), ν_{12} (SiH_2 out-of-phase rocking), and ν_{21} (SiH_2 in-phase rocking) for DSCB- h_4 and - d_4 for their C_{2v} (puckered vapor) and D_{2h} (planar solid) structures	42
11	Liquid and vapor-phase infrared spectra of 2CHO compared to its calculated DFT spectrum.....	50
12	Liquid and vapor-phase Raman spectra of 2CHO compared to its calculated DFT spectrum.....	51
13	Liquid-phase infrared and Raman (with parallel and perpendicular polarization) spectra of 2CHO.....	55
14	Fermi interaction of C=O stretching mode of 2CHO	56
15	Intermolecular interactions of 2CHO molecules in the liquid-phase due to the polar carbonyl group.....	58

FIGURE	Page
16	Calculated and liquid infrared spectra of 2CHO- d_3 59
17	Calculated and liquid Raman spectra of 2CHO- d_3 60
18	Liquid Raman spectra of 2CHO- d_3 with parallel and perpendicular polarization compared with liquid IR spectra..... 64
19	Cavity ringdown spectra of 2CHO relative to the S_1 0_0^0 band at 26089.1 cm^{-1} in the -400 to 400 cm^{-1} region 67
20	Cavity ringdown spectra of 2CHO relative to the $S_1(n,\pi^*)$ 0_0^0 band at 26089.1 cm^{-1} in the difference band region..... 68
21	Vibrational energy levels for the ground state of 2CHO for ν_{39} , ν_{38} , and ν_{37} 71
22	Raman spectra of 2CHO vapor in the low-frequency region 73
23	Calculated minimum energy and planar structures of 2CHO using B3LYP/6-31+G(d,p) and B3LYP/6-311+G(d,p) level of theories..... 75
24	Ring-inversion potential energy function for 2CHO corresponding to equation 6.2 80
25	CRD spectrum of 2CHO vapor at room temperature..... 85
26	Comparison of CRD spectra for CHO- d_0 and CHO- d_3 86
27	Energy map for 2CHO in its S_0 and $S_1(n,\pi^*)$ electronic states..... 92
28	Energy map for 2CHO- d_3 in its S_0 and $S_1(n,\pi^*)$ electronic states..... 93
29	Calculated structures for 2CHO in its S_0 and $S_1(n,\pi^*)$ electronic states 94
30	Qualitative picture of the π^* orbital involved in the $n \rightarrow \pi^*$ transition of 2CHO and 2CPO 96
31	Ring-inversion potential energy function for 2CHO and 2CHO- d_3 in their S_0 state..... 101

FIGURE	Page
32 Ring-inversion potential energy function for 2CHO and 2CHO- d_3 in their $S_1(n,\pi^*)$ state	103
33 Comparison of the S_0 and $S_1(n,\pi^*)$ ring-inversion potential energy functions	105
34 Fluorescence excitation (bottom) and ultraviolet absorption spectra (top) of 14DHN	108
35 SVLF spectra of 14DHN from 0_0^0 and 54_0^2 excitation bands compared to the UV spectra in the same region.....	109
36 Definition of the ring-puckering coordinate x and the ring-puckering angle τ	113
37 Calculated structures of 14DHN in its ground (S_0) and $S_1(\pi,\pi^*)$ electronic states.....	114
38 Ring-puckering potential functions for 14DHN in its ground (left) and $S_1(\pi,\pi^*)$ excited (right) states	117
39 Comparison of the 14DHN S_0 and S_1 potential energy functions with the 1,4-cyclohexadiene (14CHD) function.....	118
40 Liquid-phase infrared spectra of 14DHN compared to its calculated DFT spectrum.....	123
41 Liquid and vapor-phase Raman spectra of 14DHN compared to its calculated DFT spectrum.....	124
42 FES spectrum of 14DHN with some assignments.....	129
43 Labeling scheme for SVLF spectra acquired by different excitations	133
44 SVLF spectra of 14DHN from 0_0^0 excitation with some assignments	135
45 SVLF spectra of 14DHN from 54_0^2 excitation with some assignments	136
46 SVLF spectra of 14DHN from 28_0^2 excitation with some assignments.....	138

FIGURE	Page
47 SVLF spectra of 14DHN from 53_0^2 excitation with some assignments	139
48 Energy level diagram of 14DHN which depicts the vibrational levels involving some of the low-frequency modes	144
49 The three calculated conformers of 2MCP which show the orientation of the hydrogen atoms of its methyl group	149
50 Liquid-phase infrared spectrum of 2MCP compared to its calculated DFT spectrum	151
51 Liquid-phase Raman spectrum of 2MCP compared to its calculated DFT spectrum	152

CHAPTER I

INTRODUCTION

Determination of potential energy surfaces is one of the most popular research areas in physical chemistry. The importance of these potential energy surfaces can be easily understood as they can provide an enormous amount of information on molecular structure and conformations, inter and intra molecular forces, energy barriers, reaction pathways, and various other aspects of chemistry.¹ Conformational changes of molecules are typically associated with anharmonic, low-frequency, large-amplitude vibrations which interact little with higher frequency vibrational modes. These vibrations include out-of-plane ring vibrations, internal rotations, and skeletal twistings. As a result, many of the conformational changes of molecules may be described by potential energy functions which are governed by only one or two vibrational coordinates. Various spectroscopic techniques have been used to determine the transitions between quantum states of these vibrational modes. Far-infrared and low-frequency Raman spectra for molecules in the ground electronic states, and ultraviolet and laser induced fluorescence spectra for molecules in the excited electronic states are among these techniques. Cavity ringdown spectroscopy, a relatively new but a very powerful technique also has now been used to study the excited states of molecules, particularly for states with very weak electronic transitions, e.g. triplet excited states. In addition to this, with the development of computational resources during last three decades, theoretical methods for high level of classical and quantum mechanical calculations have become an integral part of this type of research. These can provide valuable information on molecular structures and conformations, vibrational frequencies, and Raman intensities which can complement the experimental data.

This dissertation follows the style of *Journal of Physical Chemistry, A*.

Since three points define a plane, an N-membered cyclic molecule has N-3 out-of-plane vibrational modes. Therefore, a four-membered cyclic molecule such as cyclobutane has only one out-of-plane ring motion and this is called the ring-puckering. This mode has the lowest vibrational frequency for this molecule. For five-membered rings such as cyclopentane or furan, there are two out-of-plane motions which have low vibrational frequencies. Therefore, as the number of atoms in a molecule increases, the number of out-of-plane modes also increases. In some cases it may be necessary to consider all of these modes simultaneously for a full conformational analysis. However, Laane and Lord showed that some unsaturated molecules such as cyclopentene² and 1,4-cyclohexadiene³ can be regarded as pseudo-four-membered rings, and they have a ring-puckering vibration similar to that of cyclobutane. The π -bonding in the ring restricts the motion of atoms and one C=C unit can be considered as one atom. Therefore, the ring-puckering motions of these pseudo-four-membered rings can be treated independently from other out-of-plane modes and expressed in terms of one-dimensional potential energy functions. Similarly, the molecule cyclohexene can be treated as a pseudo-five-membered ring with two interacting out-of-plane modes, the ring bending (or puckering) and ring-twisting. In such cases the potential energy function for the out-of-plane motion should be expressed with respect to the coordinates of the above two vibrations.

R. P. Bell in 1945 postulated that the ring puckering vibration of cyclobutane can be represented by a quartic potential energy function.⁴ However, investigation of some molecules using far-infrared spectroscopy showed that the low-frequency ring-puckering vibrations of these can be best expressed by a mixed quartic-quadratic potential energy function.⁵⁻⁷ In fact, the ring-puckering of cyclobutane was later found to have a function with a double minimum.⁸ Therefore, since Bell's postulation, a large number of cyclic and bicyclic molecules have been investigated both spectroscopically and theoretically with the methodologies presented in detail in many publications and reviews.⁹⁻¹⁴ In the present work, the conformations of several cyclic and bicyclic molecules have been

investigated by spectroscopic and theoretical methods and the results of these studies will be presented herein.

1,3-DISILACYCLOBUTANE

1,3-Disilacyclobutane (13DSCB) is a four-membered cyclic molecule which can either have a puckered (with C_{2v} symmetry) or a planar (with D_{2h} symmetry) structure. This compound and its 1,1,3,3- d_4 isotopomer were first prepared by Irwin, Cooke, and Laane in 1977 using high temperature pyrolysis.¹⁵ The potential energy function of this molecule for the ring-puckering vibration determined by vapor-phase far-infrared spectroscopy proved that the equilibrium conformation of this molecule is puckered with a barrier to planarity of 87 cm^{-1} (0.25 kcal/mol) and a puckering angle of 24° . Microwave studies also confirmed this non-planar structure and showed that it has unexpectedly large CSiC angles.^{16,17} However, the force constant calculations for both planar and puckered structures and the observation of vibrational coupling in the infrared and Raman spectra of vapor, liquid, and solid phases have shown that this molecule becomes planar in the solid state.¹⁸

In order to confirm the previous assessment of these conclusions, and to reexamine the vibrational assignments made by infrared and Raman spectroscopy, 13DSCB and its d_4 isotopomer were analyzed with several *ab initio* and DFT calculations and the results of these will be presented.

2-CYCLOHEXEN-1-ONE

2-Cyclohexen-1-one (2CHO) is an α,β -unsaturated ketone whose structure is similar to the previously studied 2-cyclopenten-1-one (2CPO). The ring-bending potential energy function of 2CPO showed that although the molecule is planar in both the ground¹⁹ and singlet²⁰ electronic states it becomes slightly puckered in the triplet²¹ electronic state. This interesting feature of 2CPO inspired the spectroscopic analysis of 2CHO.

2CHO is a non-planar asymmetric six-membered ring molecule. It is expected that the conjugation between C=C and C=O groups provides an extra rigidity to the ring which keeps all the atoms of the ring in a plane except for the carbon at the 5th position. This was experimentally verified by Manley and Tyler in 1970 who proposed a structure for 2CHO using the rotational constants determined by microwave spectroscopy.²² Therefore, the ring-inversion vibration of 2CHO which involves the out-of-plane motion of the C-5 atom can be treated as a one-dimensional motion. Although low-frequency Raman²³ and far-infrared²⁴ spectroscopic techniques have been previously utilized to determine the potential energy function of the ring-inversion, the results given by these two analyses were completely different from each other. Therefore, further spectroscopic studies were undertaken on 2CHO and its 2,6,6-*d*₃ isotopomer (2CHO-*d*₃) in order to understand the inversion process better. The research work done here will present the one-dimensional ring-inversion potential energy functions of 2CHO and 2CHO-*d*₃ in their ground and singlet S₁(n,π^{*}) electronic states determined by cavity ringdown spectroscopy, an ultra-high sensitive spectroscopic method. Furthermore, a complete vibrational assignment of these two molecules in their ground electronic state will be presented based on liquid- and vapor-phase infrared and Raman spectra together with density functional theory calculations.

1,4-DIHYDRONAPHTHALENE

1,4-Dihydronaphthalene (14DHN) is a bicyclic molecule whose structure is comparable to those of 1,4-cyclohexadiene (14CHD) and 9,10-dihydroanthracene (DHA). The stereochemistry of the dihydro ring of these molecules, that is, whether the ring is planar or puckered, has been a question for a long time. The similarity of these compounds to the biologically important quinones further underscores the need to understand the structures of these parent compounds fully. In 1971, Laane and Lord, using far-infrared spectroscopy showed that the 14CHD molecule is planar³ although a previous electron diffraction study had postulated a puckered molecule.²⁵ In 1988 Strube and Laane²⁶ determined a quantitative vibrational potential energy function for the ring-

puckering mode and again confirmed that the molecule was planar. The structure of DHA was also studied by various theoretical and spectroscopic methods²⁷⁻²⁹ and these studies proved that this molecule is puckered. Lipkowitz *et al.* in 1982 explained the increasing tendency of the dihydro ring to become bent or puckered when going from 14CHD to DHA in terms of angle strain and torsional effects.³⁰ Therefore an intermediate structure was expected for 14DHN. Molecular mechanics and *ab initio* calculations done on 14DHN predicted a planar structure but with a highly flexible dihydro ring.^{31,32} The present research work was carried out to determine the potential energy functions of 14DHN in its ground and $S_1(\pi, \pi^*)$ electronic states using laser induced fluorescence (LIF) and high resolution ultraviolet spectra. Although the LIF spectra of 14DHN have been studied by Chakraborty *et al.* previously,³³ as will be shown, their data didn't have the required spectroscopic accuracy to calculate an accurate ring-puckering potential energy function. A complete vibrational analysis of 14DHN also will be presented based on infrared and Raman measurements and aided by theoretical calculations.

2-METHYL-2-CYCLOPENTEN-1-ONE

2-Methyl-2-cyclopenten-1-one (2MCP) is another α, β -unsaturated ketone which has a methyl group attached to it at the 2nd carbon of the ring. Preliminary studies on this molecule were done using liquid-phase infrared and Raman spectroscopy in order to do a complete vibrational assignment. This type of study will be useful for a future investigation of the internal rotation of methyl groups that was previously done for the isomeric 3-methyl-2-cyclopenten-1-one.³⁴ High level *ab initio* and density functional theory calculations were also carried out to complement the spectral data. The results of these experimental and theoretical investigations will be presented.

CHAPTER II

EXPERIMENTAL METHODS

The following sections will present a concise description of the various spectroscopic techniques used in the present study. Additional specific details used for each molecule will be presented in the relevant sections. The different types of spectroscopic transitions utilized for this work are illustrated in Figure 1.

INFRARED AND RAMAN SPECTROSCOPY

Infrared and Raman spectroscopy are of vital importance since both of them can determine the vibrational energy levels of the electronic ground state of molecules. The principal difference between these two methods comes from the way the molecules interact with the incident radiation or the electromagnetic energy entering the system. In order to observe a transition in the infrared spectroscopy, a molecule must have a vibrational mode which changes its dipole moment during the atomic motions of the molecule. This dipole moment change results from an interaction between the molecule and the incident infrared radiation and results in an absorption band in the infrared spectrum. Conversely, a Raman transition comes about from a vibrational mode which changes the polarizability of the molecule. This polarizability change or oscillation results in the scattering of the incident radiation at a changed frequency. The Raman transition is illustrated in Figure 1. The molecule is typically excited to a level somewhere between the ground and excited electronic states in energy by the incident radiation. This is called the virtual excited state. The scattering takes place when the molecule returns to the initial level or to a higher vibrational level in the electronic ground state. The scattered light consists mostly of the unchanged wavelength or frequency of the incident light and is called the Rayleigh scattering. However, a small amount of scattered radiation lies at increased or decreased frequency. The radiation with decreased frequency is called the Stokes Raman scattering (or simply, Raman

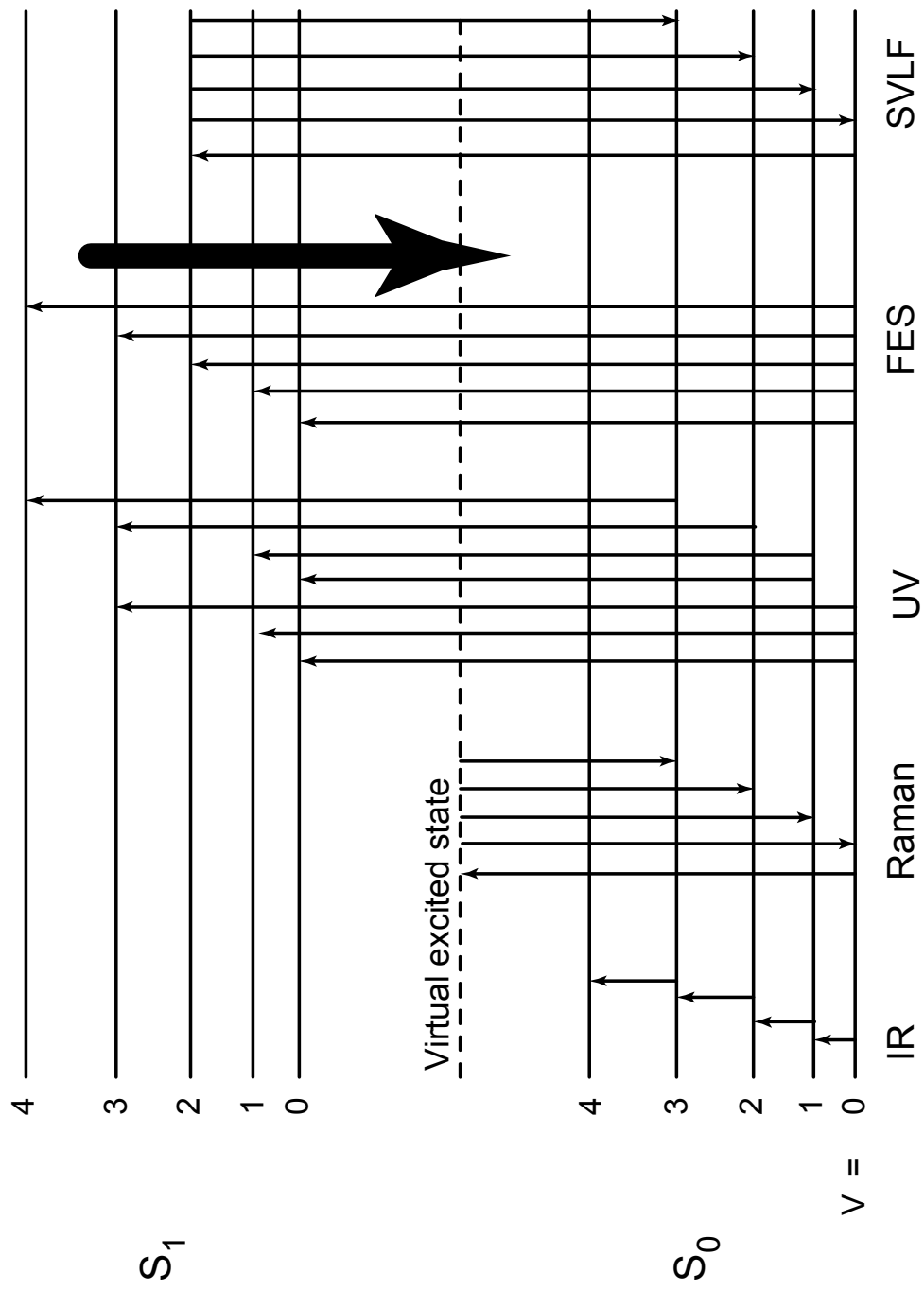


Figure 1. The transitions of the various spectroscopic techniques used.

scattering) and that with the increased frequency is called anti-Stokes Raman scattering (not shown in Figure 1). In the present study only the Stokes Raman was utilized. For a given molecule some of its vibrational modes or transitions may be Raman active, some may be infrared active, some may be both infrared and Raman active, and some may be neither depending whether these modes result in dipole moment changes or/and polarizability changes in the molecule. Selection rules which are based on the molecular symmetry help to determine whether a transition is infrared or Raman active.

The Raman spectra of the compounds presented in this work were acquired on an SA Jobin-Yvon U-1000 spectrometer equipped with liquid-nitrogen cooled CCD (charge-coupled device) and PMT (photo multiplier tube) detectors. Raman scattering was achieved using either a Coherent Radiation Innova 20 argon ion laser with an excitation at 514.5 nm or a Coherent Verdi-V10 diode-pumped laser with an excitation line at 532 nm. The liquid-phase spectra were recorded at room temperature with a lasing power of 0.5-1 W. A polarizer and a scrambler were used to measure the parallel and perpendicular polarized Raman scattering. Vapor-phase Raman spectra of the compounds which were contained in a special high-temperature Raman cell³⁵ collected at temperatures ranging from of 230-300⁰ C. A laser power of 5 W was used for this purpose.

The liquid mid-infrared spectra were collected on a Bruker Vertex 70 FT (fourier transform)-spectrometer equipped with a global light source, a KBr beamsplitter and a DLaTGS (deuterated lanthanum triglycine sulfate) detector. The liquid far-infrared spectrum was also collected on the same instrument equipped with a mylar beamsplitter, and an MCT (mercury cadmium telluride) detector which has a detection range of 630-60 cm⁻¹. The vapor phase mid-infrared spectra were recorded on a Bomem DA8.02 FT-IR spectrometer equipped with a global light source, a KBr beamsplitter, and a DTGS (deuterated triglycine sulfate) detector. A non-heatable 4-m multi path IR cell with KBr windows was used here.

JET COOLED LASER-INDUCED FLUORESCENCE (LIF) SPECTROSCOPY

LIF consists of two separate techniques, fluorescence excitation spectroscopy (FES) and single-vibronic level fluorescence (SVLF) spectroscopy. As shown in Figure 1 these two techniques give information on vibrational energy levels in the ground and excited (singlet or S_1) electronic states respectively.

For FES spectra the heated vapor of the sample was mixed with a stream of noble gas known as carrier gas which is at high pressure, and was injected into an evacuated chamber through a nozzle to create a molecular beam. The pressure of the chamber is kept in the range of 10^{-5} to 10^{-6} torr in order to sufficiently cool the sample which minimizes the number of molecules in the vibrationally excited states. Therefore, almost all of the electronic transitions take place from the lowest vibrational energy level as shown in Figure 1. The transitions to the electronic excited states can be accomplished by tuning an ultraviolet laser which intersects the molecular beam. The molecular beam excited by the tuning laser can release the energy gained in a variety of ways and one such way is emitting it as fluorescent light. Therefore a spectrum can be obtained by plotting the intensity of the emitted light as a function of the laser frequency. This spectrum shows the energy required to reach the vibronic levels of the excited electronic state. The excitation for FES was achieved using a tunable ultraviolet laser system which consists of a Continuum Powerlite 9020 Nd:YAG laser which pumps a Continuum Sunlite optical parametric oscillator (OPO). The frequency of the visible radiation from the OPO was doubled by a Continuum FX-1 doubling package. The output radiation from this package is capable of being tuned from 220 to 355 nm continuously with a resolution of 0.7 cm^{-1} . The fluorescent light was detected directly by a photo multiplier tube (PMT) manufactured by Hamamatsu. Argon was used as the backing gas whose stated purity was 99.99%. The pressure of the backing gas was typically in the range of 1 to 20 atmospheres and the specific value was selected to obtain the optimal spectra. The spectral resolution of FES was 1 cm^{-1} .

The SVLF spectra, also known as dispersed fluorescence, were acquired by tuning the laser in order to excite the molecule to a specific vibronic level, which was

already determined by FES. The fluorescent light emitted from this excited level was dispersed into individual frequencies by passing it through a Jobin Yvon ISA HR640 monochromator. The vibrational energy levels of the ground state were determined by these individual frequencies. The dispersed light was detected by a Spectrum One charge-coupled device (CCD) detector with a 2000×800 pixel chip. The resolution of this detector was $\pm 2 \text{ cm}^{-1}$.

ELECTRONIC ABSORPTION SPECTROSCOPY

Electronic absorption spectroscopy or ultraviolet (UV) spectroscopy is another technique which can determine the vibronic energy levels of the excited electronic states. The difference between UV and FES is the temperature of the sample at which the spectrum is acquired. The jet-cooled spectra obtained from FES have all its transitions originated from only very low energy vibrational levels. Therefore, the spectrum is greatly simplified. However, a UV spectrum is obtained either at room temperature or at elevated temperatures. Therefore, it can have bands originating from the higher vibrational energy levels, which were not observed in the FES spectra. These bands are called hot bands. Therefore, use of both FES and UV spectra together greatly helps in assigning the excited state vibrational levels correctly. The vapor-phase UV spectra presented here were acquired on a Bomem DA8.02 FT-spectrometer equipped with a deuterium light source, a quartz beamsplitter, and a silicon detector with a detection range of 20,000-50,000 cm^{-1} . The sample was contained in a 15 cm vapor glass cell with quartz windows. The spectra were acquired either at room temperature or at higher temperature depending on the physical state and the vapor pressure of the sample.

CAVITY RINGDOWN SPECTROSCOPY

Cavity ring down spectroscopy (CRDS) is a technique which was first designed by O'Keefe and Deacon in 1988.³⁶ It can achieve very long path lengths (several km) with a bench top experimental set up thus making it a simple and inexpensive but a very powerful tool for vapor-phase spectroscopic studies which require ultra-high sensitivity.

Therefore, this technique is used for investigation of species with very weak electronic transitions such as singlet to triplet excitation and also in atmospheric trace gas analysis. It also can be used for molecules whose excited electronic states cannot be investigated by conventional spectroscopic methods such as LIF. The principles and the experimental details of the CRDS are now available in many texts and publications.³⁷⁻³⁹ All of the CRDS work presented here were carried out at the Laboratory of Dr. Stephen Drucker of University of Wisconsin at Eau Claire. The details of the experimental work done will be presented in the relevant sections.

CHAPTER III

THEORETICAL METHODS

INTRODUCTION

Theoretical calculations constituted an integral part of this research which investigated the conformations, potential energy functions, and vibrational modes of molecules. Two types of theoretical methods were utilized in the research work presented here. The first was the use of various computational methods which are based on the principles of quantum mechanics to calculate the molecular structures, vibrational frequencies, Raman intensities and other important data such as dipole moments, charge distribution etc. These are called ab initio calculations or density functional theory calculations. The second is the determination of mathematical functions used to model the vibrational motion of molecules. These functions include kinetic energy functions which calculate the reduced mass of the vibrational motions and also potential energy functions which show the energy dependence on the displacement of the atoms of the molecules. These two types of theoretical calculations are briefly described in this chapter.

COMPUTATIONAL CHEMISTRY

Computational chemistry enables chemists to study the structures and other chemical and physical properties of molecular systems by running calculations on computers rather than examining them by experimental means.

There are two broad areas within computational chemistry: Molecular mechanics, and electronic structure theory. Molecular mechanics (MM) is based on a model of a molecule as a collection of balls (atoms) held together by springs (bonds). It uses the laws of classical mechanics to predict the properties of molecules. In the present work, MM methods were deemed to not have sufficient accuracy for the molecules of interest and were not utilized. Electronic structure methods on the other hand, use the

principles of quantum mechanics, fully or partially, as the basis of their calculations. The molecular properties are obtained by solving the Schrödinger Equation

$$H\Psi = E\Psi \quad (3.1)$$

where H is the Hamiltonian energy operator and the many values of E represent the quantized energy states. The Ψ 's are the wavefunctions.

The solutions for Eq. (3.1) are the energies and the wavefunctions of the molecular system. However this cannot be solved exactly for any but the smallest one, i.e. for hydrogen atom-like systems where there is no electron-electron repulsion. Therefore there are various electronic structure methods characterized by the mathematical approximation methods used to solve the Schrödinger Equation. These are mainly of two classes: The first one are the semi-empirical methods that solve the Schrödinger equation approximately with the use of suitable experimental parameters available for the type of molecular system of interest. The second is the *ab initio* methods, which use no experimental parameters at all, and whose foundation is solely dependent upon the principles of quantum mechanics and the values of some physical constants such as Planck's constant, the velocity of light, and the permittivity of the vacuum. The major difference between these two classes is the trade-off made between the computational cost and the accuracy of the results. Semi-empirical methods are inexpensive compared to *ab initio* methods. They predict fairly accurate quantities for energies and structural data for systems for which good parameter sets exist. *Ab initio* methods in contrast can predict quantities of high accuracy and reliability. In principle, they can be applied for systems of any size or class though the computational cost increases as the size of the system increases. However, with the development of computers, *ab initio* methods can now be used to investigate fairly large molecular systems with even several hundred atoms. Since these calculations use only the principles of quantum mechanics, *ab initio* methods are applicable to excited states, unstable and hypothetical molecules, reaction intermediates etc.

In recent times, a third class of electronic structure methods have begun to play a significant role in the field of computational chemistry. This is known as density functional theory (DFT) methods. These are also based on the Schrödinger Equation but the solutions do not yield wavefunctions. Rather, DFT methods calculate an electron distribution (or a density) functional. Computational cost of DFT methods are somewhere in between those of semi empirical and *ab initio* methods. Therefore, DFT methods are becoming increasingly popular.

This research work mainly used the *ab initio* methods of Hartree-Fock (HF) Theory, Second-order Möller-Plesset Perturbation Theory (MP2), Configuration interaction-singles (CIS), and Coupled-Cluster Theory (CCSD). The DFT calculations were done mostly with B3LYP (three-term Becke functional combined with Lee, Yang, Parr exchange functional). These theories are coupled with appropriate basis sets (a set of linear combinations of mathematical functions that describes the shapes of molecular orbitals) in order to calculate the required molecular parameters. The principles of *ab initio* and DFT calculations is available in many texts.⁴⁰⁻⁴⁴ All of the *ab initio* and DFT calculations presented here were carried out using the Gaussian 03 quantum mechanical package.⁴⁵

KINETIC AND POTENTIAL ENERGY OPERATORS

The conformational changes of non-rigid molecules can be well represented by potential energy surfaces which are defined by one or two vibrational coordinates. These functions can be determined from experimental spectroscopic data in conjunction with quantum mechanics. The time-independent Schrödinger equation for molecular vibrations is

$$\hat{H}^{vib}\Psi^{vib} = E^{vib}\Psi^{vib} \quad (3.2)$$

where \hat{H}^{vib} is the vibrational Hamiltonian operator. Ψ^{vib} is the vibrational wavefunction, and E^{vib} represents the solutions for the vibrational energy or each vibrational wavefunction. The vibrational Hamiltonian can be expressed as

$$\hat{H}^{vib} = \hat{T} + \hat{V} \quad (3.3)$$

where \hat{T} and \hat{V} represent the kinetic and potential energy operators respectively.

The kinetic energy operator

For a molecule having N atoms, the vibrational kinetic energy operator \hat{T} can be expressed as

$$\hat{T} = \frac{1}{2}(\omega^t \dot{q}^t) G \begin{pmatrix} \omega \\ \dot{q} \end{pmatrix} \quad (3.4)$$

where ω is a three-dimensional angular momentum column vector, q is the 3N-6 dimensional vector of linear momenta conjugate to the vibrational coordinate q , G is the Wilson G matrix.^x The superscript t denotes the matrix transpose.

The G matrix depends on the molecular rotations and vibrations and can be expressed as

$$G = \begin{pmatrix} \mathbf{I} & \mathbf{X} \\ \mathbf{X}^t & \mathbf{Y} \end{pmatrix}^{-1} \quad (3.5)$$

\mathbf{I} is a 3 × 3 inertial moment tensor, whose elements can be defined as

$$\mathbf{I} = \begin{pmatrix} I_{xx} & -I_{xy} & -I_{xz} \\ -I_{yx} & I_{yy} & -I_{yz} \\ -I_{zx} & -I_{zy} & I_{zz} \end{pmatrix} \quad (3.6)$$

where each element of \mathbf{I} can be expressed in terms of atomic masses and coordinate vectors. The matrix \mathbf{X} in Eq. (3.6) is the 3 × (3N-6) rotational-vibrational interaction matrix defined by

$$X_{ij} = \sum_{l=1}^N m_l \left(r_l \times \left(\frac{\partial r_l}{\partial q_j} \right) \right)_i \quad (3.7)$$

and Y represents the matrix which describes the pure vibrational interactions which is expressed as

$$Y_{ij} = \sum_{l=1}^N m_l \left(\frac{\partial r_l}{\partial q_i} \right) \cdot \left(\frac{\partial r_l}{\partial q_j} \right) \quad (3.8)$$

m_l represents the mass of the l^{th} atom, r_l is the coordinate vector from the l^{th} atom to the center of mass, and q is the vibrational coordinate. For a molecule with large number of atoms, a multi-dimensional analysis is required which is very difficult in practice. However for molecules such as pseudo four-membered-rings such as cyclopentene or 1,4-cyclohexadiene, their ring-puckering vibration can be separable from other normal modes. In such a case, the vibrational mode of interest can be analyzed independently and the Wilson G matrix becomes

$$G = \begin{pmatrix} I_{xx} & -I_{xy} & -I_{xz} & X_{11} \\ -I_{yx} & I_{yy} & -I_{yz} & X_{12} \\ -I_{zx} & -I_{zy} & I_{zz} & X_{13} \\ X_{11} & X_{12} & X_{13} & Y_{13} \end{pmatrix}^{-1} \quad (3.9)$$

The inverted G matrix is defined as

$$G = \begin{pmatrix} g_{11} & g_{12} & g_{13} & g_{14} \\ g_{21} & g_{22} & g_{23} & g_{24} \\ g_{31} & g_{32} & g_{33} & g_{34} \\ g_{41} & g_{42} & g_{43} & g_{44} \end{pmatrix} \quad (3.10)$$

Where g_{ij} 's are the reciprocal reduced masses. The g_{ij} 's in the equation with i and $j = 1, 2,$ and $3,$ represent the pure rotational motion by convention. The g_{i4} and g_{4j} terms with i and $j = 1, 2,$ and $3,$ represent the rotational-vibrational interactions. The pure vibrational term is g_{44} and this represents the reduced mass for the vibrational motion.

The reduced mass for a large-amplitude vibration varies with the vibrational coordinate. Therefore, for a such a motion the reduced mass is expressed as a function in terms of the vibrational coordinate:

$$g_{44}(x) = \sum_{i=0}^n g_{44}^i x^i = \frac{1}{\mu(x)} \quad (3.11)$$

Where g_{44}^i are the expansion coefficients and $\mu(x)$ is the coordinate-dependent reduced mass. The terms in the Eq. (3.11) are generally ignored after the sixth power term. The odd-powered terms are zero for symmetric vibrations.

The kinetic energy functions used in this research work were written by vector methods which express the position of each atom as a function of the vibrational coordinate in a center-of-mass system. The kinetic energy expression terms for different molecular types were reported previously reported by Laane's research group.⁴⁶⁻⁴⁸

The potential energy operator

The low-frequency vibrational modes of ring molecules such as ring-puckering and ring-bending vibrations with large-amplitudes are highly anharmonic. Therefore their vibrational motion cannot be described by a harmonic function. R. P. Bell in 1945 predicted that the ring-puckering vibration of a four-membered ring could be represented by a quartic potential energy function.⁴ However, later studies done on several four-member ring molecules⁵⁻⁷ showed that their ring-puckering can be best described by a mixed quadratic-quartic potential energy function which can be expressed as

$$\hat{V} = ax^4 + bx^2 \quad (3.12)$$

Where a and b are force constants related to the ring-angle strain and torsional strain of the molecule. x is the vibrational coordinate. The sign of b determines the shape of the potential energy curve. If b is negative the function has two minima and it indicates a bent equilibrium of the molecule. The planar structure is the maximum of such a curve and the barrier to planarity value, B , is given by the formula

$$B = \frac{b^2}{4a} \quad (3.13)$$

The coordinate corresponding to the minimum energy structure is given by

$$x_{\min} = \pm \sqrt{\frac{b}{2a}} \quad (3.14)$$

If b is positive, the potential energy function has only one minima which correspond to the planar energy minimum structure. In the calculation of the potential energy function for a particular vibrational mode, the coefficients a and b are varied until the calculated energy levels, or vibrational eigen values, which best fit the experimental spectroscopic data are found.

CHAPTER IV

VIBRATIONAL SPECTRA AND THEORETICAL CALCULATIONS OF 1,3-DISILACYCLOBUTANE

INTRODUCTION

The molecules 1,3-disilacyclobutane (13DSCB) and its 1,1,3,3-*d*₄ isotopomer were first synthesized by Irwin and Laane in 1977.¹⁵ Far-infrared studies of this molecule proved that the four-membered ring is puckered with a barrier to planarity of 87 cm⁻¹ (0.25 kcal/mol) and has a puckering angle of 24° in the vapor phase. Microwave analysis also confirmed the puckered structure of the vapor phase and showed unexpectedly large values for CSiC angles.^{16,17} However, the force constant calculations for both planar (with D_{2h} symmetry) and puckered (with C_{2v} symmetry) structures and the observations of vibrational coupling in the infrared and Raman spectra of vapor, liquid, and solid phases have shown that this molecule becomes planar in the solid state.¹⁸

In order to confirm the previous assessment of these conclusions, 13DSCB and its *d*₄ isotopomer were analyzed with various *ab initio* and DFT calculation methods. The outcome of these studies not only explained the structure of 13DSCB better but also illustrated that this molecule has CH₂ wagging and twisting modes which have unusually low frequencies. This also led to the reexamination and reassignment of some of the vibrational modes reported previously.

EXPERIMENTAL

The experimental data for the synthesis of 13DSCB and its *d*₄ isotopomer, and the acquisition of infrared and Raman spectra have been previously published^{15,18} and also presented in a Ph.D. thesis.⁴⁹ No other laboratory has ever prepared this molecule and hence the only experimental spectroscopic data for 13DSCB and its *d*₄ isotopomer come from this previous study, and these are compared with the calculated results of the

present research work. This is not surprising as the preparation of the molecule is very difficult, involving high-temperature pyrolysis.

COMPUTATIONS

All of the calculations discussed here were done using the Gaussian 03 quantum mechanical package.⁴⁵ The structures of 13DSCB for its puckered form (with C_{2v} symmetry) and its restricted planar form (with D_{2h} symmetry) were calculated using the second-order Möller-Plesset Perturbation Theory with the triple zeta basis set (MP2/CC-PVTZ) and also using coupled cluster theory (CCSD) with the 6-311++G(d,p) basis set. The rotational constants were calculated using MP2/CC-PVTZ and B3LYP/6-311++G(d,p) levels of theories. The vibrational frequencies of 13DSCB and its isotopomer were calculated using several levels of theories such as B3LYP, BP86, TPSSPSS, HF, MP2 and CCSD with different basis sets (6-311++G(d,p), LanL2DZ, CC-PVDZ, CC-PVTZ, 6-311+G(3df, 3dp) etc.). All of these calculations give unusually low-frequency values for the CH_2 wagging and twisting vibrational modes. The calculated frequency values and the computed spectra presented here are from the B3LYP/6-311++G(d,p) basis set as this level of calculations give the values which are the closest to the experimentally observed frequencies. For scaling, a factor of 0.964 for frequencies over 1800 cm^{-1} and a factor of 0.985 for those below 1800 cm^{-1} were used, as from previous work⁵⁰⁻⁵³ it has been found that these factors for this basis set to fit experimental data extremely well (typically within 5 cm^{-1}).

STRUCTURE OF 13DSCB

The calculated structures of 13DSCB for its C_{2v} (puckered) and D_{2h} (planar) conformations are shown in Figure 2. The puckered structure is the most stable form for non-interacting molecules and this is calculated to be 160 cm^{-1} lower in energy than the planar molecule. The experimental value is 87 cm^{-1} . The computed dihedral angle of 23.6° , as shown in Figure 3, agrees very well with the experimental value¹⁵ of 24° ,

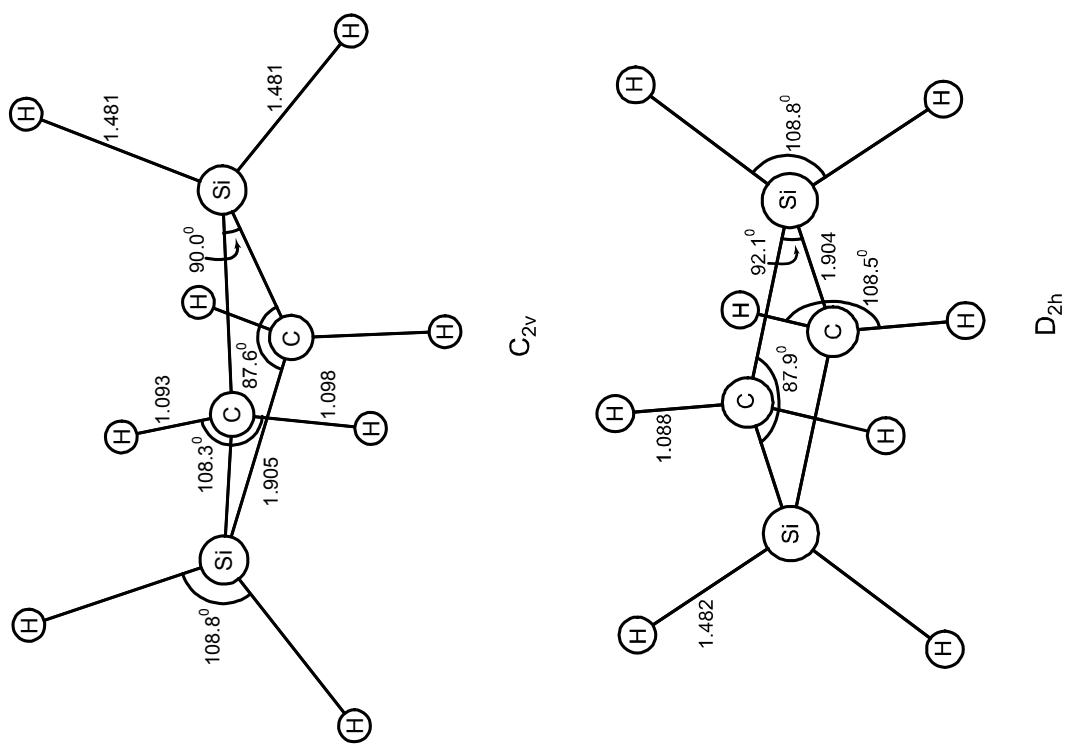


Figure 2. Calculated structures of puckered (C_{2v}) and planar (D_{2h}) 13DSCB.

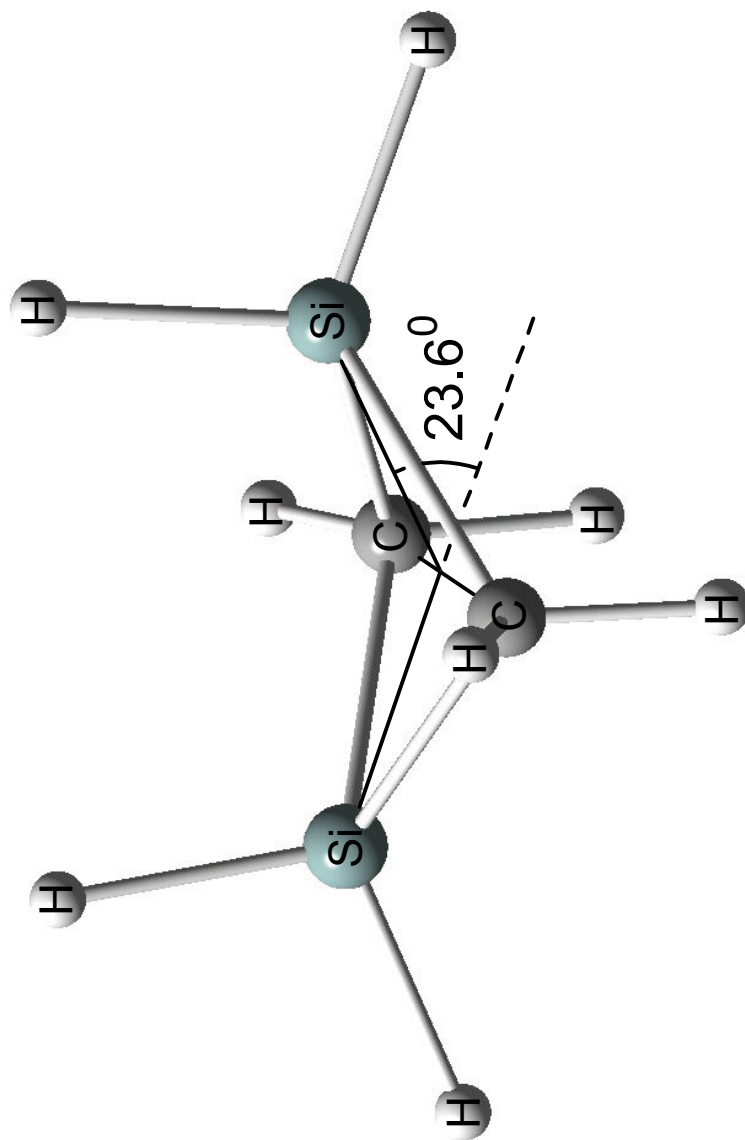


Figure 3. Dihedral angle of pucker 13DSCB.

especially in light of the fact that this is a non-rigid molecule with a large amplitude ring-puckering vibration.

Table 1 lists the calculated rotational constants for 13DSCB and its d_4 isotopomer, and those for the latter are compared to the experimental microwave values.^{16,17} No microwave work has been done for the h_4 isotopomer. The A, B, and C rotational constants for the C_{2v} structure of the d_4 molecule were calculated to be 0.2223, 0.1123, and 0.08755 cm^{-1} , respectively, in excellent agreement with 0.2226, 0.1132, and 0.08748 cm^{-1} from the microwave. While the calculated A and C constants differ by only about 0.1% from the experimental values, the 0.8% difference in the B constant reflects the small difference between the calculated and observed dihedral angles of puckering. The I_b moment of inertia, which has its axis passing through the two carbon atoms for the D_{2h} structure, is most affected by the value of the puckering coordinate. Table 1 also compares the bond distances and angles reported in the microwave work to calculated values from this study, and the agreement is very good. A very interesting feature of the 13DSCB structure is that the CSiC angles are larger than the SiCSi angles. This was first observed in the microwave work where the CSiC angle was reported to be $92.33 \pm 0.23^\circ$. The calculated value here is 90.0° and the SiCSi angle is 87.6° . This is counter-intuitive as the CSiC angle is expected to be more flexible as it has a smaller force constant. However, Kubota et al.¹⁶ rationalize this result in terms of “bent” C-Si bonds. Another possible explanation involves the partial charges on the ring atoms. As discussed later, the carbon atoms have greater partial negative charges (-0.49) than the silicon atoms have partial positive charges (+0.35). Hence, the carbon atoms will have a tendency to push each other further apart than do the silicon atoms, thereby expanding the CSiC angles.

ASSIGNMENT OF SPECTRA

Figures 4 and 5 compare the calculated infrared and Raman spectra, respectively, of 13DSCB to the experimental liquid phase spectra. The vapor-phase spectra, which are

Table 1: Rotational constants (in GHz) and structural parameters of 13DSCB- h_4 and 13DSCB- d_4

Rotational Constants		13DSCB- h_4						13DSCB- d_4									
		MP2/CC-PVTZ			B3LYP/6-311++G(D,P)			MP2/CC-PVTZ			B3LYP/6-311++G(D,P)			Experimental ^a			
		C_{2v}	D_{2h}	C_{2v}	D_{2h}	C_{2v}	D_{2h}	C_{2v}	D_{2h}	C_{2v}	D_{2h}	C_{2v}	D_{2h}	C_{2v}	D_{2h}	C_{2v}	
A		7.2227598	7.1834176	7.1805493	7.1748016	6.6694736	6.6320036	6.6280897	6.6218617	6.67934814							
B		4.0309313	4.0157067	3.9619868	3.9561814	3.3697376	3.3496200	3.3068958	3.3007636	3.39634528							
C		2.9109464	2.8360646	2.8241468	2.8059108	2.6265841	2.5605183	2.5481049	2.5320080	2.62452175							
Parameters (in Angstroms and degrees)																	
		Parameter	MW ^b	DFT ^c	TZ ^d	Parameter	MW ^e	DFT ^e	TZ ^d								
	r_{C-Si}		1.896	1.910	1.901	r_{C-H}	1.09	1.090	1.092								
	α_{CSiC}		92.3	91.2	90.2	r_{Si-H}	1.48	1.488	1.482								
	α_{HSiH}		108.3	108.6	108.8	α_{HCH}	109.0	108.1	108.9								

^a Reference 16. ^b Microwave (calculated); reference 16. ^c B3LYP/6-311++G(d,p). ^d MP2/CC-PVTZ. ^e Microwave (assumed); reference 16.

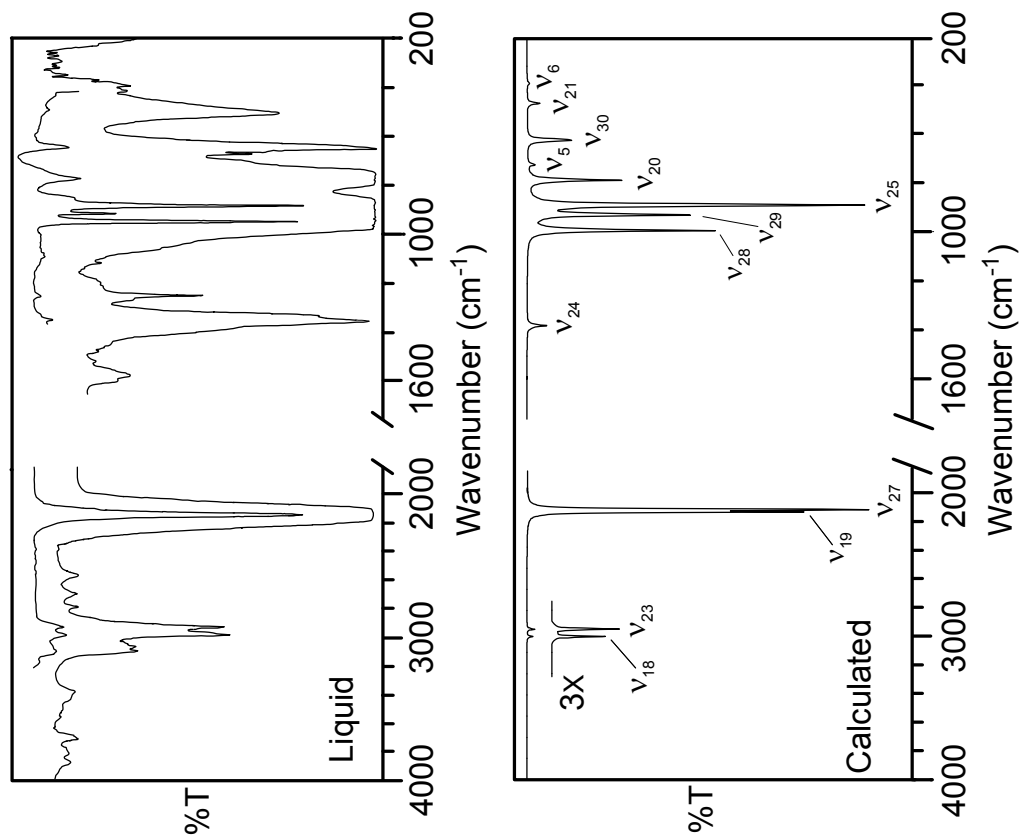


Figure 4. Infrared spectrum of liquid 13DSCB compared to its calculated spectrum.

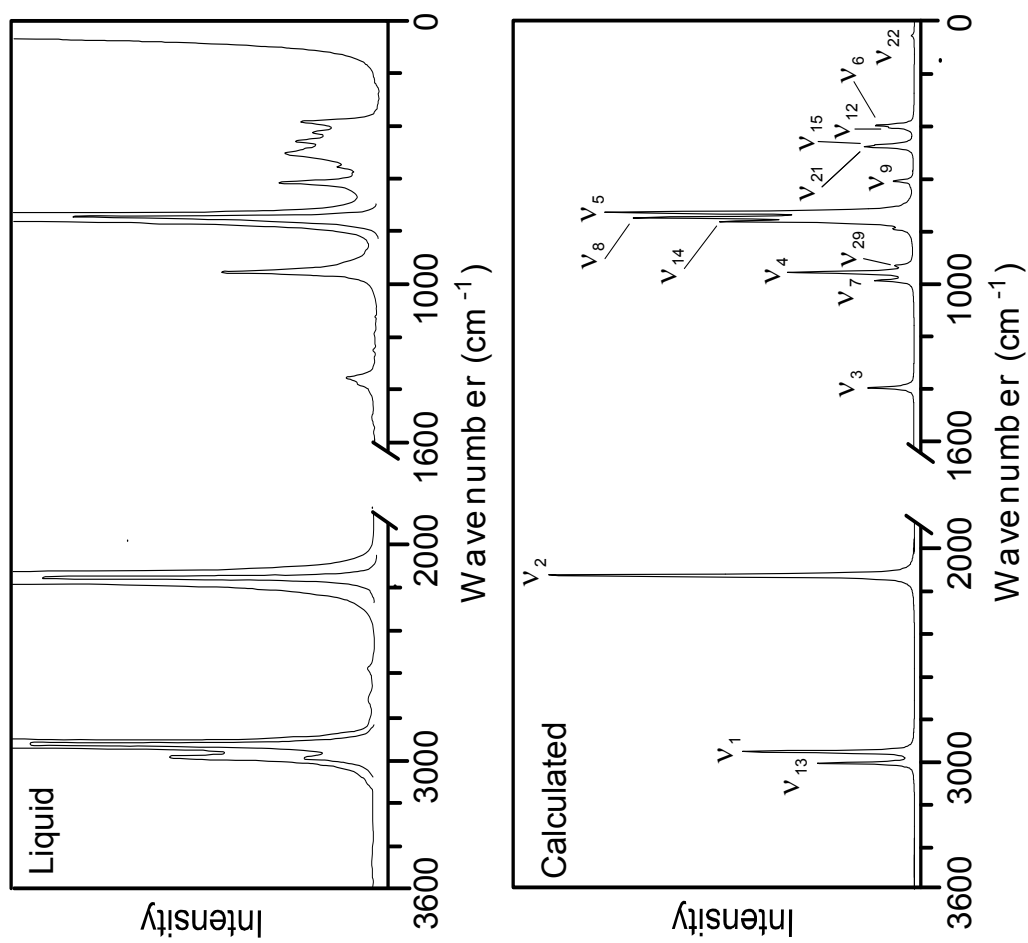


Figure 5. Raman spectrum of liquid 13DSCB compared to its calculated spectrum.

expected to give better frequency agreement, are not shown since the vapor-phase band shapes tend to disguise the intensity correlations. Figures 6 and 7 compare the calculated and experimental spectra for the 13DSCB-1,1,3,3-*d*₄ isotopomer. As can be seen for all cases, both the frequency and the intensity correlations are excellent. Tables 2 and 3 compare the calculated frequencies for both isotopomers to their experimental vapor and liquid values. Several of these have been reassigned based on both frequency and intensity correlations for the C_{2v} structures. These will be discussed below in more detail. The solid state spectra, which correspond to the D_{2h} planar structure, will also be discussed later. In order to confirm the new vibrational assignments, the infrared and Raman bands which were calculated to be the most intense were examined and compared these to the observed spectra for both types of spectra for both molecules. These frequencies for these bands are shown as bold numbers in Tables 2 and 3 and a remarkably good correlation can be seen. The agreement is such that every infrared and Raman band calculated to have substantial intensity in fact does appear prominently in the spectra very close to the predicted frequency value. This excellent agreement for these intense bands is especially important because, as Tables 2 and 3 show, the calculated CH₂ wagging and twisting frequencies, which mostly have very weak intensities, are at unexpectedly low values. Conventional wisdom places these in the 1100-1300 cm⁻¹ range with the wagging motions about 100 cm⁻¹ higher than the twists. However, 13DSCB has its calculated wags at 988(*v*₇) and 996 cm⁻¹ (*v*₂₈) and the twists at 976 (*v*₁₁) and 935 cm⁻¹ (*v*₁₆). Except for *v*₂₈ observed at 965 cm⁻¹ for the vapor as a strong infrared band, all of these are predicted to be very weak and thus were difficult to assign without these computations. Previously,¹⁸ the CH₂ wagging and twisting were assigned near 1260 and 1120 cm⁻¹, respectively, based on weak infrared and Raman bands. Colthup, Wiberly, and Daley⁵⁴ state that these modes in general for substituted cyclobutanes should be in the 1245-1220 cm⁻¹ range for the wags and 1250-1050 cm⁻¹ for the twists. For SiCH₂R groups the wag is stated to be in the 1250-1200 cm⁻¹ region. Based on the DFT calculations, however, for 13DSCB these modes are approximately 200 cm⁻¹ lower, and the reason for this will be discussed later. The very weak bands

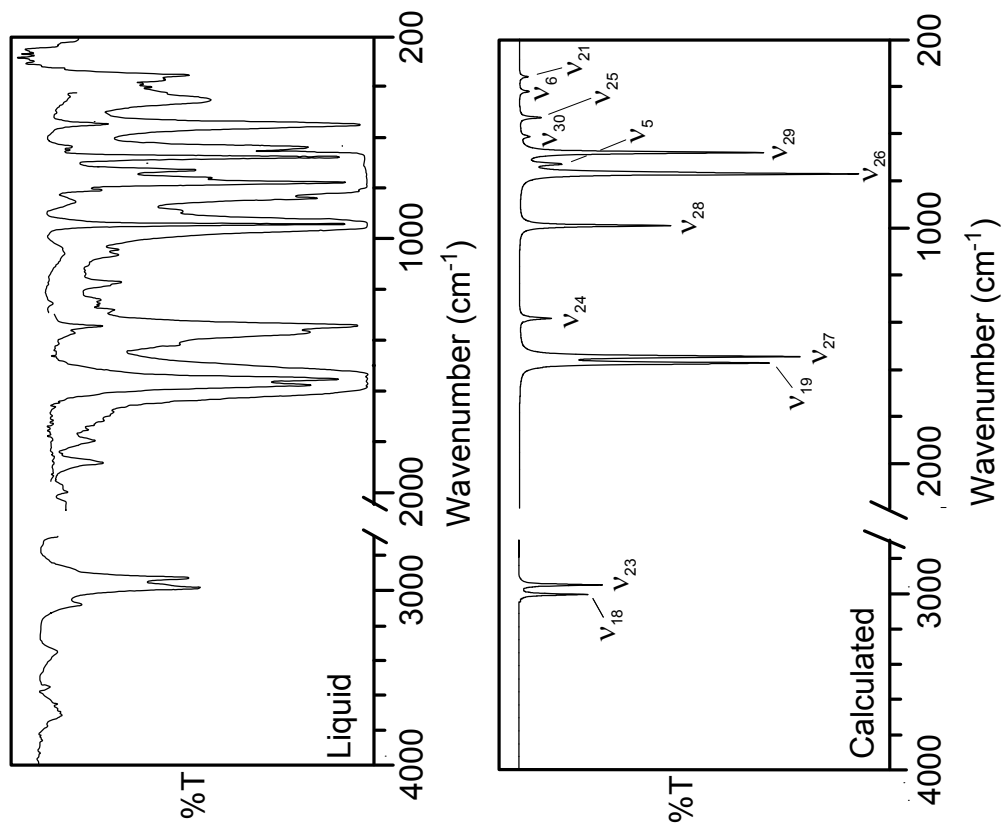


Figure 6. Infrared spectrum of liquid 13DSCB-*d*₄ compared to its calculated spectrum.

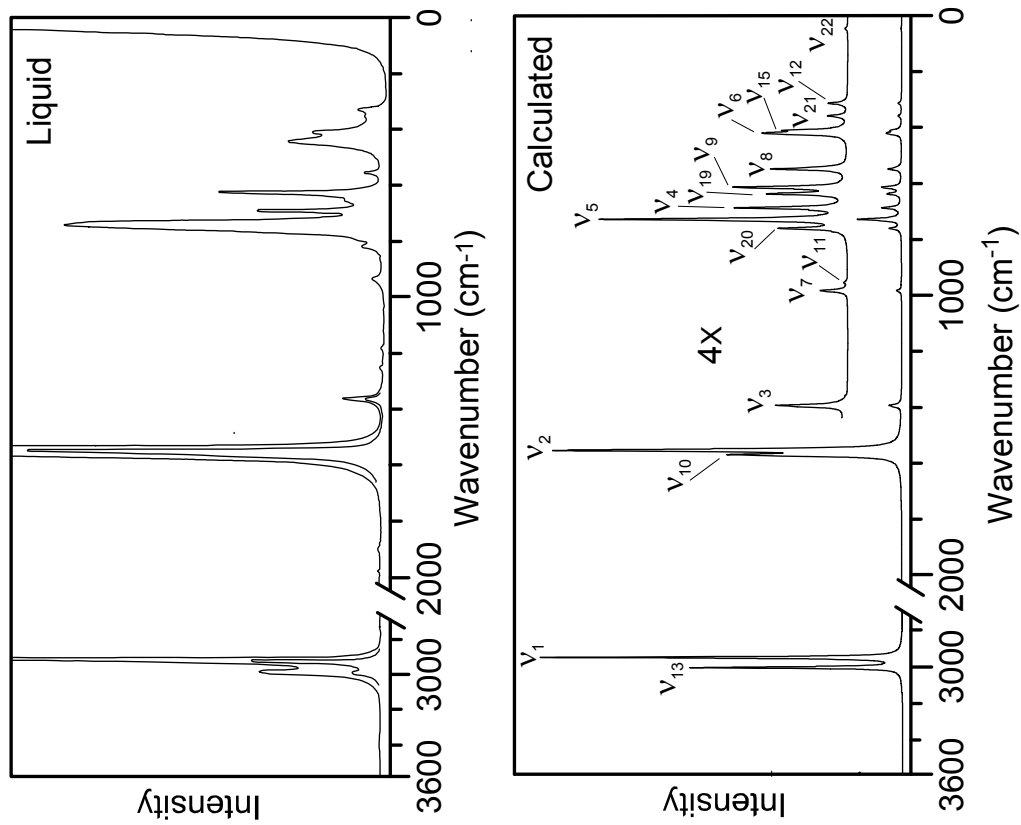


Figure 7. Raman spectrum of liquid 13DSCB-*d*₄ compared to its calculated spectrum.

Table 2: Vibrational assignment (in cm^{-1}) of 13DSCB- h_4 (vapor and liquid)^a

Symmetry		Vapor			Liquid			Calculated ^b
D_{2h}	C_{2v}	ν	Approx. description	IR	Raman ^c	IR	Raman ^c	C_{2v}
A_g	A_1	1	CH_2 sym. str. (ip)	2930 w	2931 (100)	(2920)	2923 (20)	2951 (4, 626)
		2	SiH_2 sym. str. (ip)	2155 s	2156 (1000)	(2169)	2148 (1000)	2125 (140, 1000)
		3	CH_2 deform (ip)		1373 (2)	1355 mw	1355 (5)	1396 (4, 18)
		4	SiH_2 deform (ip)	(965)	965 (11)		958 (32)	956 (7, 47)
		5	Ring breathing	745 m	745 (134)	742 m	749 (311)	728 (22, 109)
		6	Ring deform	380 mw	380 (47)		385 (16)	397 (8, 13)
B_{1g}	A_2	7	CH_2 wag (op)		(965)	(950)	(958)	988 (0, 13)
		8	SiH_2 wag (op)	(745)	(745)	(742)	(760)	747 (0, 91)
		9	Ring mode		620 (3)		617 (15)	609 (0, 8)
B_{2g}	B_1	10	SiH_2 antisym. str. (op)	(2155)	(2156)	(2169)	(2148)	2129 (10, 450)
		11	CH_2 twist (ip)	(965)	(965)	(950)	(958)	976 (9, 1)
		12	SiH_2 rock (op)	(380)	(380)		429 (10)	406 (0.4, 6)
B_{3g}	B_2	13	CH_2 antisym. str. (op)	2995 w	2989 (10)	(2980)	2981 (44)	3004 (7, 287)
		14	CH_2 rock (op) [*]	(745)	(745)	(775)	760 (50)	762 (2, 61)
		15	SiH_2 twist (ip) [*]	442 mw	442 (3)	(440)	460 (10)	469 (1, 10)
A_u	A_2	16	CH_2 twist ((op)			(918)	(928)	935 (0, 0.1)
		17	SiH_2 twist (op)				555 (3)	571 (0, 0.2)

Table 2: (Continued)^a

Symmetry		Vapor			Liquid		Calculated ^b	
D _{2h}	C _{2v}	v	Approx. description	IR	Raman ^c	IR	Raman ^c	C _{2v}
B _{1u}	A ₁	18	CH ₂ antisym. str. (ip)	2965 m	2950 (52)	2980 w	(2981)	3003 (13, 90)
		19	SiH ₂ antisym. str. (ip)	2157 vvs	(2156)	2169 vvs	(2148)	2133 (709, 311)
		20	CH ₂ rock (ip) [*]	~780 ms		775 m	(760)	792 (293, 4)
		21	SiH ₂ rock (ip) [*]	438 mw	446 (13)	~440 vw	(460)	478 (38, 16)
		22	Ring puckering	56	56			54 (7, 1)
B _{2u}	B ₂	23	CH ₂ sym. str. (op)	2930 w	(2931)	2920 w	(2923)	2950 (21, 23)
		24	CH ₂ deform (op)	1363 mw	(1373)	1330 mw		1384 (62, 1)
		25	SiH ₂ wag (ip)	905 s	905 (1)	886 vs	875 (1)	893 (1000, 0)
		26	Ring mode	(644)	(620)		(617)	636 (6, 0.2)
B _{3u}	B ₁	27	SiH ₂ sym. str. (op)	2147 vvs	2147 (44)	(2169)	(2148)	2117 (933, 48)
		28	CH ₂ wag (ip)	965 s	(965)	950 vs	(958)	996 (561, 0.1)
		29	SiH ₂ deform (op)	928 m		918 m	928 (5)	931 (493, 5)
		30	Ring mode	644 m		650 m		627 (135, 0.5)

^a w, weak; m, medium; s, strong; v, very; ip, in-phase, op, out-of-phase; the intensities of frequencies in parentheses result primarily from another vibration at that frequency; ^b frequencies were calculated using B3LYP/6-311++G(D,P) level of theory and the values in the parentheses are the calculated relative IR and Raman intensities respectively. ^c values in the parentheses are relative Raman intensities. ^{*} These vibrational modes next to each other are strongly coupled.

Table 3: Vibrational assignment (in cm^{-1}) of $^{13}\text{DSCB-}d_4$ (vapor and liquid)^a

Symmetry		Vapor			Liquid			Calculated ^b	
D_{2h}	C_{2v}	ν	Approx. description	IR	Raman ^c	IR	Raman ^c	C_{2v}	C_{2v}
A_g	A_1	1	CH_2 sym. str. (ip)	(2930)	2920 (53)	(2925)	2925 (37)	2950 (0.6, 100)	
		2	SiD_2 sym. str. (ip)	(1554)	1554 (100)	(1549)	1555 (100)	1556 (0, 97)	
		3	CH_2 deform (ip)		1370 (3)	1368 vw	1363 (3)	1396 (0.6, 4)	
		4	SiD_2 deform (ip)	(692)	695 (20)	(678)	695 (7)	689 (0.1, 6)	
		5	Ring breathing		754 (65)	730 m	750 (22)	730 (11, 13)	
		6	Ring deform	441 vw	439 (23)	~420 vw	445 (12)	423 (3, 4)	
B_{1g}	A_2	7	CH_2 wag (op)		940 (2)	(940)	940 (1)	986 (0, 1)	
		8	SiD_2 wag (op)		546 (1)		555 (2)	549 (0, 4)	
		9	Ring mode		620 (7)		(629)	616 (0, 6)	
B_{2g}	B_1	10	SiD_2 antisym. str. (op)	(1576)	1579 (74)	(1575)	1568 (50)	1573 (0.5, 39)	
		11	CH_2 twist (ip)		(940)		(940)	956 (0.01, 0.2)	
		12	SiD_2 rock (op)		332(2)	352 w	330(2)	315 (0.02, 1)	
B_{3g}	B_2	13	CH_2 antisym. str. (op)	2972 vvw	2974 (4)	(2982)	2985 (11)	3004 (1, 46)	
		14	CH_2 rock (op) [*]		635 (7)	(640)	629 (12)	639 (0, 4)	
		15	SiD_2 twist (ip) [*]		428 (6)	(420)	411 (4)	412 (0.03, 3)	
A_u	A_2	16	CH_2 twist ((op)		(428)	450 mw?	(411)	894 (0, 0)	
		17	SiD_2 twist (op)					425 (0, 0.1)	

Table 3: (Continued)^a

Symmetry		Vapor			Liquid			Calculated ^b
D _{2h}	C _{2v}	v	Approx. description	IR	Raman ^c	IR	Raman ^c	C _{2v}
B _{1u}	A ₁	18	CH ₂ antisym. str. (ip)	2950 vvw	2941 (24)	2982 mw	(2985)	3003 (2, 15)
		19	SiD ₂ antisym. str. (ip)	1576 vvs	1574 (17)	1575 vvs	(1568)	1575 (75, 4)
		20	CH ₂ rock (ip) [*]	(791)	795 (1)	(780)	792 (1)	763 (22, 3)
		21	SiD ₂ rock (ip) [*]	344 vw	344 (4)	360 vw	360 (1)	361 (3, 1)
		22	Ring puckering	52	52			48 (1, 0.1))
B _{2u}	B ₂	23	CH ₂ sym. str. (op)	2930 vw	(2920)	2925 mw	(2925)	2950 (3, 4)
		24	CH ₂ deform (op)	1339 m		1340 mw		1384 (10, 0.2)
		25	SiD ₂ wag (ip)	543 m	(546)	548 m	(555)	533 (7, 0.02)
		26	Ring mode	791 vvw	(795)	780 s	(792)	771 (100, 0.1)
B _{3u}	B ₁	27	SiD ₂ sym. str. (op)	1554 vvs	1556 (15)	1549 vvs	(1555)	1548 (86, 1)
		28	CH ₂ wag (ip)	951 vvs		943 s	(940)	991 (48, 0.02)
		29	SiD ₂ deform (op)	692 vvs	685 (4)	678 s		683 (76, 0.2)
		30	Ring mode	629 m	(620)	640 m	(629)	614 (3, 0.2)

^a see the footnotes of Table 2 for abbreviations.

near 1120 and 1260 cm^{-1} , previously assigned to the twists and wags, are apparently overtone or combination bands. For example, the former is likely $\nu_5 + \nu_6$ ($745 + 380 = 1125 \text{ cm}^{-1}$) and the later $\nu_9 + \nu_{30}$ ($620 + 644 = 1266 \text{ cm}^{-1}$). For the d_4 isotopomer the wags and the twists are calculated to be at 986 (ν_7), 991 (ν_{28}), 956 (ν_{11}), and 894 cm^{-1} (ν_{16}), respectively. Again, all but ν_{28} , which is a very strong band in the infrared at 951, are predicted to have negligible intensity.

ANOMALOUS CH₂ WAGGING AND TWISTING FREQUENCIES

As mentioned above, the CH₂ wagging frequencies for the h_4 molecule of 988 (ν_7 calculated) and 965 (ν_{28}) cm^{-1} and the twisting frequencies of 976 (ν_{11} calculated) and 935 (ν_{16} calculated) cm^{-1} are far below those typically observed. Notably, the CH₂ deformations at 1373 (ν_3) and 1363 (ν_{24}) cm^{-1} and the CH₂ rocks at 760 (ν_{15}) and 780 (ν_{20}) cm^{-1} are not outside their normal ranges. The anomalous wagging and twisting frequencies can be understood by considering the partial charges on the hydrogen atoms attached to the carbon and silicon atoms, as shown in Figure 8. The hydrogens on carbon have partial positive charges while those on silicon are partially negative charged due to the electropositive nature of the silicon atoms. The values for the charges in the figure are from the *ab initio* calculations. The sideways motions of the positively charged carbon hydrogen atoms during a twisting or wagging motion brings them closer to the negatively charged hydrogens on the silicon atoms. Hence, this attraction between opposite charges counteracts the usual increase in the potential energy away from the equilibrium positions of the CH₂ groups. The steepness of the potential energy curve is thus decreased and lower vibrational frequencies result. A previous study⁵⁵ suggested that decreased frequencies for these types of modes might result, but here a very clear evidence for these unprecedented low values is seen.

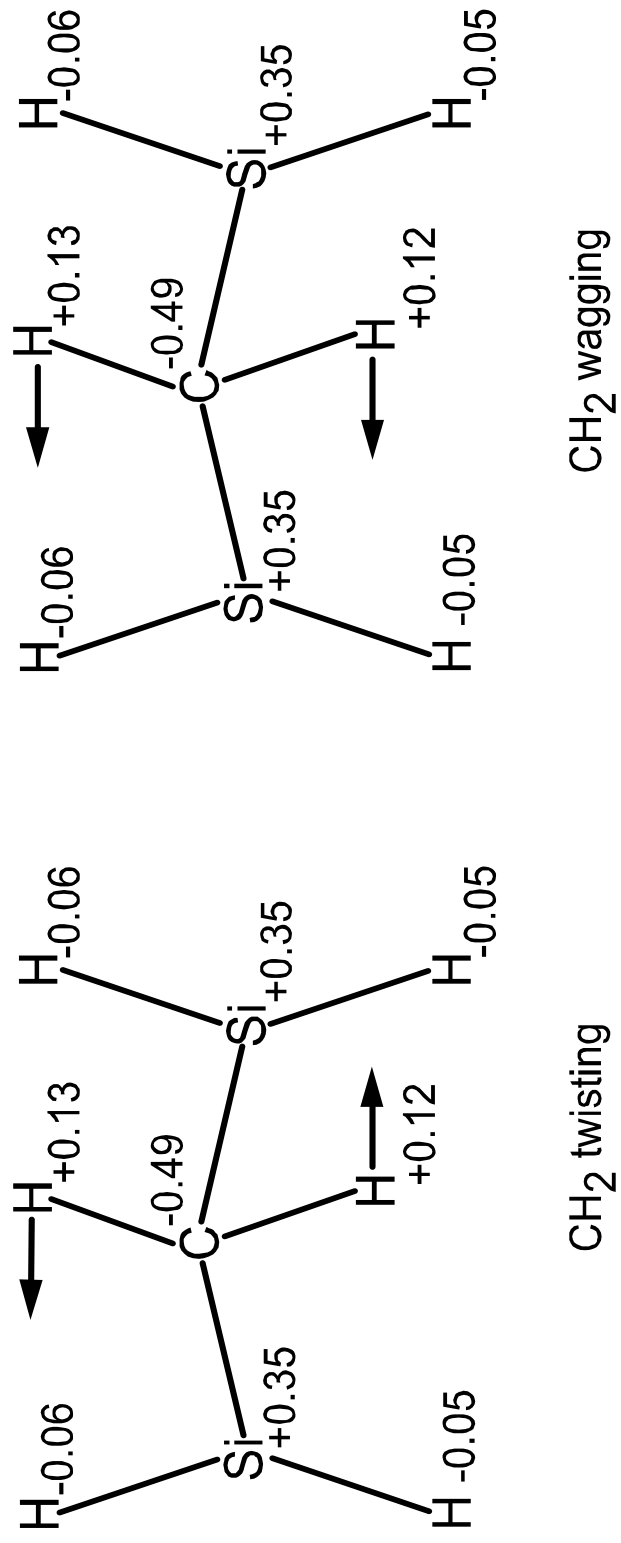


Figure 8. CH₂ twisting and wagging vibrations of 13DSCB and the partial charges calculated for each atom. The attraction between unlike charges lowers the frequencies of these two vibrational modes.

STRUCTURAL CONVERSION IN THE SOLID PHASE

As postulated previously, 13DSCB converts from C_{2v} symmetry (puckered) to D_{2h} (planar) in the solid phase. Tables 4 and 5 compare the calculated D_{2h} frequencies to those of solid 13DSCB- h_4 and $-d_4$. Since the vapor-phase structure for the independent molecule is not planar, the calculated ring-puckering frequency is imaginary.

Figure 9 shows the Raman spectra of the vapor, liquid, and solid 13DSCB- h_4 and $-d_4$ in the low-frequency region. The dramatic change in ν_6 , the ring angle bending, from 380, to 385, to 422 cm^{-1} in going from the vapor, to liquid, to solid phases can be seen. For the $-d_4$ molecule, the corresponding values are 441, 445, and 406 cm^{-1} . At the same time ν_{21} , the SiH_2 in-phase rocking, has values of 436 (vapor), 440 (liquid, from the infrared), and 465 cm^{-1} (solid) for 13DSCB- h_4 and 344, 360, and 381 cm^{-1} (solid) for the $-d_4$ isotopomer. The large change in the frequencies for the solid results from the fact that ν_6 and ν_{21} are now of different symmetry species (A_g and B_{1u}) and can no longer interact as their motions are orthogonal. In the puckered C_{2v} structure both vibrations are of A_1 symmetry species and the up and down motion of the SiH_2 rocking can easily interact with the angle bendings which now have a component perpendicular to the original plane of the molecule. This is all depicted in Figure 9 where the calculated frequencies for both isotopomers are shown for C_{2v} and D_{2h} symmetries. For D_{2h} the A_g (ν_6) and B_{1u} (ν_{21}) modes have similar frequencies for both isotopomers, but they are pushed apart for the C_{2v} (vapor) cases. In the vapor-phase the potential energy distribution for ν_{21} at 436 cm^{-1} is 0.70 SiH_2 rock and 0.28 angle bending while ν_6 is 0.67 bending and 0.28 rock for the h_4 isotopomer. For the planar solid, ν_{21} and ν_6 are almost purely the rock and bend, respectively. These values are shown in Figure 10. Similarly, for the d_4 isotopomer, ν_6 is 0.73 bending, 0.22 rocking, while ν_{21} is 0.72 rocking and 0.26 bending. The vibrations again become nearly “pure” for the planar C_{2v} form. It is very reassuring that the assessments made in 1977, based on force constant calculations, was just the same, and now this phase-dependent structure of 13DSCB has been

Table 4: Vibrational assignment (in cm^{-1}) of 13DSCB- h_4 (solid)^a

Symmetry		v	Approx. description	Solid		Calculated ^b
D _{2h}	IR			Raman ^c	D _{2h}	
A _g	1	CH ₂ sym. str. (ip)	(2925)	2918 (199)	2954 (0, 531)	
	2	SiH ₂ sym. str. (ip)	(2140)	2146 (1000)	2124 (0, 1000)	
B _{1g}	3	CH ₂ deform (ip)	1360 m	1349 (11)	1395 (0, 14)	
	4	SiH ₂ deform (ip)	(955)	949 (42)	955 (0, 41)	
	5	Ring breathing		740 (500)	725 (0, 92)	
	6	Ring angle bending	419 vw	422 (65)	417 (0, 19)	
B _{2g}	7	CH ₂ wag (op)	(955)	(949)	989 (0, 11)	
	8	SiH ₂ wag (op)	(768)	767 (75)	754 (0, 75)	
	9	Ring mode		607 (6)	608 (0, 6)	
B _{3g}	10	SiH ₂ antisym. str. (op)	(2140)	2156 (55)	2126 (0, 430)	
	11	CH ₂ twist (ip)	(955)	(949)	974 (0, 1)	
B _{3g}	12	SiH ₂ rock (op)		(422)	401 (0, 6)	
	13	CH ₂ antisym. str. (op)	(2968)	2971 (97)	3001 (0, 266)	
	14	CH ₂ rock (op) [*]		(767)	762 (0, 51)	
A _u	15	SiH ₂ twist (ip) [*]	(465)	450 (11)	468 (0, 7)	
	16	CH ₂ twist ((op)	(928)		933 (0, 0)	
	17	SiH ₂ twist (op)		562 (1)	578 (0, 0)	

Table 4: (Continued)^a

Symmetry		Solid			Calculated ^b
D _{2h}	ν	Approx. description	IR	Raman ^c	D _{2h}
B _{1u}	18	CH ₂ antisym. str. (ip)	2968 w	2962 (62)	3000 (16, 0)
	19	SiH ₂ antisym. str. (ip)	(2140)	2162 (8)	2128 (852, 0)
	20	CH ₂ rock (ip) [*]	768 s	(767)	786 (309, 0)
	21	SiH ₂ rock (ip) [*]	465 w	465 (17)	457 (47, 0)
	22	Ring puckering	-----	-----	<i>i</i>
B _{2u}	23	CH ₂ sym. str. (op)	2925 w	2920 (146)	2954 (25, 0)
	24	CH ₂ def (op)	1338 m	(1349)	1383 (67, 0)
	25	SiH ₂ wag (ip)	880 vs	875 (1)	895 (1000, 0)
	26	Ring mode	(650)	617 (85)?	637 (8, 0)
B _{3u}	27	SiH ₂ sym. str. (op)	2140 vvs	2140 (200)	2115 (920, 0)
	28	CH ₂ wag (ip)	955 vs		994 (585, 0)
	29	SiH ₂ deform (op)	928 s	927 (4)	931 (465, 0)
	30	Ring mode	650 s	646 (1)	627 (136, 0)

^a see the footnotes of Table 2 for abbreviations

Table 5: Vibrational assignment (in cm^{-1}) of 13DSCB- d_4 (solid)^a

Symmetry		v	Approx. description	Solid		Calculated ^b
D _{2h}	IR			Raman ^c	D _{2h}	
A _g	1	CH ₂ sym. str. (ip)	(2920)	2920 (63)	2954 (0, 100)	
	2	SiD ₂ sym. str. (ip)	(1549)	1555 (100)	1554 (0, 91)	
	3	CH ₂ deform (ip)	1357 m	1355 (8)	1394 (0, 3)	
	4	SiD ₂ deform (ip)	(672)	688 (15)	689 (0, 6)	
	5	Ring breathing	(740)	740 (101)	733 (0, 15)	
B _{1g}	6	Ring angle bending		406 (25)	400 (0, 4)	
	7	CH ₂ wag (op)	(940)	(945)	987 (0, 1)	
	8	SiD ₂ wag (op)	(560)	555 (1)	553 (0, 4)	
	9	Ring mode		617 (6)	619 (0, 6)	
B _{2g}	10	SiD ₂ antisym. str. (op)	(1570)	1564 (56)	1570 (0, 40)	
	11	CH ₂ twist (ip)	(940)	945 (2)	953 (0, 0.2)	
B _{3g}	12	SiD ₂ rock (op)	353 vw	350 (2)	311 (0, 1)	
	13	CH ₂ antisym. str. (op)	(2960)	2974 (56)	3001 (0, 50)	
	14	CH ₂ rock (op) [*]		638 (59)	635 (0, 4)	
	15	SiD ₂ twist (ip) [*]	420 vw	419 (12)	413 (0, 2)	
A _u	16	CH ₂ twist (op)			891(0, 0)	
	17	SiD ₂ twist (op)	450 mw?	454 (2)?	429 (0, 0)	

Table 5: Continued^a

Symmetry		v	Approx. description	Solid		Calculated ^b	
D _{2h}	IR			Raman ^c	D _{2h}		
B _{1u}		18	CH ₂ antisym. str. (ip)	2960 m	2962 (19)	3000 (2, 0)	
		19	SiD ₂ antisym. str. (ip)	1570 vs	1574 (13)	1573 (75, 0)	
		20	CH ₂ rock (ip) [*]	740 m	(740)	751 (31, 0)	
		21	SiD ₂ rock (ip) [*]	381 mw	(406)	383 (6, 0)	
		22	Ring puckering			<i>i</i>	
B _{2u}		23	CH ₂ sym. str. (op)	2920 m	2925 (41)	2954 (4, 0)	
		24	CH ₂ deform (op)	1326 m		1383 (10, 0)	
		25	SiD ₂ wag (ip)	560 ms	(555)	535 (6, 0)	
		26	Ring mode	772 s		770 (100, 0)	
B _{3u}		27	SiD ₂ sym. str. (op)	1549 vs		1546 (84, 0)	
		28	CH ₂ wag (ip)	940 s	(945)	989 (47, 0)	
		29	SiD ₂ deform (op)	672 s	(688)	683 (75, 0)	
		30	Ring mode	640 m		614 (3, 0)	

^a see the footnote of Table 2 for abbreviations

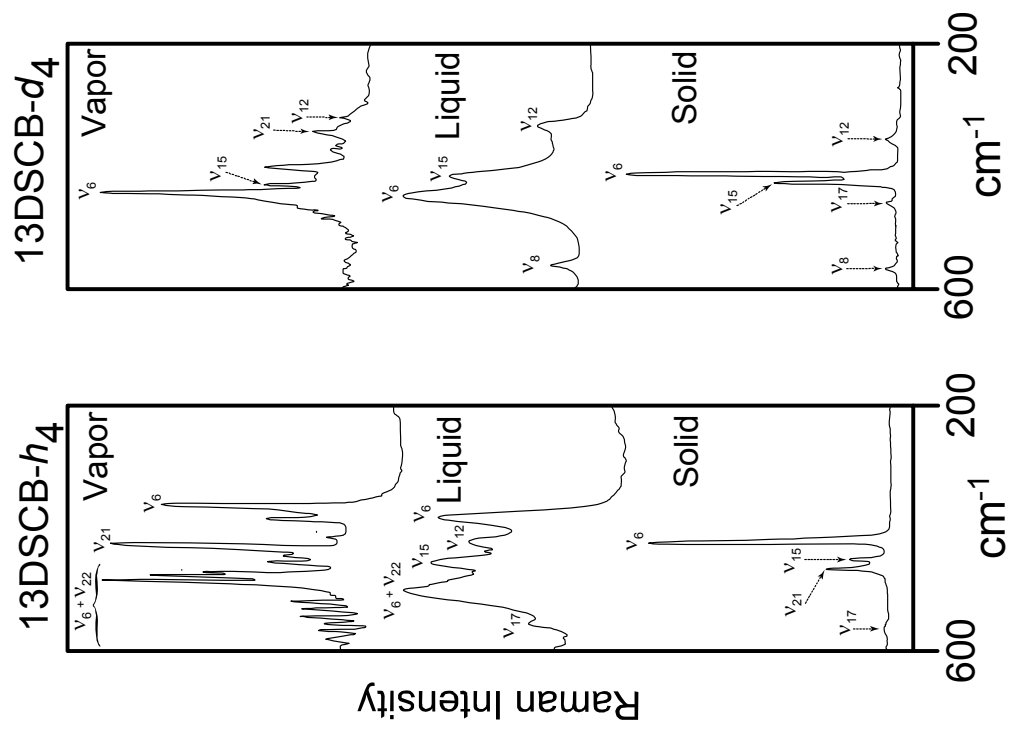


Figure 9. Raman spectra of 13DSCB-*h*₄ and -*d*₄ for its vapor, liquid, and solid (77 K) in the 200-600 cm⁻¹ region.

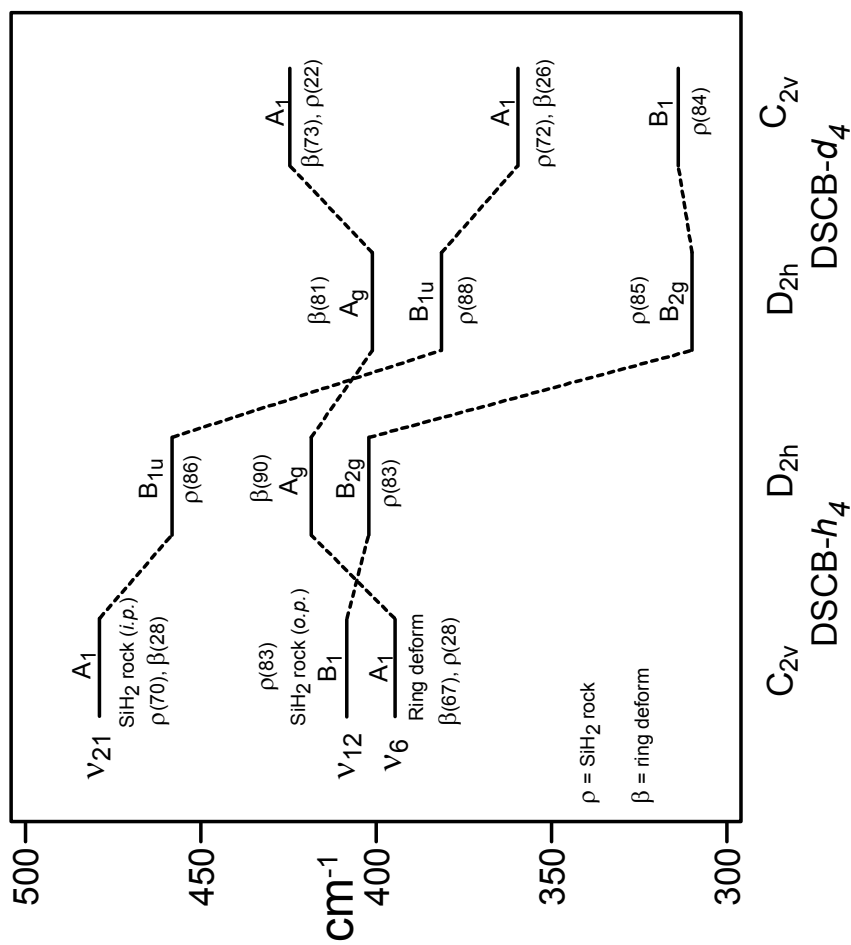


Figure 10. Correlation diagram for ν_6 (ring-angle bending), ν_{12} (SiH₂ out-of-phase rocking), and ν_{21} (SiH₂ in-phase rocking) for DSCB- h_4 and $-d_4$ for their C_{2v} (puckered vapor) and D_{2h} (planar solid) structures. For C_{2v} symmetry ν_6 and ν_{21} interact; for D_{2h} they do not. β and ρ indicate the percent potential energy distribution from the ring bending and SiH₂ rocking modes respectively.

reconfirmed. It should be added that no other type of analysis could have been used to ascertain the structure and symmetry changes of this molecule in the solid since it would not have been possible to grow crystals of the molecule at low temperatures for crystallography studies.

CONCLUSION

¹³DSCB is a most fantastic molecule. It has apparently only been prepared in this laboratory and that was three decades ago. It has several highly unusual features. First, the CSiC angles are larger than the SiCSi angles although the force constant for the former is typically much smaller, and therefore these angles should be able to accommodate the angle strain in the ring to a greater extent. This is not the case, however, possibly because of charge repulsions across the four-membered ring. Second, the CH₂ wagging and twisting frequencies for ¹³DSCB are the lowest by far of any that is aware of. This results from charge attractions between neighboring hydrogen atoms. The third unusual feature of ¹³DSCB is its change in structure in the solid phase. The DFT calculations beautifully confirm the earlier conclusions about the changes in vibrational coupling. The structural change itself is not so surprising as planar ¹³DSCB molecules can obviously stack together better in the solid than can puckered ones. Since the energy barrier between the C_{2v} and the D_{2h} is so small (0.25 kcal/mole) for the individual molecules in the vapor, even tiny intermolecular interactions in the solid phase can easily squelch out this energy difference between the two conformations. The effect on the spectra, however, has been lovely to see.

CHAPTER V

EXPERIMENTAL AND CALCULATED VIBRATIONAL FREQUENCIES OF THE ELECTRONIC GROUND STATE OF 2-CYCLOHEXEN-1-ONE AND ITS 2,6,6-*d*₃ ISOTOPOMER

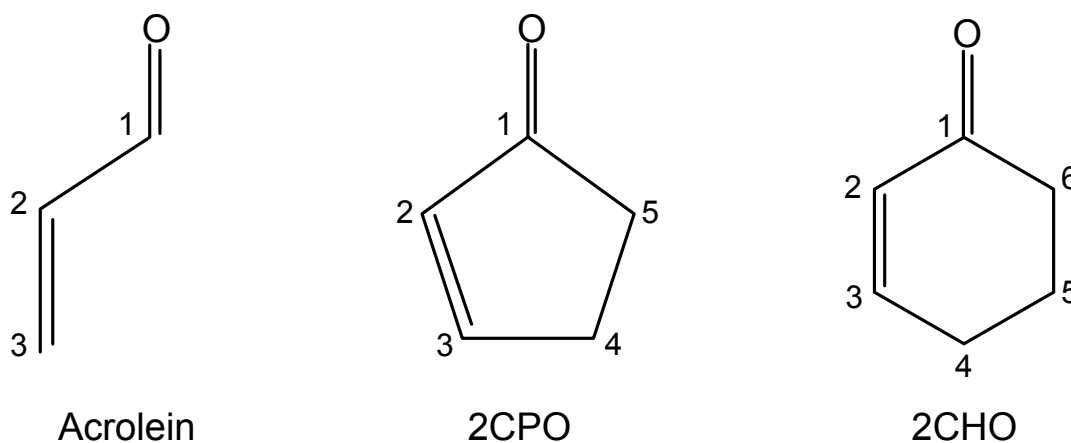
INTRODUCTION

Photochemistry of carbonyl compounds has drawn the attention of chemists due to various structural changes and chemical reactions they can undergo in their electronic excited states. In 1953, Walsh⁵⁶ predicted that the carbonyl carbon of formaldehyde can be distorted from a planar to a pyramidal structure in its singlet excited state. This was later verified spectroscopically by Brand⁵⁷ in 1956. Since then a number of carbonyl compounds have been investigated by spectroscopic and theoretical methods which have characterized their excited state potential energy surfaces (PESs) useful in predicting chemical and physical properties of these compounds.

α,β -Unsaturated ketones or conjugated enones is a class of carbonyl compounds which can undergo numerous photochemical reactions in their higher electronic states, particularly in their triplet excited states. Some of these reactions such as α -cleavage, dimerization, and oxetane formation are very useful in organic syntheses. Acrolein, the simplest of the conjugated enones, has been a subject of numerous computational studies of triplet states.^{58,59} The photochemical properties of acrolein have in turn stimulated the interest of conjugated cyclic enones which have focused on the influence of structural rigidity of these compounds on the life time and reactivity of excited states.

2-Cyclopenten-1-one or 2CPO, a conjugated cyclic enone, is one of the very few molecules whose ground and excited states have been studied in detail by both spectroscopic and theoretical methods. The ground state ring bending PES with a single minimum determined by far-infrared spectroscopy¹⁹ concluded that this molecule is planar and fairly rigid in this state. This rigidity comes from the conjugation between the C=O and C=C groups which overcomes the torsional interactions of the two sp³ hybridized carbons in the ring that favors non-planarity. The ring remains planar in the

singlet excited state (S_1) too,²⁰ but becomes less rigid because of the diminished conjugation. This was resulted by the excitation of a non-bonding electron into an anti-bonding π^* molecular orbital that decreases the bond orders of both C=C and C=O bonds. However, the outcome of the triplet excited state²¹ was quite interesting. The PES of this state was determined by fitting the vibrational energy levels of the ring bending mode observed by cavity ringdown spectroscopy, an ultra-high sensitive technique which is ideal to observe spin forbidden $T_n \leftarrow S_0$ ($n = 1, 2, \dots$) transitions. The double minima of the PES suggest that unlike the other two states, the ring is bent in the T_1 state. This shows that the effect of diminished conjugation is more pronounced in the triplet state and causes the ring to bend.



2-Cyclohexen-1-one or 2CHO is another conjugated cyclic enone which is an asymmetric, non-planar, six membered-ring molecule. In 1970 Manley and Tyler²² reported the microwave spectrum of 2CHO along with its rotational constants and proposed a structure for which only the carbon atom in the 5th position of the ring is significantly out-of-plane. This is again due to the conjugation between C=C and C=O groups which is expected to provide a rigidity to the ring that makes the other carbon atoms in the ring be coplanar. In 1979 Carreira et. Al²³ reported the vapor-phase Raman spectrum of the low frequency region, and concluded that the molecule had an inversion barrier of 935 cm^{-1} . This was based on the assignment where the $0 \rightarrow 2/1 \rightarrow 3$ degenerate

transitions of ν_{39} , the lowest frequency vibration were at 248 cm^{-1} . However, one year later, Smithson and Wieser²⁴ analyzed the vapor-phase far-IR spectrum, which showed a series of Q branches in the $96.9\text{-}99.8\text{ cm}^{-1}$ range. These transitions were fitted to a ring inversion potential function from which a barrier of 3379 cm^{-1} was calculated. A type B band observed at 247 cm^{-1} in the far-IR spectra, was assigned to the second lowest-frequency vibrational mode (ν_{38}).

In order to understand the inversion process better both in the ground and excited electronic states and to carry out a complete vibrational analysis, further spectroscopic and theoretical studies have been undertaken on 2CHO and its 2,6,6- d_3 isotopomer (2CHO- d_3). This chapter presents the vibrational frequencies and modes of 2CHO and 2CHO- d_3 determined by infrared and Raman spectra and by density functional theory (DFT) calculations along with their complete vibrational assignments. The next chapter will discuss the ultraviolet cavity ringdown spectra of 2CHO together with vapor-phase Raman spectra and DFT calculations which were used to determine the structure and the one-dimensional ring inversion potential energy in its ground electronic state. The chapter VII will emphasize the importance of investigating the excited states of conjugated enones and present a further discussion of the cavity ringdown spectra of 2CHO and 2CHO- d_3 which were used to determine their ring inversion potential function in the excited $S_1(n,\pi^*)$ electronic state.

The vibrational assignments of 2CHO and 2CHO- d_3 presented in this chapter are done with the aid of *ab initio* calculations and the modern molecular visualization programs which have now largely replaced the previous use of force constant calculations to carry out such assignments. Spectroscopists have been impressed with the accuracy of some of the recent results⁶⁰⁻⁶² predicted by these computational methods. Accurate vibrational assignments are very useful as they can play important roles in determining molecular structures, conformations and intermolecular forces.

EXPERIMENTAL

2CHO was purchased from Acros (with 99% purity). It has a boiling point of 168⁰ C and a vapor pressure of 1.8 Torr at 25⁰ C. The Raman spectra of 2CHO were acquired on an SA Jobin-Yvon U-1000 spectrometer. Raman scattering was achieved using a Coherent Radiation Innova 20 argon ion laser with an excitation at 514.5 nm. The liquid-phase spectra were recorded at ambient temperature with a lasing power of 1 W. Depolarization measurements were done using a polarizer and a scrambler. Vapor-phase Raman spectra of the sample contained in the previously described high-temperature Raman cell³⁵ were collected at a temperature of 230⁰ C which gives about 600-800 torr of vapor pressure with a laser power of 5 W. The liquid mid-infrared spectra were collected on a Bruker Vertex 70 FT-IR spectrometer. A thin capillary film of the sample between two KBr discs was used for this purpose. 256 scans with a resolution of 1 cm⁻¹ were recorded. The liquid far-infrared spectrum was also collected on the same instrument. 5% (of volume/volume) solution of the sample in carbon disulfide contained in a liquid far-IR cell with polyethylene windows was used here. A total of 128 scans with a 1 cm⁻¹ resolution were recorded. The vapor phase mid-infrared spectra were recorded on a Bomem DA8.02 FT-IR spectrometer. A 4-m multi path IR cell with KBr windows was used in this case. A total of 8192 scans were collected at a resolution of 0.5 cm⁻¹ at ambient temperature.

2CHO-*d*₃ was synthesized at the laboratory of Dr. Stephen Drucker of University of Wisconsin at Eau Claire. It was prepared by combining 2-cyclohexen-1-one (0.1 mol) with D₂O (1.0 mol) and a catalytic amount of D₂SO₄. The mixture was refluxed at 55 °C for 48 hours, and then extracted with dichloromethane. The solvent was removed by rotary evaporation, and the product was distilled. Analysis by NMR and GC-MS indicated that the product contained approximately 70% 2CHO-*d*₃, with the remainder the dideuterated derivatives. The liquid-phase mid-IR and Raman spectra of this were recorded using the same equipment and under the same condition as of 2CHO. However, the exchange of the deuterium atoms of 2CHO-*d*₃ by hydrogen present in moisture was observed. This was very clearly seen in the liquid infrared spectrum which is more

congested than that of the liquid Raman. The mid-infrared spectrum was collected in open air and using hygroscopic KBr discs while there was no exposure to air during the acquisition of Raman spectra. No vapor-phase spectra of 2CHO- d_3 were acquired due to lack of sample.

COMPUTATIONS

The computations presented here were carried out using the Gaussian 03 quantum mechanical package.⁴⁵ Calculation of vibrational frequencies together with infrared and Raman intensities of both 2CHO and 2CHO- d_3 were done using DFT (B3LYP) with the 6-311++G(d,p) basis set. Based on previous research work⁵⁰⁻⁵³ scaling factors of 0.964 for frequencies above 2000 cm^{-1} and 0.985 for frequencies below 2000 cm^{-1} were used. The descriptions of the normal modes were determined by the GaussView 3.0 molecular visualization program.⁶³

MOLECULAR VIBRATIONS

As confirmed by previous studies,²²⁻²⁴ the 2CHO molecule has a non-planar structure with C_1 symmetry. However, to assist with the classification of the vibrational modes, calculations were also done for a hypothetical planar structure of 2CHO with C_s symmetry. This planar structure has a distribution of vibrational modes of

$$21 A' + 18 A'' \quad (5.1)$$

This separates the totally symmetric vibrational modes (in-plane modes) with A' symmetry from the non-totally symmetric ones (out-of-plane modes) with A'' symmetry. This is also helpful in identifying the polarized and depolarized Raman bands since the A' modes tend to be more polarized (and also are more intense).

RESULTS AND DISCUSSION

Figures 11 and 12 compare the vapor and liquid phase infrared and Raman spectra of 2CHO to the computed spectra using the DFT-B3LYP/6-311++G(d,p) level of calculation. There is remarkably good agreement can be seen between the scaled frequencies of the C_1 point group and the experimental values. The vapor-phase frequencies are closer to the computed values than those in the liquid where they are affected by the intermolecular interactions. However, better intensity correlation is seen in the liquid spectra since the vapor-phase band structures (mostly due to the rotational fine structure) may disguise this correlation. Table 6 lists the values of the vibrational frequencies and their intensities. Some of the observed C-H stretching vibrations may be shifted because of Fermi resonance between these modes and the overtones of CH_2 deformations present in organic systems. Therefore, the 2800-3200 cm^{-1} region is less important in giving structural and vibrational information. Also the agreement between the computed and experimental frequencies in this region is not as good. So this region is not discussed in detail. As stated before, the approximate descriptions of the normal modes were determined by the GaussView molecular modeling program which shows the atomic motions of each vibration. Strong coupling can be seen for many of the vibrations, especially the low frequency ones of the C_1 structure. The most coupled vibrations are indicated with asterisks in Table 6. The calculated values for C_s symmetry are also presented in Table 6 to compare the two sets of calculated frequencies. Careful analysis shows that most of the modes which show significant frequency differences are the ones which involve the motion of the ring skeleton (e.g. ν_{16} , ν_{17} , ν_{18} , ν_{19} and ν_{21}). Therefore, it is evident that imposing a constraint to the ring structure limits the coupling between the “in-plane” and “out-of-plane” motions. The two imaginary values calculated for ν_{38} and ν_{39} for the C_s point group reflect the fact that this is not the minimum energy structure.

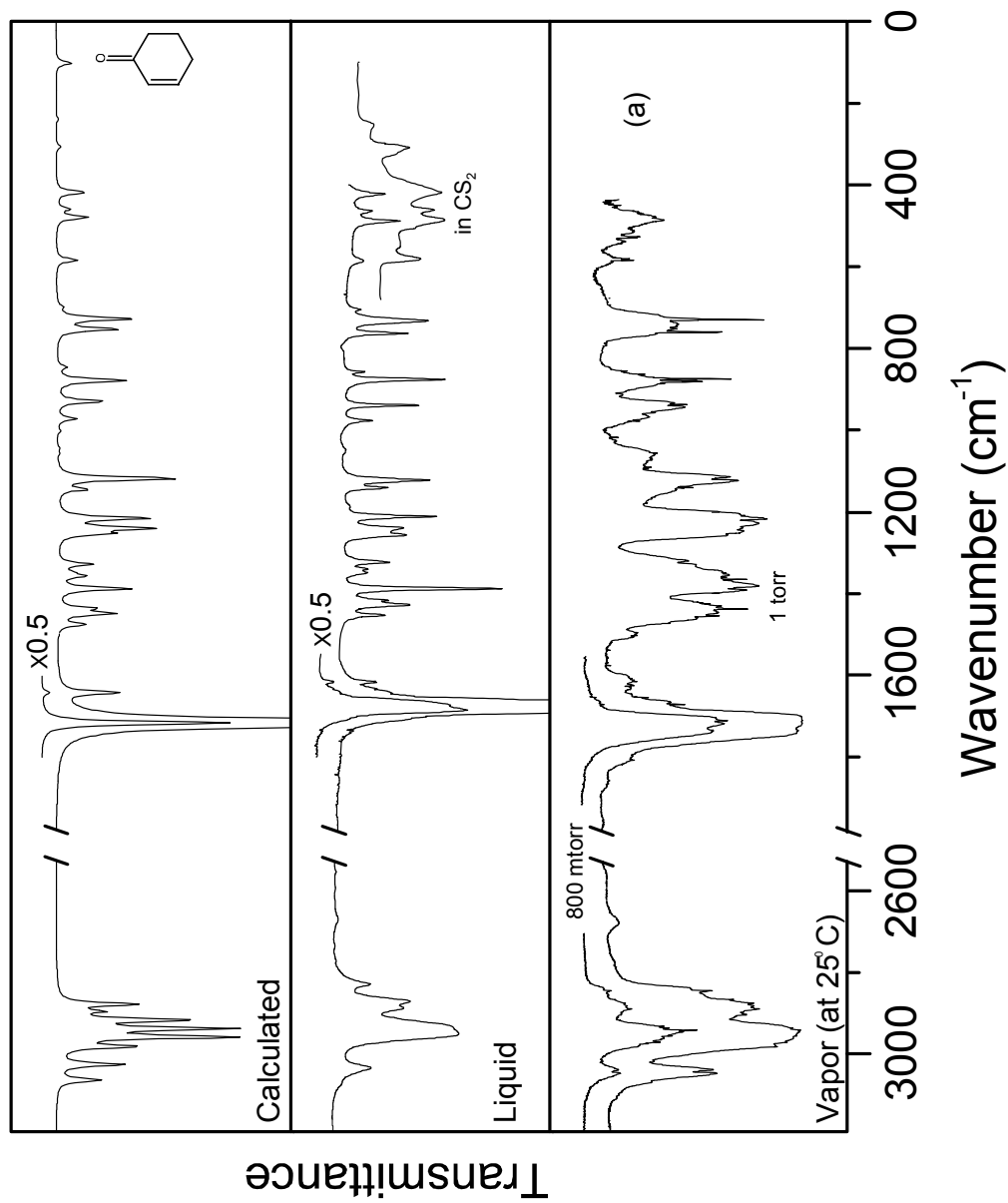


Figure 11. Liquid and vapor-phase infrared spectra of 2CHO compared to its calculated DFT spectrum. (a) The infrared spectrum below 400 cm^{-1} is reported in reference 24.

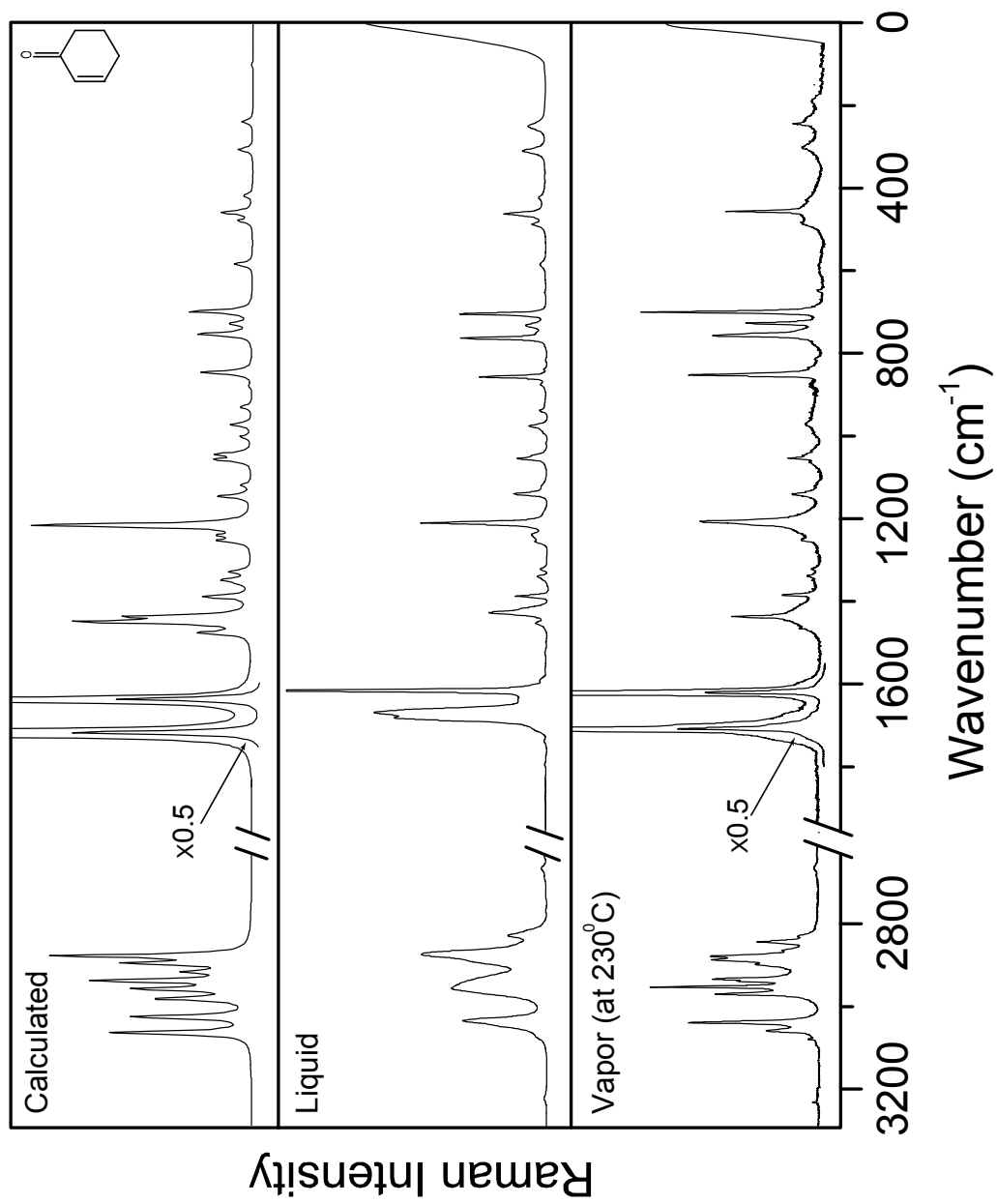


Figure 12. Liquid and vapor-phase Raman spectra of 2CHO compared to its calculated DFT spectrum.

Table 6: Vibrational assignment (in cm^{-1}) of 2-cyclohexen-1-one^a

Sym. $C_s (C_1)$	ν $C_s \quad C_1$	Approx. description	Liquid			Vapor			Calculated ^c		
			Infrared	Raman ^b		Infrared	Raman ^b		$C_s (I_{IR}, I_{Ram})$	$C_1 (I_{IR}, I_{Ram})$	ρ
A' (A)	1	=C-H str.	----	3046 sh	----	3059 (35)	----	3063 (3, 62)	3064 (3, 76)	0.19	
	2	=C-H str.	3034 ms	3035 (32) P	3043 s	3039 (96)	----	3017 (5, 54)	3026 (4, 61)	0.37	
	3	CH ₂ sym. str.	----	----	----	2934 (61)	----	2947 (9, 100)	2916 (8, 29)	0.39	
	4	CH ₂ sym. str.	2887 ms	2888 sh	2889 w	2887 (39)	----	2932 (7, 19)	2895 (2, 59)	0.17	
	5	CH ₂ sym. str.	2871 s	2879 (57) P	2875 w	2879 (57)	----	2899 (7, 78)	2878 (5, 100)	0.16	
	6	C=O stretch	1686 vvs	1681/1669 ^d P	1712 vs	1709 (91)	----	1705 (100, 35)	1718 (100, 33)	0.37	
	7	C=C stretch	1617 w	1616 (100) P	1625 vw	1621 (83)	----	1660 (4, 24)	1644 (4, 26)	0.09	
	8	CH ₂ deform	----	----	----	----	----	1492 (3, 3)	1477 (2, 3)	0.67	
	9	CH ₂ deform	1454 m	1453 (4) D	1455 m	----	----	1447 (4, 12)	1451 (4, 9)	0.47	
	10	CH ₂ deform	1428 ms	1428 (16) P	1438 s	1436 (21)	----	1439 (0.5, 4)	1438 (2, 6)	0.72	
	11	=C-H in-plane wag	1388 vs	1387 (10) P	1388 vs	1384 (8)	----	1399 (6, 2)	1390 (5, 3)	0.53	
	12	CH ₂ wag	1349 mw	----	1366 s	----	----	1367 (1, 1)	1359 (2, 0.5)	0.57	
	13	CH ₂ wag	1340 mw	1340 (3) P	----	1339 (2)	----	1350 (4, 2)	1349 (1, 2)	0.32	
	14	CH ₂ wag	1324 ms	1322 (2) P	1320 m	1321 (1)	----	1289 (0.3, 3)	1330 (2, 1)	0.50	
	15	=C-H in-plane wag*	1211 s	1210 (39) P	1217 s	1207 (32)	----	1245 (20, 10)	1217 (6, 13)	0.44	
	16	Ring stretch*	1122 s	1123 (2) D	1119 s	1121 (1)	----	1161 (7, 2)	1120 (8, 1)	0.61	
	17	Ring stretch	1048 w	1048 (5) D	----	1046 (1)	----	1093 (1, 2)	1045 (0.2, 2)	0.75	
	18	Ring stretch*	977 m	975 (6) D	978 w	970 (2)	----	955 (5, 1)	974 (1, 10)	0.72	
	19	Ring angle bend*	939 s	939 (3) D	939 s	----	----	891 (1, 0.1)	931 (3, 1)	0.63	
	20	Ring stretch	858 w	857 (20) P	856 w	853 (34)	----	833 (1, 2)	847 (1, 3)	0.16	
	21	Ring stretch	764 s	763 (26) P	761 s	757 (27)	----	712 (1, 6)	755 (4, 3)	0.15	
	22	C=O in-plane wag*	488 ms	488 (4) D	485 m	485 (4)	----	528 (0.1, 2)	480 (2, 1)	0.67	
	23	Ring angle bend*	464 mw	462 (12) P	459 w	456(23)	----	470 (2, 2)	460 (1, 2)	0.42	
	24	Ring angle bend	422 m	423 (2) D	----	428 (2)	----	438 (4, 0.3)	419 (2, 0.5)	0.68	

Table 6: (Continued)^a

Sym.	v	Liquid			Vapor			Calculated ^c		
		C _s (C ₁)	C ₁	Approx. descript.	Infrared	Raman ^b	Infrared	Raman ^b	C _s (I _{IR} , I _{Ram})	C ₁ (I _{IR} , I _{Ram})
A''(A)	25	3	CH ₂ antisym. str.	----	(2955)	----	2970 (72)	2979 (9, 37)	2981 (5, 48)	0.33
	26	4	CH ₂ antisym. str.	2950 s	2955 (39) P	2952 vw	2953 (100)	2954 (0.3, 23)	2958 (11, 56)	0.44
	27	5	CH ₂ antisym. str.	2942 s	2940 sh	2942 vs	(2934)	2910 (2, 34)	2938 (11, 78)	0.25
	28	18	CH ₂ twist	1257 s	1256 (4) P	1258 w	1252 (4)	1286 (0, 2)	1254 (3, 2)	0.58
	29	19	CH ₂ twist	1240 s	1239 (2) D	1248 sh	----	1251 (0.1, 2)	1242 (6, 1)	0.67
	30	21	CH ₂ twist	1141 ms	1140 (10) P	1141 m	1140 (6)	1203 (1, 0.3)	1147 (2, 2)	0.49
	31	23	CH ₂ rock	1055 vw	1055 (9) D	----	1054 (6)	1030 (0, 1)	1058 (0.1, 2)	0.46
	32	25	=C-H oop wag	1018 vvw	1017 (0.3) D	1019 w	----	1009 (0, 1)	1003 (0.2, 1)	0.67
	33	28	CH ₂ rock	876 s	875 (1) P	875 s	875 (2)	907 (6, 0.1)	880 (5, 0.2)	0.37
	34	31	CH ₂ rock*	732 s	733 (5) P	730 s	727 (18)	753 (0.3, 0.5)	729 (5, 1)	0.17
	35	32	=C-H oop wag*	705 vw	704 (27) P	----	700 (49)	709 (7, 0.5)	700 (0.3, 4)	0.07
	36	33	C=O oop wag	586 mw	585 (2) D	585 w	585 (2)	527 (1, 1)	585 (1, 1)	0.72
	37	37	C=C twist	309 m	310 (7) D	304 ^e	304 (4)	282 (0.4, 0.4)	308 (0.3, 1)	0.66
	38	38	Ring bending	250 mw	250 (5) D	247 ^e	245 (6)	<i>i</i>	241 (0.2, 1)	0.61
	39	39	Ring inversion	----	----	99 ^e	----	<i>i</i>	103 (1, 0.1)	0.74

^a s, strong; m, medium; w, weak; v, very; P, polarized; D, depolarized; sh, shoulder peak; *i*, imaginary frequency; oop, out-of-plane; ρ, calculated depolarization ratios for the C₁ point group. ^b The values in the parentheses are relative Raman intensities. ^c Calculated using B3LYP/6-311++G(d,p) level of theory, the calculated values were scaled by a factor of 0.985 for frequencies below 2000 cm⁻¹ and by 0.964 for frequencies above 2000 cm⁻¹. ^d Fermi resonance with relative intensities of 86 and 35 respectively. ^e Reference 24. * These modes are strongly coupled with each other.

Figure 13 shows the liquid Raman spectra of 2CHO (below 2000 cm^{-1} region) with parallel and perpendicular polarization compared with the liquid infrared spectra. The frequency values observed in the two complementary spectra matches very closely and the difference is not more than 1 cm^{-1} for most cases. The frequencies determined by the infrared spectrum are more accurate since they are based on the calibration with respect to the 632 nm line of the He-Ne laser of the FT instrument. The liquid-phase far-infrared spectrum was collected using a CS_2 solution of the sample. Comparison of the peaks observed using the pure compound and the solution shows that the peaks observed in the solution are slightly broadened. The listing of polarized and depolarized bands of the liquid Raman spectra in Table 6 is based on the values of the experimental depolarization ratios (ρ values). The bands which show an observed ρ value of 0.6 or higher are listed as depolarized. Since this molecule has C_1 symmetry, theoretically all of the bands should be polarized. However, some modes will be more polarized than the others. Comparison of the polarizability of these bands with the calculated ρ values of the C_1 point group shows that this classification is very reasonable as most of the Raman bands classified as depolarized have higher calculated ρ values compared to those of the polarized ones. The classification of A' and A'' symmetries is also useful as most of the vibrational modes with A'' symmetry have low Raman intensities and are depolarized. Six out of twelve bands with A'' symmetry observed by liquid Raman spectra are depolarized while only seven out of nineteen modes with A' symmetry and observed by liquid Raman are depolarized. The liquid Raman spectrum of 2CHO exhibits a doublet at 1669 and 1681 cm^{-1} . This doublet is due to the interaction of the $\text{C}=\text{O}$ stretching mode with an overtone or a combination of another vibrational mode. The origin of these bands was discussed in detail previously and it was reported that this is due to a Fermi resonance interaction between the $\text{C}=\text{O}$ stretch mode and the combination mode of the ring breathing and $\text{C}=\text{C}$ skeletal deformation (both are ring stretching modes in general) and reported the two peaks at 1669.4 and 1682.4 cm^{-1} .⁶⁴ However, this doublet is illustrated again in Figure 14 which shows the parallel and perpendicular Raman polarization measurements which were not done in the original study.

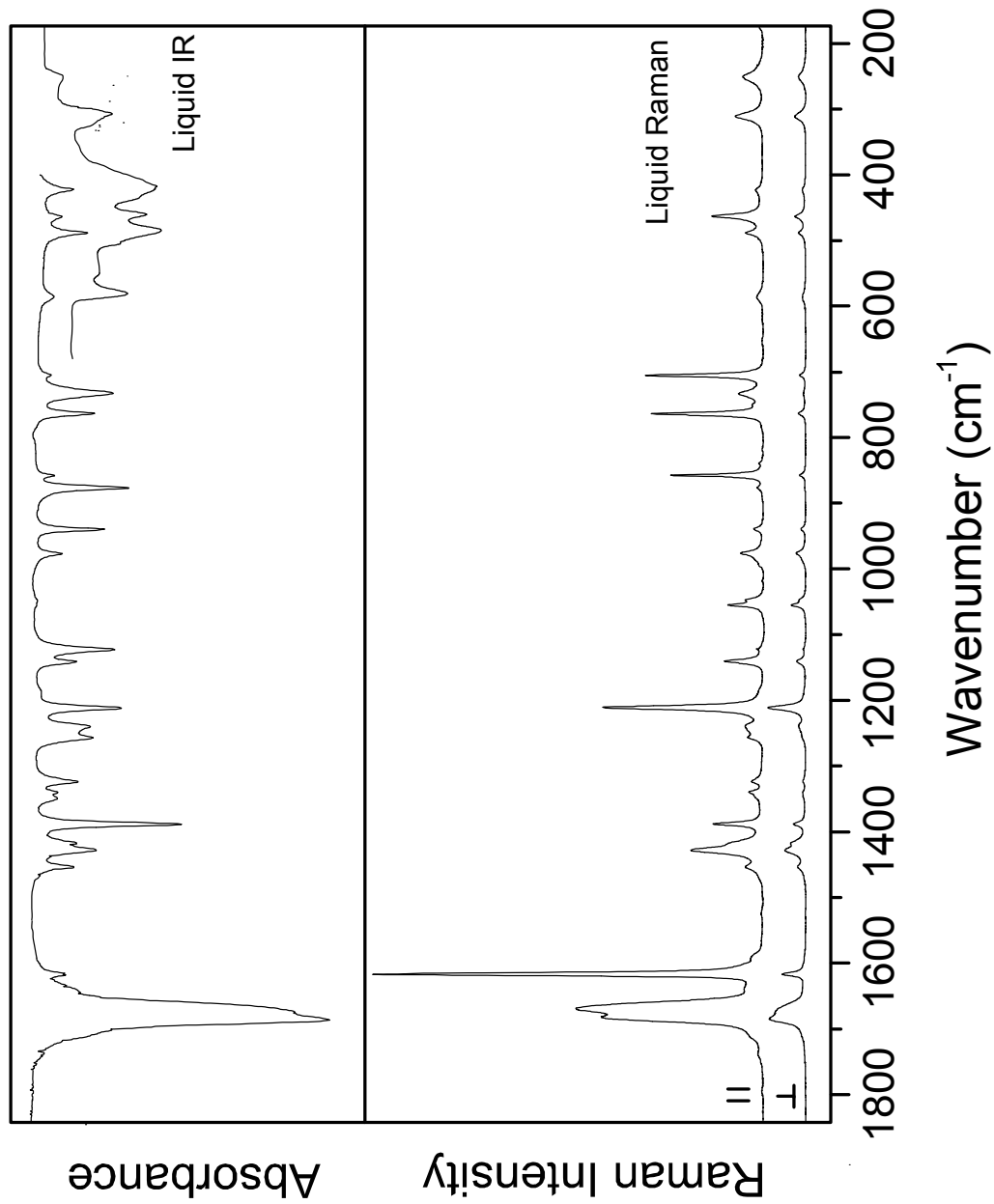


Figure 13. Liquid-phase infrared and Raman (with parallel and perpendicular polarization) spectra of 2CHO.

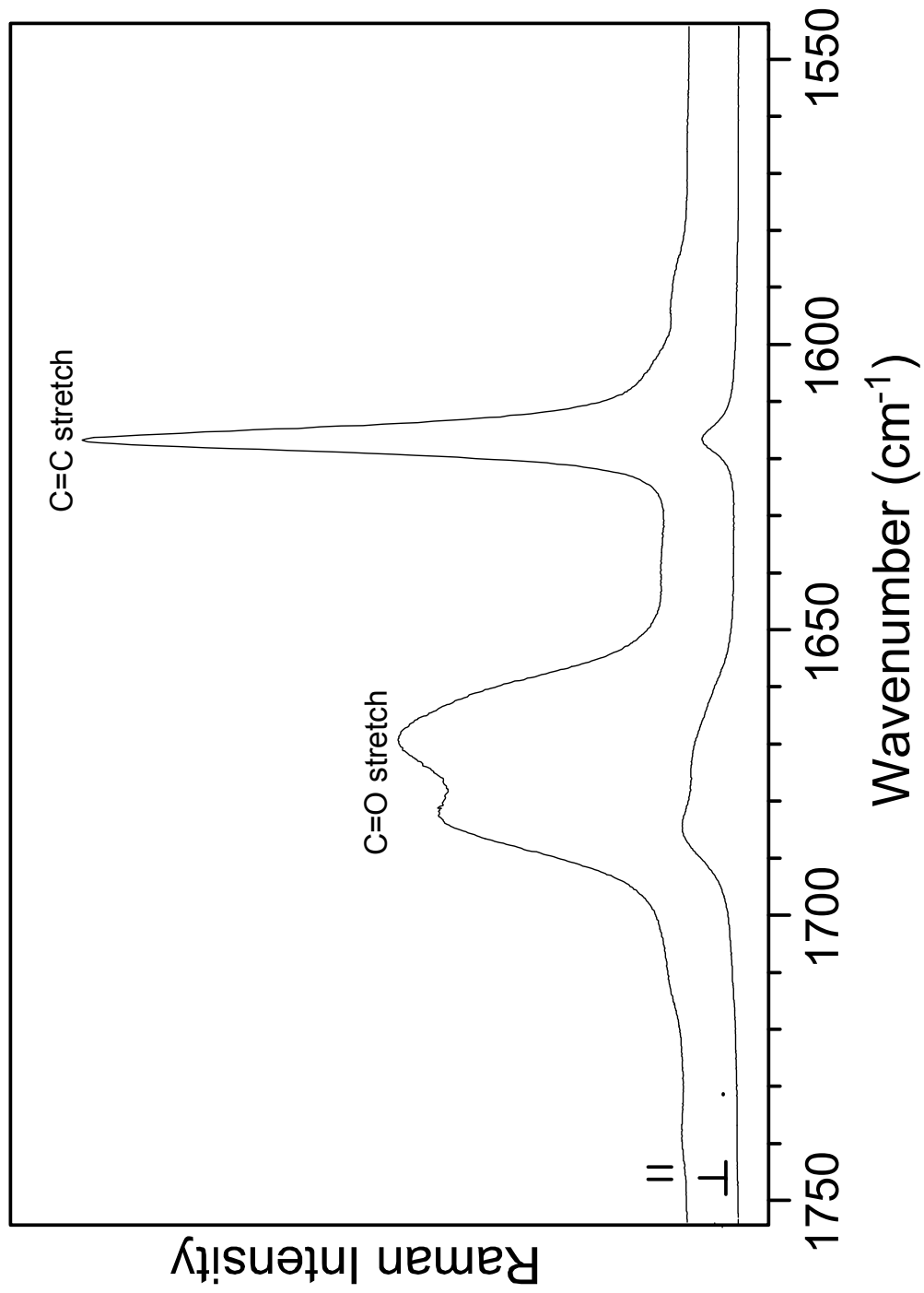


Figure 14. Fermi interaction of C=O stretching mode of 2CHO.

The low-frequency peak is more intense with parallel polarization, but becomes weaker than the higher frequency band when measured with perpendicular polarization indicating that it has a lower depolarization ratio. The C=O stretching frequency observed in the vapor-phase IR spectrum is 1712 cm^{-1} which is significantly higher than that observed in the liquid-phase spectrum which is at 1686 cm^{-1} . 2CHO molecules in the liquid have intermolecular dipole interactions due to the polar carbonyl group. This interaction is shown in Figure 15 and this causes a red shift in the C=O stretching vibration and results in a broader peak. These intermolecular forces are mostly absent in the vapor phase because the molecules are far apart. Therefore, the vapor-phase spectra show spectra for independent, non interacting molecules which are also those calculated by DFT method. Another interesting feature seen in the C=O stretching of 2CHO is its frequency significantly lower than that 2CPO which is at 1748 cm^{-1} .²⁰ This is a very common feature seen in cyclic ketones where the C=O stretching frequency decreases as the size of the ring increases.

Figures 16 and 17 compare the liquid-phase Infrared and Raman spectra of 2CHO- d_3 with the calculated spectra. Both IR and Raman spectra show at least three strong C-D stretching vibrations in the $2000\text{-}2300\text{ cm}^{-1}$ region. The vibrational assignments made in Table 7 were carried out by taking the experimental frequencies and their intensities which closely match with the calculated values. The normal modes were again determined by visualization of the atomic motions of the calculated Gaussian 03 output files using GaussView 3.0 molecular modeling program.⁶³ The frequencies of the two strongest peaks observed in the liquid Raman spectra, the C=C and C=O stretching frequencies at 1604 and 1666 cm^{-1} respectively, are lower than those of the undeuterated compound. Also unlike 2CHO, no Fermi resonance is observed in the C=O stretching vibration. A peak observed at 1617 cm^{-1} may be due to the C=C stretching of the undeuterated compound whose value was seen at 1616 cm^{-1} in the Raman spectrum of the pure 2CHO- d_0 . This indicates that some undeuterated compound also remains in

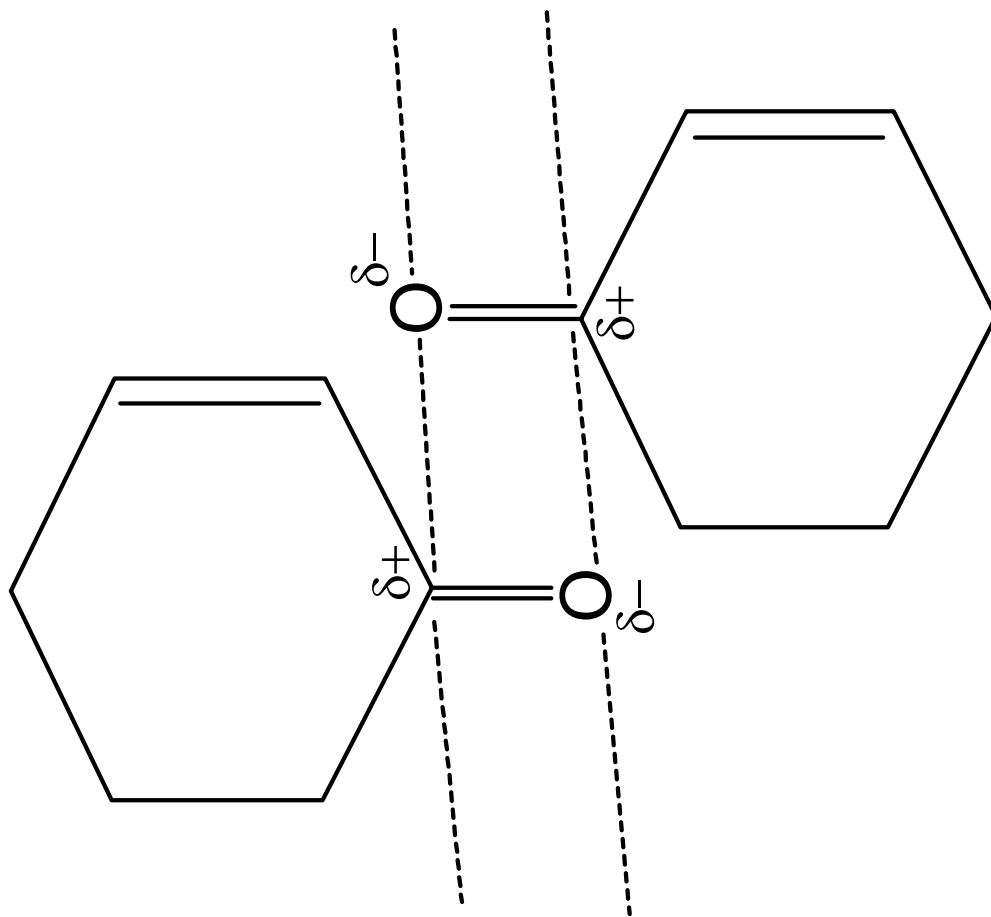


Figure 15. Intermolecular interactions of 2CHO molecules in the liquid-phase due to the polar carbonyl group.

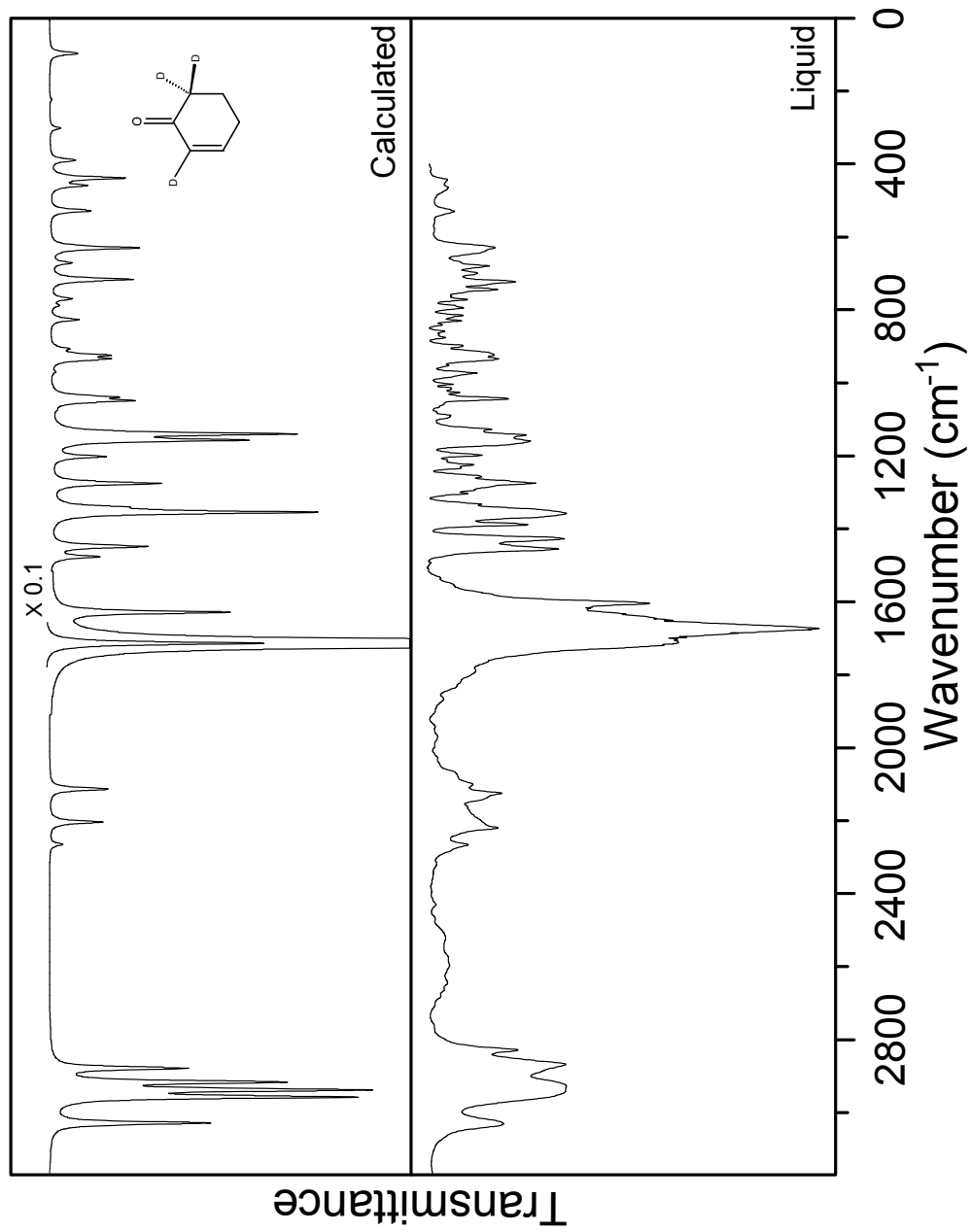


Figure 16. Calculated and liquid infrared spectra of 2CHO-d₃.

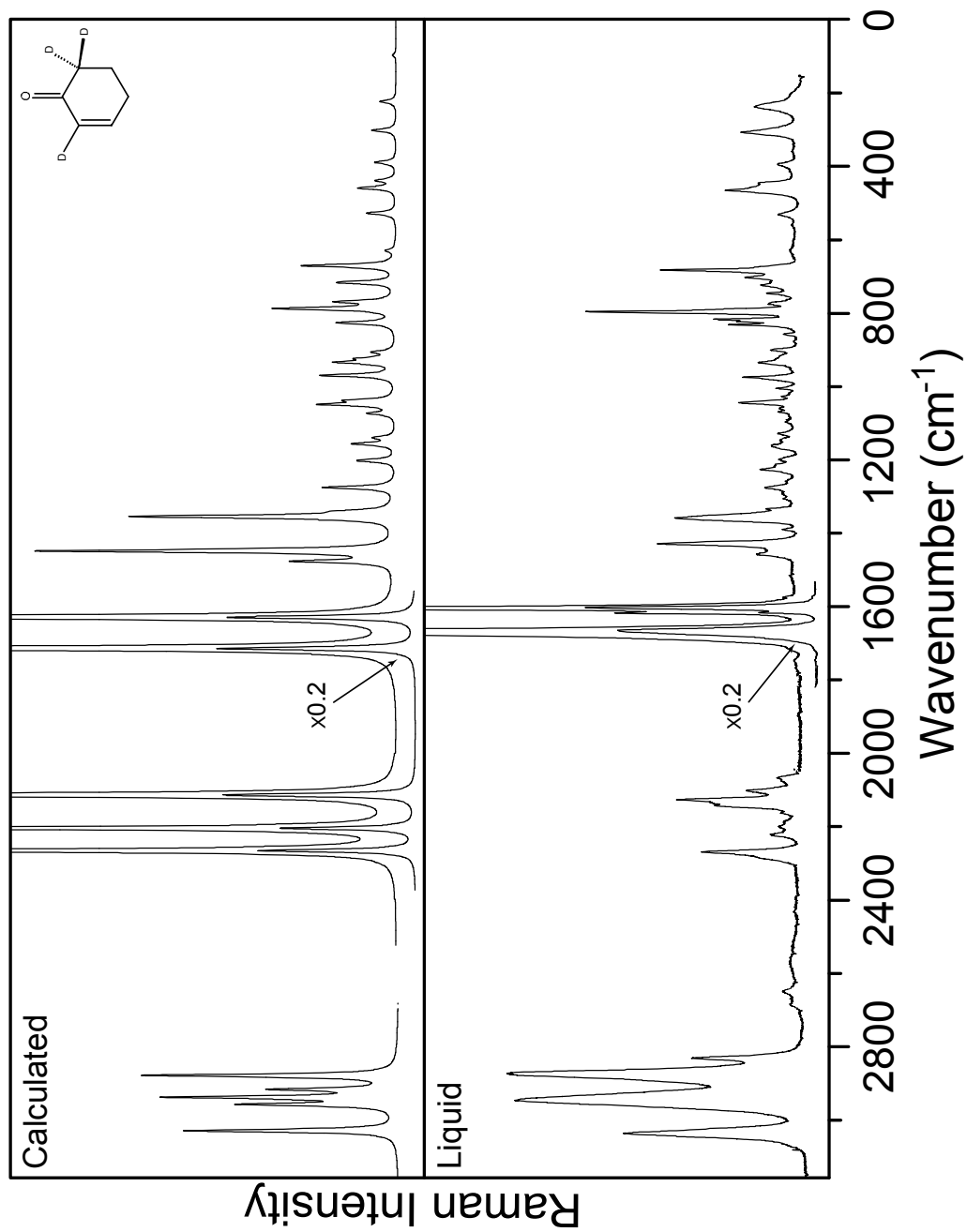


Figure 17. Calculated and liquid Raman spectra of 2CHO-d₃.

Table 7: Vibrational assignment (in cm^{-1}) of 2-cyclohexen-1-one- d_3 ^a

Symmetry $C_s(C_1)$	v		Approx. description	Liquid		Calculated ^c		
	C_s	C_1		IR	Raman ^b	$C_s(I_{IR}, I_{Raman})$	$C_1(I_{IR}, I_{Raman})$	ρ
A' (A)	1	1	=C-H stretch	3032 ms	3036 (25) P	3020 (6, 86)	3028 (6, 84)	0.25
	2	3	CH ₂ symm. Str. (C-5)	---	2945 (38) P	2943 (12, 87)	2938 (11, 88)	0.23
	3	5	CH ₂ symm. Str. (C-4)	2869 s	2873 (40) P	2899 (7, 100)	2878 (5, 100)	0.17
	4	6	=C-D stretch	2266 mw	2269 (14) P	2265 (0.4, 27)	2265 (0.5, 28)	0.36
	5	8	CD ₂ symm. Str.	2125 ms	2126 (13)P	2137 (2, 34)	2113 (2, 34)	0.10
	6	9	C=O stretch	1673 vvs	1666 (87) P	1701 (100, 41)	1714 (100, 35)	0.38
	7	10	C=C stretch	1603 s	1604 (100) P	1646 (8, 38)	1628 (6, 33)	0.10
	8	11	CH ₂ deform (C-5)	1455 s	1457 (5) D	1490 (2, 4)	1477 (2, 3)	0.70
	9	12	CH ₂ deform (C-4)	1427 vs	1428 (17) P	1447 (4, 16)	1448 (4, 13)	0.50
	10	13	=C-H in-plane wag	1388 s	1389 (2) P	1369 (11, 9)	1357 (2, 3)	0.56
	11	14	CH ₂ wag (C-4, 5)	1358 s	1358 (16) P	1364 (2, 3)	1354 (9, 8)	0.37
	12	15	CH ₂ wag (C-4, 5)	1332 vw	1333 (3) P	1337 (3, 4)	1340 (2, 1)	0.49
	13	18	Ring stretch	1160 vs	1161 (3) P	1185 (18, 2)	1157 (7, 2)	0.45
	14	19	Ring stretch	1143 vw	1147 (1) D	1152 (2, 1)	1140 (9, 1)	0.75
	15	20	Ring stretch + CD ₂ wag	1065 vvw	1068 (1) P	1071 (5, 1)	1073 (0.1, 1)	0.32
	16	21	CD ₂ deform	1043 s	1044 (7) D	1053 (2, 2)	1049 (3, 3)	0.74
	17	23	Ring stretch	973 ms	974 (7) D	972 (1, 5)	970 (0.1, 3)	0.67
	18	26	Ring angle bend	898 vw	900 (3) D	881 (2, 1)	906 (0.5, 1)	0.50
	19	27	=C-D in-plane wag	830 w	831 (7) P	830 (1, 0.4)	827 (1, 2)	0.07
	20	29	Ring stretch + CD ₂ wag	771 w	774 (2) P	767 (1, 7)	769 (1, 2))	0.09
	21	31	Ring stretch	680 m	681 (17) P	682 (1, 5)	671 (1, 3)	0.08
	22	33	Ring angle bend	529 ms	531 (2) P	521 (0.1, 2)	528 (2, 1)	0.63
	23	34	Ring angle bend	464 m	465 (9) P	462 (1, 2)	459 (1, 1)	0.43
	24	36	C=O in-plane wag	----	394 (2) D	423 (4, 0.2)	390 (1, 1)	0.73

Table 7: (Continued)^a

Symmetry	ν	Liquid			Calculated				
		$C_s(C_1)$	C_s	C_1	Infrared	Raman	$C_s(I_{IR}, I_{Raman})$	$C_1(I_{IR}, I_{Raman})$	ρ
A'' (A)	25	2	CH ₂ antisymm. Str. (C-5)	2936 s	----	----	2970 (8, 42)	2957 (11, 58)	0.53
	26	4	CH ₂ antisymm. Str. (C-4)	----	----	----	2910 (2, 46)	2916 (8, 45)	0.26
	27	7	CD ₂ antisymm. Str.	----	2142 (9) P	----	2194 (1, 17)	2204 (2, 24)	0.57
	28	16	CH ₂ twist (C-4,5)	1275 vs	1275 (3) D	----	1279 (0.1, 4)	1275 (4, 3)	0.73
	29	17	CH ₂ twist (C-4,5)	1198 ms	1199 (2) P	----	1227 (0.3, 1)	1202 (2, 1)	0.59
	30	22	CH ₂ rock (C-4,5)	1026 vw	1027 (1) D	----	1032 (1, 2)	1038 (2, 1)	0.64
	31	24	=C-H out-of-plane wag	935 s	935 (4) D	----	947 (2, 1)	934 (2, 2)	0.74
	32	25	CD ₂ twist	923 s	----	----	931 (1, 0)	924 (2, 1)	0.70
	33	28	=C-D out-of-plane wag	794 w	796 (26) P	----	809 (0.4, 0.2)	788 (0.3, 4)	0.08
	34	30	CH ₂ rock (C-4,5)	722 m	723 (3) D	----	705 (3, 1)	716 (3, 2)	0.61
	35	32	CD ₂ rock	629 ms	631 (1) P	----	605 (4, 0.3)	630 (3, 0.3)	0.74
	36	35	C=O out-of-plane wag	444 m	446 (5) P	----	451 (1, 1)	439 (3, 1)	0.51
	37	37	C=C twist	----	307 (7) D	----	275 (1, 1)	302 (0.4, 1)	0.64
	38	38	Ring inversion	----	236 (5) D	----	<i>i</i>	224 (0.1, 1)	0.63
	39	39	Ring bend	----	----	----	<i>i</i>	97 (1, 0.1)	0.74

^a See Table 6 for footnotes.

the sample. The infrared spectrum is more congested than that of the Raman and there are more peaks which cannot be explained using the calculated values. Since the deuterium atoms of the $2\text{CHO-}d_3$ can be exchanged with the hydrogen atoms of H_2O in moist ambient air, the sample may become contaminated by the formation of other isotopic species during the acquisition of the infrared spectra. This can be clearly seen by the careful analysis of the strongest infrared band, C=O stretching, which is much broader than that of 2CHO . The most probable reason to this is the presence of several bands of close frequencies overlapped on each other. Nevertheless, the observance of the intense C=C stretching band of $2\text{CHO-}d_3$ at 1603 cm^{-1} (1604 cm^{-1} in the Raman spectra) suggests that the sample is rich in $2\text{CHO-}d_3$. Furthermore, most of the anticipated bands predicted by the calculations are observed in both spectra and very good agreement can be seen between the experimental values and the calculated frequencies for the C_1 point group.

Figure 18 illustrates the liquid Raman spectra of $2\text{CHO-}d_3$ with parallel and perpendicular polarization compared with the liquid infrared spectra. Again very good agreement can be seen between the wavenumbers observed in the two spectra and the difference is only 1 or 2 cm^{-1} in most cases. The calculated and the experimental depolarization ratios also agree very well and most of the normal modes classified as A'' are depolarized.

CONCLUSIONS

The computed frequencies and intensities for the C_1 structure of 2CHO and $2\text{CHO-}d_3$ using the B3LYP/6-311++G(d,p) level of theory agree remarkably with the experimentally determined values. These computations are extremely useful in assigning the vibrational modes of these types of molecules. The calculated C_s (planar structure) frequencies differ substantially as this structure imposes a constraint on the molecule. The spectra of $2\text{CHO-}d_3$ have been affected to some extent by the presence of isotopic impurities and further studies, especially the analysis of the vapor phase, may be of value in the future.

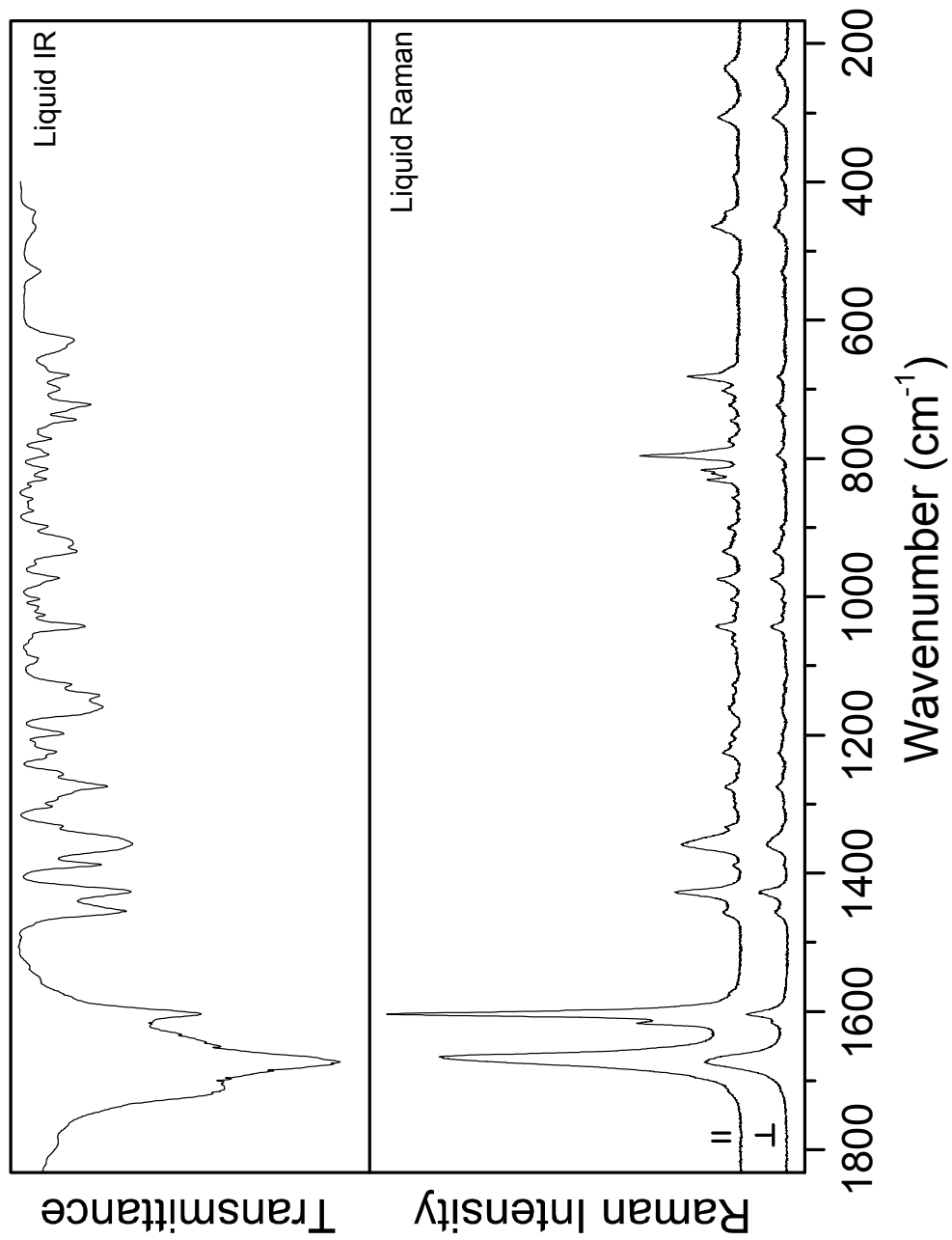


Figure 18. Liquid Raman spectra of 2CHO-d_3 with parallel and perpendicular polarization compared with liquid IR spectra.

CHAPTER VI

ULTRAVIOLET CAVITY RINGDOWN SPECTRA OF 2-CYCLOHEXEN-1-ONE AND ITS POTENTIAL ENERGY FUNCTION FOR THE ELECTRONIC GROUND STATE

INTRODUCTION

This chapter and the next will present a detailed study of the ultraviolet cavity ringdown spectra (CRDS) of the compounds of 2-cyclohexen-1-one (2CHO) and its 2,6,6-*d*₃ isotopomer (2CHO-*d*₃). The experimental work of this was done at the laboratory of Dr. Stephen Drucker at University of Wisconsin at Eau Claire. The spectroscopic data obtained from this analysis was used to determine the vibrational energy levels and the ring-inversion potential energy functions of these two compounds in their ground and S₁(n,π^{*}) electronic states. The study presented in this chapter will discuss the one-dimensional ring-inversion potential energy function of 2CHO for its ground electronic state determined by CRDS along with vapor-phase Raman spectra. Although low-frequency Raman²³ and far-infrared²⁴ studies have been previously utilized for this purpose, the outcomes of these two analyses are completely different from each other. Also because of the use of reduced (dimensionless) potential energy function, the structure corresponding to the energy minimum is not determined. Here, a kinetic energy expansion has been used to model the inversion process to find the equilibrium structure. The results obtained are compared with those given by density functional theory (DFT) calculations.

EXPERIMENTAL AND COMPUTATIONAL

The cavity ringdown spectra of 2CHO were recorded using a CRD spectroscopy system that has been described elsewhere in detail.²¹ Briefly, the output of a Nd:YAG-pumped pulsed dye laser (approximately 0.5 mJ at 385 nm) was sent through a spatial filter and then into a 1-m CRD cell. The cell was bounded by high-reflectivity mirrors

(Los Gatos Research, quoted $R = 0.99994$ at 385 nm) with 6-m radii of curvature. The light exiting the cell was detected by a photomultiplier module (Hamamatsu H6780). The photomultiplier signal was sent into the 50-ohm input of a digital oscilloscope (10-bit vertical resolution) and through a 20-MHz internal low-pass filter. The decay traces from typically 16 laser pulses were averaged and then sent to a computer, where a monoexponential rate constant k (along with baseline offset) was determined. The vapor-phase Raman spectra were recorded on a JY U-1000 instrument equipped with a photomultiplier tube using a Coherent I-20 argon ion laser operating at 514.5 nm with 5 W of laser power. DFT calculations were carried out by Dr. Jaebum Choo of Hanyang University, Korea utilizing the same programs and methods previously described for 2CPO.^{21,65}

RESULTS AND DISCUSSION

Cavity ringdown (CRD) spectra

Figure 19 illustrates the CRD spectrum of 2CHO in the 400 to -400 cm^{-1} region relative to the 0_0^0 band which is at 26089.1 cm^{-1} . A broader range of frequencies was examined but this chapter primarily focuses only on this region. This spectrum illustrates the inversion transitions in both the ground state and in the $S_1(n,\pi^*)$ state. Figure 20 shows an expanded form of the difference band region from 0 to -400 cm^{-1} which points up the frequencies of the ring inversion vibration in the ground state. Table 8 shows some of the selected assignments for the CRD spectrum including the ones which are relevant for understanding the S_0 electronic ground state. Most importantly the ν_{39} inversion band ($\nu_1 = 0 \rightarrow 2$ and $1 \rightarrow 3$) can be observed at -99.0 cm^{-1} . (The labeling scheme for inversion levels is indicated in Figure 21). The next band in the series corresponding to $0 \rightarrow 4$ and $1 \rightarrow 5$ occurs at -197.0 cm^{-1} , thus showing the next spacing (3-4) to be 98.0 cm^{-1} . There is also a weak band at -294.9 cm^{-1} which seems to indicate that the 5-6 spacing is 97.9 cm^{-1} . A weak band also is present at -391.6 cm^{-1} indicating another possible spacing of 96.7 cm^{-1} . The reported far-infrared spectrum²⁴ has bands listed at 99.85, 99.23, 98.63, 98.02, 97.48, and 96.87 cm^{-1} . Since these were recorded at

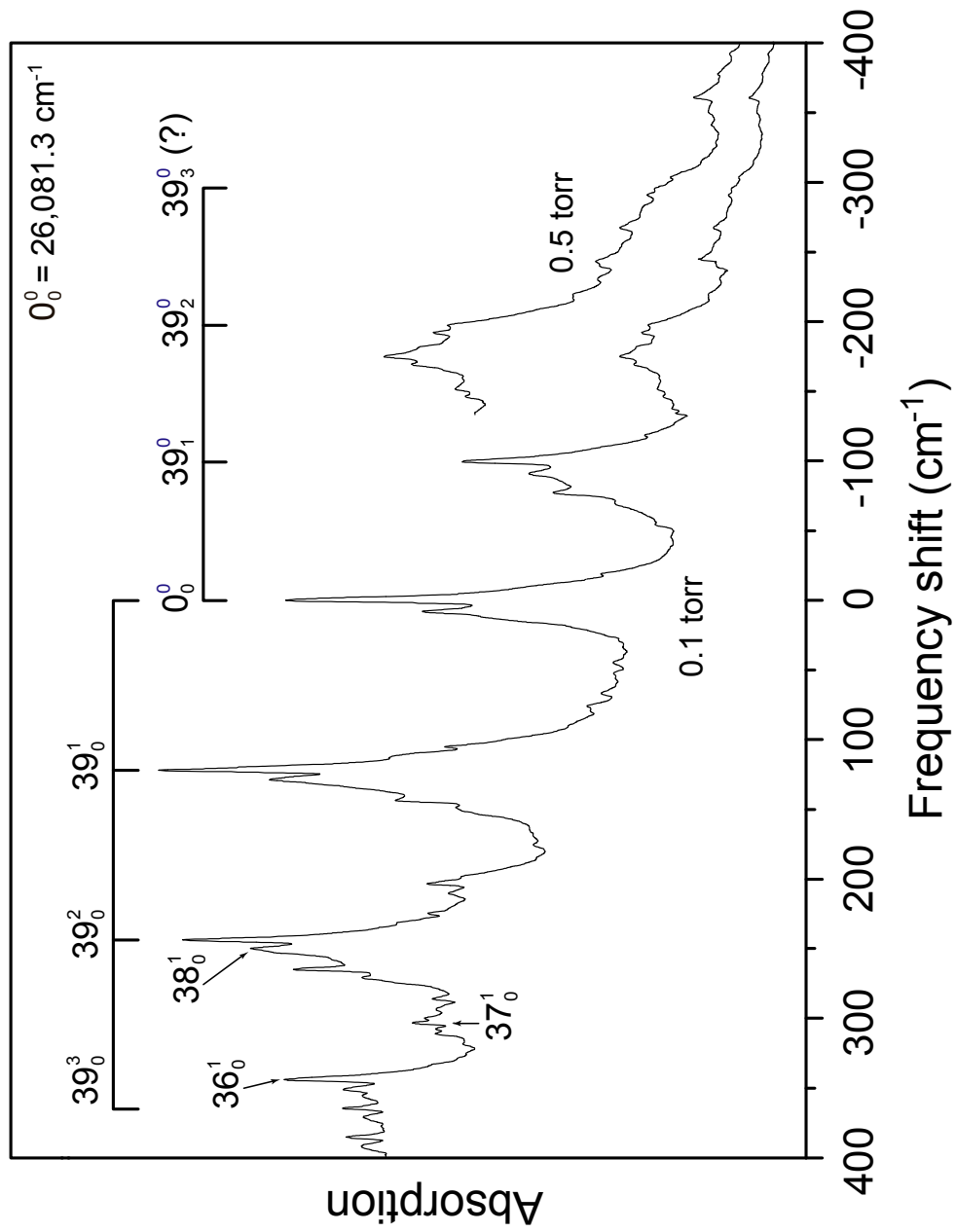


Figure 19. Cavity ringdown spectra of 2CHO relative to the S_1 0^0_0 band at 26089.1 cm^{-1} in the -400 to 400 cm^{-1} region.

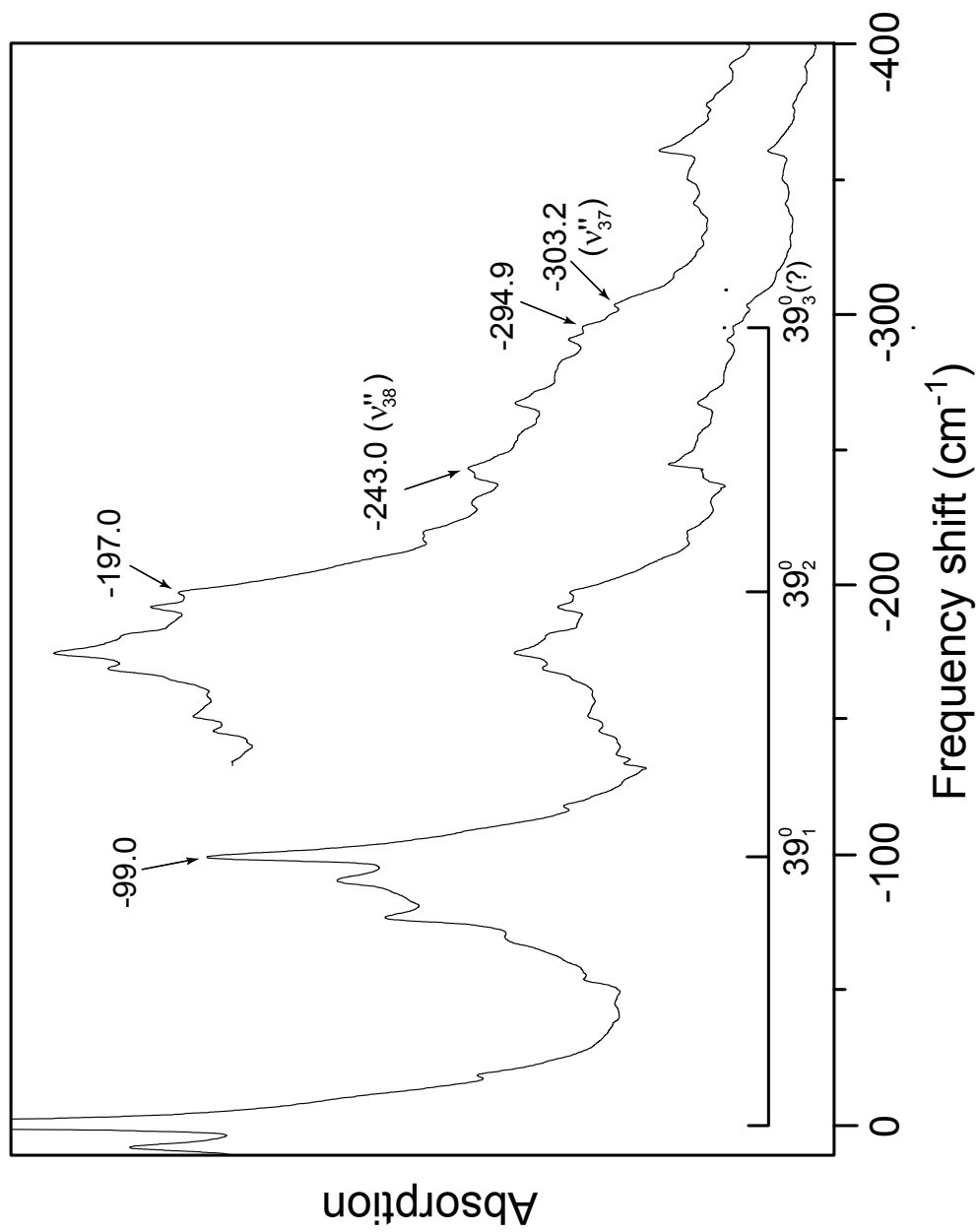


Figure 20. Cavity ringdown spectra of 2CHO relative to the $S_1(n,\pi^*) 0_0^0$ band at 26089.1 cm⁻¹ in the difference band region.

Table 8: Selected assignments for the CRD spectrum (in cm^{-1}) of 2CHO

Observed	Calculated ^a	Inferred	Assignment	
-99.0	-103	-99.2 ^b	39_1^0	
-197.0	-----	-197.2 ^b	39_2^0	
-294.9	-----	-294.1 ^b	39_3^0 (?)	
-243.0	-241	-244 ^c	38_1^0	
-303.2	-308	-304.1 ^b	37_1^0	
122.2	121	-----	39_0^1	
244.0	-----	-----	39_0^2	
364.8	-----	-----	39_0^3	
250.1	250	-----	38_0^1	
303.5	298	-----	37_0^1	
344.1	342	-----	36_0^1	
-76.6	-----	-74.8	39_2^1	122.2-197.0
44.9	-----	47.0	39_2^2	244.0-197.0
52.7	-----	53.1	$38_0^1 39_2^0$	250.1-197.0
143.7	-----	145.0	39_1^2	244.0-99.0
150.3	-----	151.1	$38_0^1 39_1^0$	250.1-99.0
168.8	-----	167.8	39_2^3	364.8-197.0
203.8	-----	204.5	$37_0^1 39_1^0$	303.5-99.0
244.0	-----	245.1	$36_0^1 39_1^0$	344.1-99.0
265.1	-----	265.8	39_1^3	364.8-99.0
271.1	-----	272.0	$38_0^1 39_1^1$	371.0-99.0
370.9	-----	372.3	$38_0^1 39_0^1$	250.1+122.2

^a Calculated using B3LYP/6-311+G(d,p) level of theory. ^b Inferred from far-infrared data (Ref. 24). ^c From the Raman spectrum.

0.5 cm^{-1} resolution and the spectral points were probably calculated for each 0.25 cm^{-1} , the accuracy of these numbers can be taken to be $\pm 0.3 \text{ cm}^{-1}$. It is not clear why they were reported to two decimal place accuracy. In any case, since ν_{38} occurs at 243 cm^{-1} and since its excited vibrational state will be 30% as populated as the ground state at room temperature, a second superimposed series of ν_{39} bands can be expected in this region. The two strongest far-infrared peaks occur at 99.2 and 98.0 cm^{-1} so it seems apparent that these correspond to the first two spacings of 99.0 and 98.0 cm^{-1} obtained from the CRD spectra. The 99.8 and 98.6 cm^{-1} bands then arise within the ν_{38} excited state and not from the principal series as previously assumed. Moreover, the close spacing assumed by Smithson and Wieser²⁴ led them to calculate an unreasonably high barrier to inversion of 3379 cm^{-1} (9.65 kcal/mole). The remaining question then is whether the weak -294.9 and -391.6 bands in the CRD spectra arise from the ν_{39} or from some other combinations. With the 39 vibrations of 2CHO there are many possibilities for combinations when various excited states are considered. If the -294.9 cm^{-1} CRD band is part of the ν_{39} series, then the 97.9 cm^{-1} spacing probably results from a small perturbation since a value near 97 cm^{-1} is expected. Similarly the 96.7 cm^{-1} inferred from the CRD spectrum for the following spacing seems to be almost one cm^{-1} too high. The presence of both spacings, however, would not conflict with the far-infrared spectrum as the 98.0 and 97.9 cm^{-1} bands would be superimposed, and the 96.7 cm^{-1} CRD spacing would correspond to the 96.9 cm^{-1} far-infrared band. Nonetheless, the band at 96.9 cm^{-1} in the far-infrared spectrum is assigned as the third spacing, and the two CRD bands in question were ascribed to other combinations. The energy levels and transitions in Figure 21 for ν_{39} , ν_{38} , and ν_{37} , which are based on a combination of the CRD and far-infrared spectra, were utilized for the computation of the potential energy function. The -243.0 cm^{-1} band for ν_{38} can be seen in the CRD spectrum and was observed as a far-infrared band of type B with a band center at 247 cm^{-1} .²⁴ In the excited state of ν_{38} the ring inversion (ν_{39}) bands can be seen in the far-infrared at 99.8, 98.6, and 97.5 cm^{-1} , and as expected, on the whole are somewhat weaker than the bands assigned as the principal

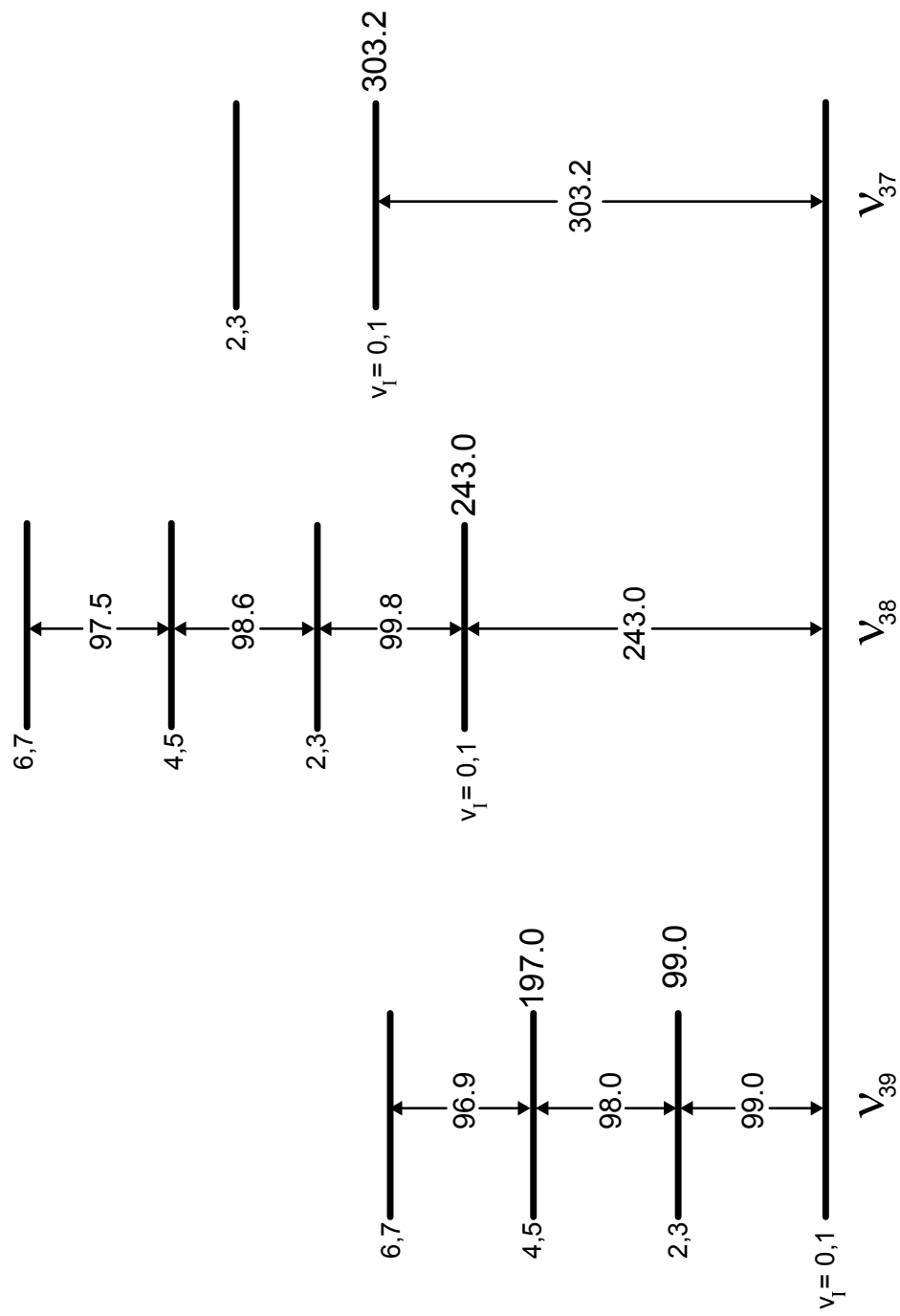


Figure 21. Vibrational energy levels for the ground state of 2CHO for v_{39} , v_{38} , and v_{37} . The v_{39} levels are doubly degenerate. v_1 represents the v_{39} quantum number.

series without ν_{38} excitation. For ν_{37} , the CRD spectra show this level to be at 303.2 cm^{-1} as compared to 304.1 cm^{-1} in the far infrared.

An important comment should be made about the band maxima listed in Table 8. The maxima themselves should be accurate to $\pm 0.1\text{ cm}^{-1}$. However, the maxima will not exactly correspond to the pure vibrational transitions, namely from $J = 0$ to $J = 0$ in the rotational quantum number. For the $S_1(n,\pi^*)$ state several of the bond distances, notably for the C=O and C=C bonds, will be longer than for S_0 . Hence, the moments of inertia will be larger for the S_1 state and the rotational constants will be smaller. This means that the rotationless Q branches actually will be on the high frequency extreme of each observed band in the spectrum. It also means that the combination bands listed in Table 8 cannot be expected to add up to yield the exact ground-state intervals since the band maxima are reported there. To a lesser extent, the rotational constants for the vibrational excited states of the inversion will, on the whole, also be smaller than for the $\nu_1=0,1$ state.

Raman spectra

The low-frequency Raman spectrum of 2CHO vapor is shown in Figure 22. This is similar to that was reported previously²³ except that the increased vapor pressure resulting from heating the sample to near its boiling point in a sealed cell results in high vapor pressure (0.6 atm) and a better signal to noise ratio. The band maximum for ν_{38} in the Raman spectrum is at 244 cm^{-1} and broad bands with maxima at 233 and 188 cm^{-1} can also be seen. Bands at 248 , 230 , 212 , 165 , and 145 cm^{-1} were previously reported,²³ but the last three bands are more likely to be noise in the spectrum. A broad feature centered at about 190 cm^{-1} was also observed and this corresponds to 188 cm^{-1} in the Raman spectrum reported here. The origins of the bands at 233 and 188 cm^{-1} seen in this spectrum are clearly not from any fundamentals, and this is supported by both the DFT calculations and the CRD spectra. The 233 cm^{-1} band could result from the $1\rightarrow 2$ transition of ν_{38} but a shift of more than 10 cm^{-1} from the $0\rightarrow 1$ band is larger than

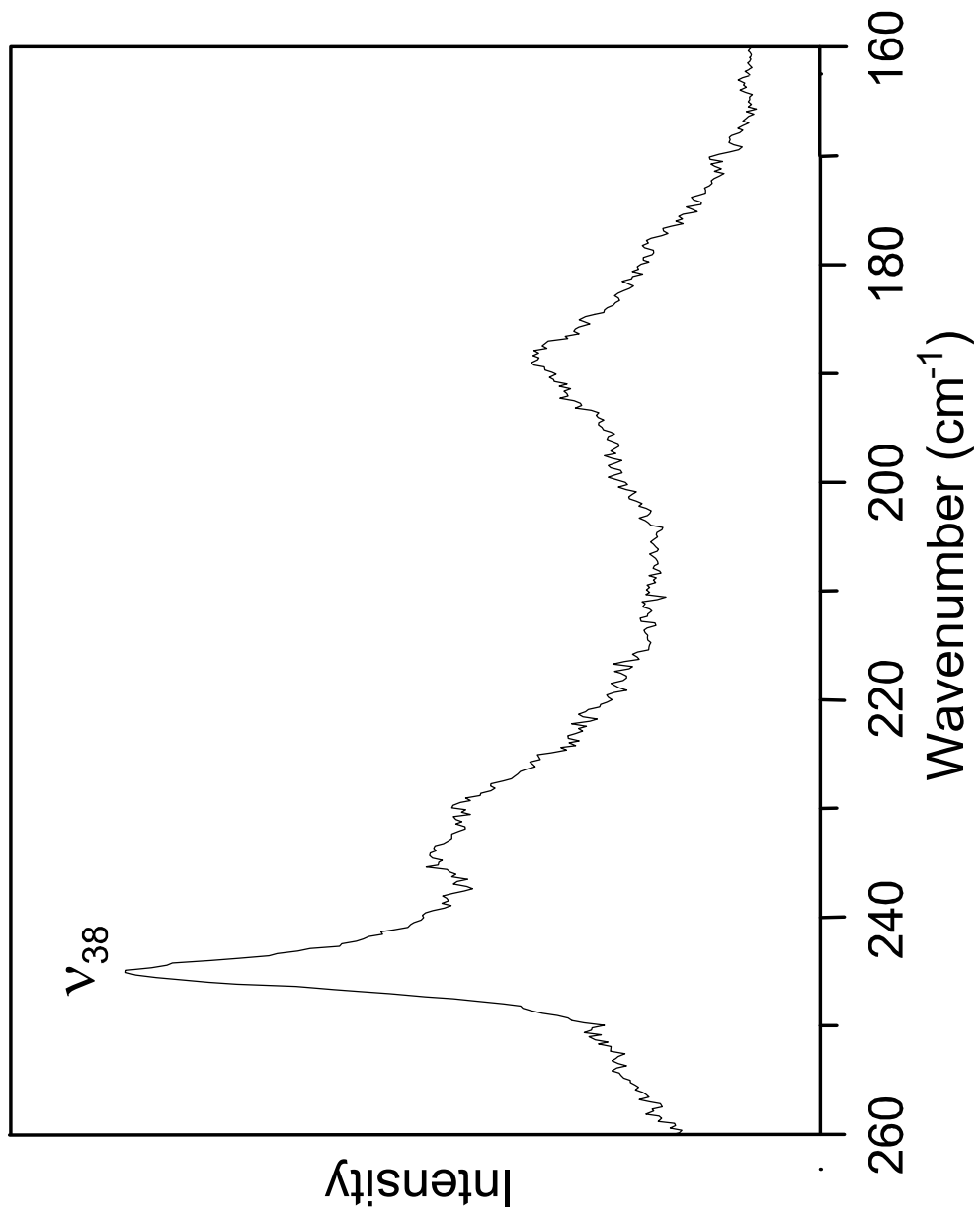


Figure 22. Raman spectra of 2CHO vapor in the low-frequency region.

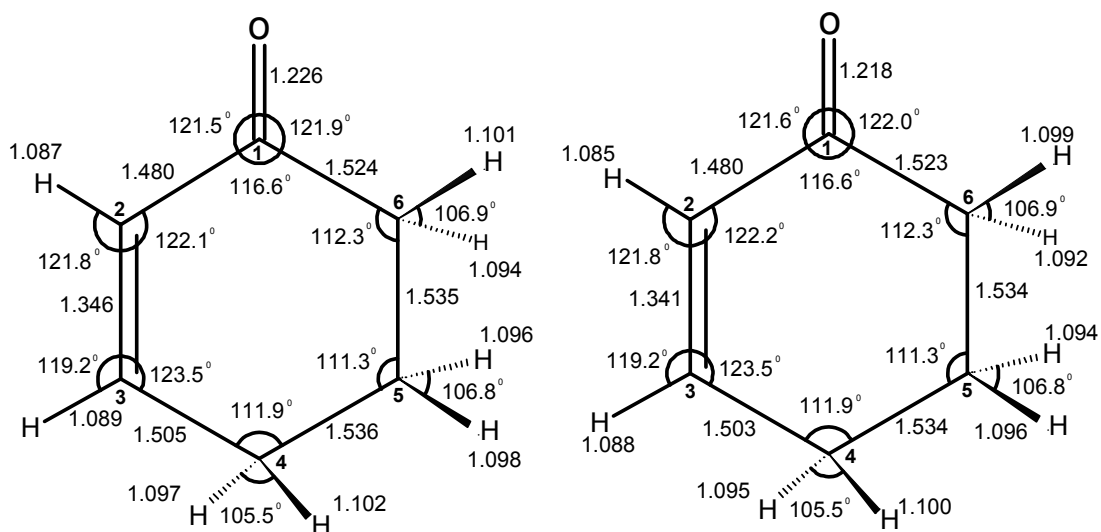
expected. Moreover, the band type appears to be broader than the 244 cm^{-1} band, and this would indicate it has a different assignment. A second possibility is that it may arise from $\nu_{36} - \nu_{39}$ difference bands (from different inversion states) which are expected near 230 cm^{-1} . For example, the $\nu_{39} (\nu_1 = 4,5) \rightarrow \nu_{36} (\nu_1 = 0,1)$ band is expected at 228 cm^{-1} . The broad 188 cm^{-1} band is somewhat too low to correspond to $2\nu_{39}$ transitions expected in the $190\text{-}197\text{ cm}^{-1}$ region for the first several ν_1 states. Similarly, it is a bit higher than expected for the $\nu_{36}\text{-}\nu_{38}$ bands which should be near 182 cm^{-1} . However, the latter may be the best explanation. No Raman bands were detected between 90 and 100 cm^{-1} corresponding to ν_{39} as the rotational envelope for the molecule is still quite strong there.

DFT calculations

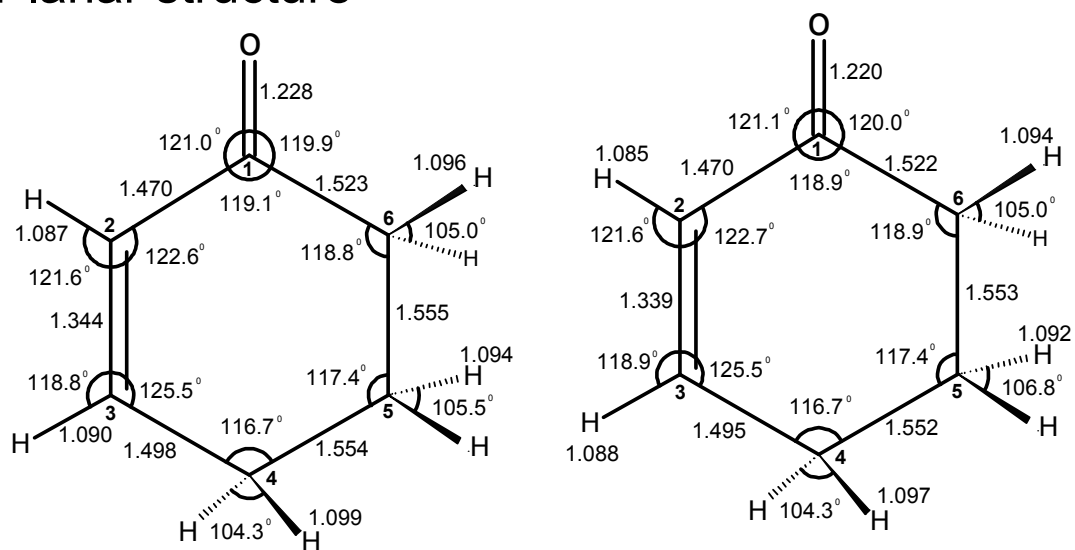
All of the DFT calculations presented here were carried out by Dr. Jaeboom Choo of Hanyang University, Korea. Several different basis sets were utilized to calculate the structure of 2CHO in its S_0 electronic ground state. Figure 23 shows the bond distances and angles calculated for the minimum energy structures and constrained planar structures using the B3LYP/6-31 + G(d,p) and B3LYP/6-311 + G(d,p) basis sets. The energy differences between the minimum energy structure and the planar structure were calculated to be 2098 and 2090 cm^{-1} , respectively. Table 9 shows the out-of-plane displacements for both calculations for the minimum energy structure for carbon atoms 1, 4, 5, and 6. The other atoms lie in the plane. Table 10 shows the rotational constants calculated for the two DFT theoretical structures and compares these to the experimental values from the microwave work.²² Also shown are the MMPI molecular mechanics results.²³ It can be seen that the two DFT calculations, and especially that with the larger basis set, provide very good agreement with the microwave experiments. Table 10 also shows the rotational constants for the $\nu_1 = 4$ quantum state of ν_{39} from the microwave study. These values have some relevance in helping to understand the band profiles better in the far-infrared and CRD spectra. The table also shows the rotational constants the hypothetical planar structure; these values are sufficiently different from the

S_0 state

Minimum energy structure



Planar structure



B3LYP/6-31+G(d,p)

B3LYP/6-311+G(d,p)

Figure 23. Calculated minimum energy and planar structures of 2CHO using B3LYP/6-31+G(d,p) and B3LYP/6-311+G(d,p) level of theories.

Table 9. Relative out-of-plane displacements of C1, C4, C5, and C6 (in Angstroms)

	B3LYP/6-31+G(d,p)	B3LYP/6-31+G(d,p)
C1	0.017166	0.017523
C4	0.133595	0.130933
C5	-0.340025	-0.339025
C6	0.267045	0.269044

Table 10. Rotational constants (in GHz) of 2-cyclohexen-1-one

	A	B	C
Experiment (MW) ^a	4.7704	2.54320	1.75829
Experiment ($\nu = 4$) ^a	4.71785	2.55709	1.77078
B3LYP/6-31+G(d,p)	4.75463	2.52258	1.74103
B3LYP/6-311+G(d,p)	4.76853	2.53297	1.74763
B3LYP/6-311+G(d,p) (planar)	4.65982	2.48608	1.66994
MMPI ^b	4.763	2.557	1.769

^a Reference 22. ^b Reference 23.

microwave ones, confirming the non-planarity of the ring. Some of the Calculated vibrational frequencies of both the ground and the S_1 states at the B3LYP/6-311+G(d,p) level of theory are listed in Table 8.

Kinetic energy functions

The extra rigidity provided by the conjugation between C=O and C=C group enables to treat the inversion process using a one-dimensional potential energy function. In that sense, the inversion is similar to that of 1,3-cyclohexadiene⁶⁶ and 1,2-dihydronaphthalene,⁶⁷ which were studied previously using Raman and fluorescence spectroscopic techniques as well as density functional (DFT) calculations.

A slightly modified version of the computer program used for 1,2-dihydronaphthalene was used to calculate the kinetic energy function of 2CHO. The vibrational model in the present work assumed that the inversion vibration labeled S follows the out-of-plane displacements according to those in Table 9. Hence, if the model is totally correct, the energy minima should correspond to an inversion coordinate value of $S = 1.0 \text{ \AA}$. The calculated function for which S is in \AA for ν_{39} is

$$g_{44}(S) = 0.03119 - 0.04782S^2 - 0.1153S^4 + 0.1490S^6 \quad (6.1)$$

The reciprocal of the first term, 32.06 in atomic units, corresponds to the reduced mass for the planar structure. The higher-order terms characterize the coordinate dependence of the function.

Ring-inversion potential energy function

As shown in Figure 21, the first three levels of the ring-inversion vibration have been determined, the first two from the cavity ringdown spectra ($\pm 0.1 \text{ cm}^{-1}$), and all three from far-infrared data ($\pm 0.3 \text{ cm}^{-1}$). These were used to determine the potential function

$$V = 7.459 \times 10^2 S^4 - 2.378 \times 10^3 S^2 \quad (6.2)$$

based on the kinetic energy function in Eq. (6.1). The function is shown in Figure 24, and it has a barrier of 1895 cm^{-1} , in very close agreement with the DFT results. Table 11 compares the observed and calculated frequencies for ν_{39} , and the agreement is excellent. However, it should be recognized that the observed levels only go up to about 340 cm^{-1} including the zero point energy, so the barrier is obtained by extrapolation. Moreover, if a value for the spectral spacing was changed even by a small amount, large changes would be observed for the barrier height. For example, if the first transition is assumed to be 99.2 cm^{-1} , the barrier drops to 1687 cm^{-1} or 14% lower. Hence, the barrier is best stated to be $1900 \pm 300 \text{ cm}^{-1}$. However, it is clearly very different from the previously reported values.^{23,24}

CONCLUSIONS

The CRD spectra of 2CHO for the $S_1(n,\pi^*) \leftarrow S_0$ transition have allowed clarifying the level spacings for the low-frequency vibrations both in the ground and in the S_1 state (Table 8). Previous Raman and far-infrared work had misinterpreted the spectra and resulted in incorrect values calculated for the inversion barrier. The research work presented in this chapter has experimentally determined the ground state inversion barrier to be $1900 \pm 300 \text{ cm}^{-1}$, with the large uncertainty arising from the need to extrapolate the potential energy function to values above the experimental data. However, this barrier value is in excellent agreement with the DFT value of 2090 cm^{-1} from the B3LYP/6-311+G(d,p) calculation. The inversion model for the vibration, which

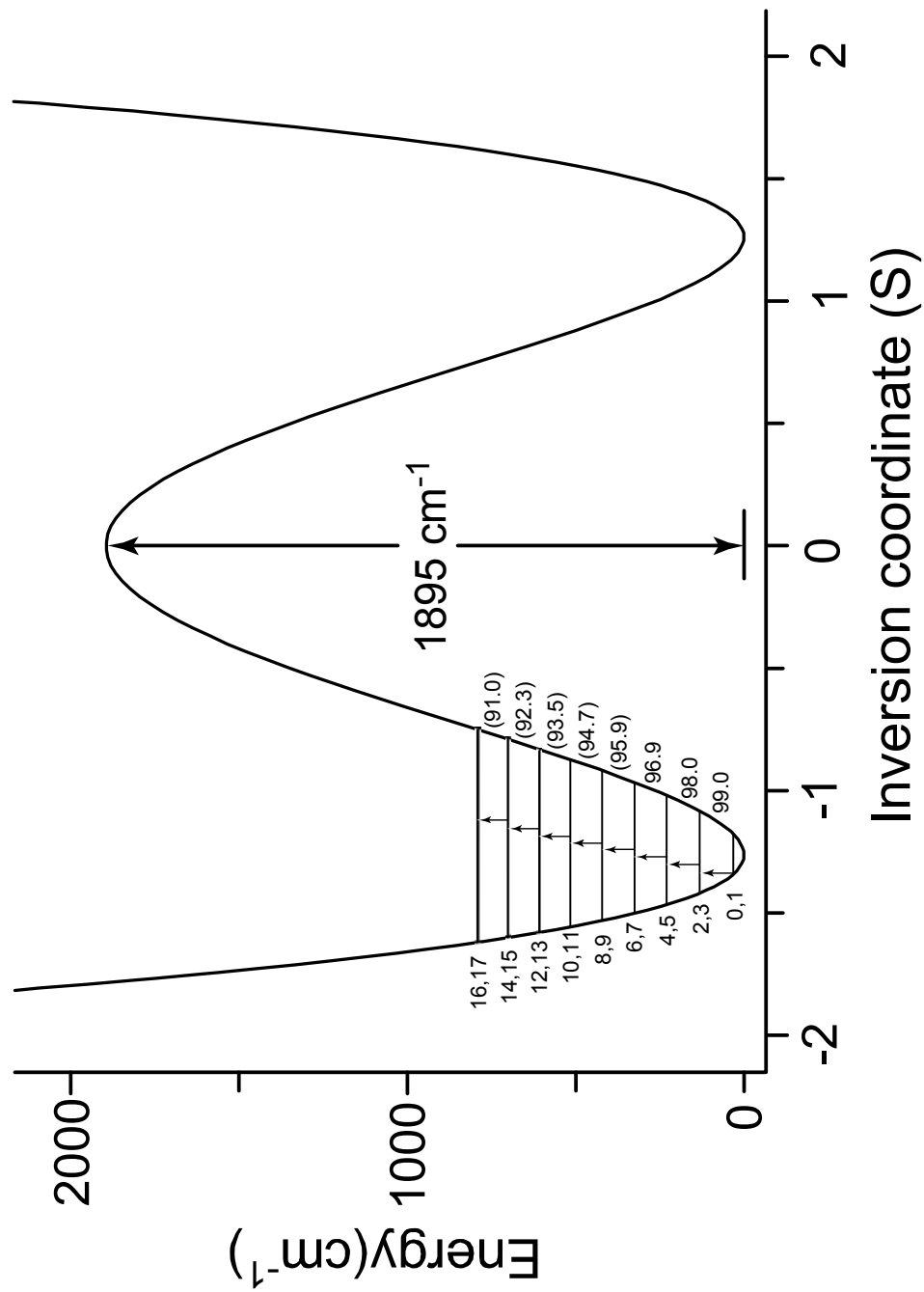


Figure 24. Ring-inversion potential energy function for 2CHO corresponding to equation 6.2.

Table 11. Observed and calculated frequencies (in cm^{-1}) for the vibration of 2-cyclohexen-1-one in its S_0 state

Separation	Frequency (cm^{-1})	
	Experimental	Calculated
0-1	-----	0.0
1-2	99.0	99.0
2-3	-----	0.0
3-4	98.0	98.0
4-5	-----	0.0
5-6	96.9 ^a	96.9
6-7	-----	0.0
7-8	-----	95.8

^a From reference 24

does not affect the barrier height, was based on the out-of-plane displacements for the minimum energy structure obtained from the DFT computations. Using the kinetic energy function for this model produces an energy minimum occurring at 1.26 Å. Since $S=1.0$ Å would indicate perfect correspondence with the DFT calculation, the minimum for this potential energy function shows the model to be quite reliable although the out-of-plane displacements of the atoms are likely to be somewhat larger than those calculated and shown in Table 9. The next chapter will present a further discussion on the CRD spectra of both 2CHO and 2CHO- d_3 which were used to determine the ring-inversion potential energy function in their electronic excited $S_1(n,\pi^*)$ state.

CHAPTER VII

ULTRAVIOLET CAVITY RINGDOWN SPECTRA AND THE $S_1(n,\pi^*)$ RING-INVERSION POTENTIAL ENERGY FUNCTION FOR 2- CYCLOHEXEN-1-ONE- d_0 AND ITS 2,6,6- d_3 ISOTOPOMER

INTRODUCTION

The photochemistry of conjugated cyclic enone molecules has been investigated from a mechanistic perspective for several decades.⁶⁸ Computational investigations in this area have been particularly active, including studies of cycloaddition reactions⁶⁹ as well as Type B,⁷⁰ lumiketone,⁷⁰ and Type C⁷¹ rearrangements. These studies, along with supporting experimental evidence, show that photoexcitation of the conjugated enone initially prepares the singlet $S_1(n,\pi^*)$ state. This is followed by nonradiative decay (intersystem crossing) along a pathway that includes the lowest-energy triplet $T(n,\pi^*)$ or $T(\pi,\pi^*)$ triplet potential-energy surface (or both). The triplet states are relatively long-lived and reactive. Therefore the investigation of $S_1(n,\pi^*)$ state is important in understanding the mechanism of the photochemical reactions of enones.

The research work presented in this chapter will characterize the $S_1(n,\pi^*)$ electronic state of 2CHO and the ground and $S_1(n,\pi^*)$ electronic states of 2CHO- d_3 by analyzing the $S_1(n,\pi^*) \leftarrow S_0$ vibronic band system observed for these two compounds by cavity ringdown spectroscopy (CRDS). The $S_1(n,\pi^*) \leftarrow S_0$ CRD spectrum of 2CHO was also presented in the previous chapter but the ring-inversion potential function for the $S_1(n,\pi^*)$ state was not determined. This work will report additional CRD data for 2CHO that requires data to determine the ring-inversion potential energy function for the S_1 state. CRDS,³⁶ rather than fluorescence excitation, was chosen for the experiment because CRDS is based on absorption and is therefore amenable to molecules such as 2CHO that are subject to rapid nonradiative decay processes. Moreover, the $\pi^* \leftarrow n$ transitions of ketones and enones are orbitally forbidden and hence typically several

orders of magnitude weaker than fully allowed $\pi^* \leftarrow \pi$ transitions. The high sensitivity of the CRD techniques permits observation of the weak $\pi^* \leftarrow n$ transitions readily.

EXPERIMENTAL AND COMPUTATIONAL

The CRDS experimental work was carried out at the University of Wisconsin-Eau Claire and the complete CRDS experimental setup was described in the previous chapter. DFT calculations were carried out by Dr. J. Choo by utilizing the same programs and methods previously described for 2CPO.^{21,65}

RESULTS AND DISCUSSION

Vibronic analysis

Figures 25 and 26 show the CRD spectra for 2CHO and 2CHO- d_3 in the 26,000 to 26,700 cm^{-1} region (385 to 375 nm). The vertical axis indicates fractional photon loss per pass through the cell. The band origins (0_0^0) for the two isotopomers are 26,081.3 cm^{-1} and 26,075.3 cm^{-1} , respectively. The value of 26,089.1 cm^{-1} reported for the origin of 2CHO in the previous chapter was incorrect because it inadvertently neglected to convert the calibrated air wavelengths to vacuum. This correction also has changed the wavenumber values reported for some of the vibrational transitions in Chapter VI and the corrected values will be illustrated here.

The assignments in Figure 25 are based on a series of attached bands observed at approximately 99- cm^{-1} intervals in the d_0 spectrum and extending in the low-frequency direction. An analogous series is observed in the d_3 spectrum at 95- cm^{-1} intervals. These are identified as hot bands and assigned as a progression in ν_{39}'' (ground-state ring inversion), based on the fundamental frequency for this mode in the S_0 state which is already determined. These hot bands were analyzed to determine the inversion potential energy function for the S_0 state.

Several other low-frequency fundamentals for the S_1 state have been assigned and are listed in Tables 12 and 13. These include ν_{38} (ring bending), ν_{37} (C=C twist), and ν_{36} (carbonyl deformation). These band assignments were made based on similarity to

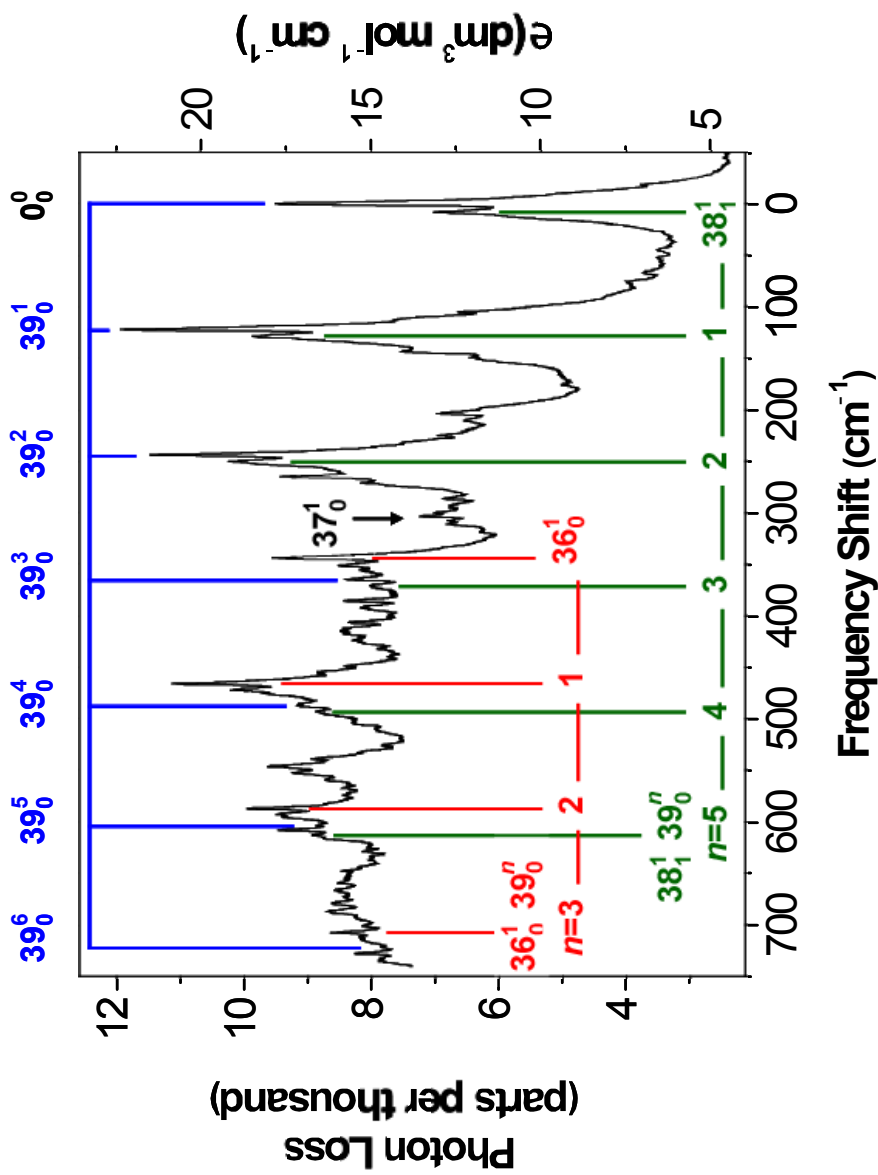


Figure 25. CRD spectrum of 2CHO vapor at room temperature. The pressure in the sample cell was 13 Pa (0.1 torr). This spectrum is a composite of several scans recorded over adjacent wavelength regions near the $S_1(n,\pi^*) \leftarrow S_0$ origin. Frequencies are relative to the 0_0^0 band at $26,081.3 \text{ cm}^{-1}$. Colored tie lines attached to an assigned origin indicate a progression in the excited-state inversion mode (ν_{39}).

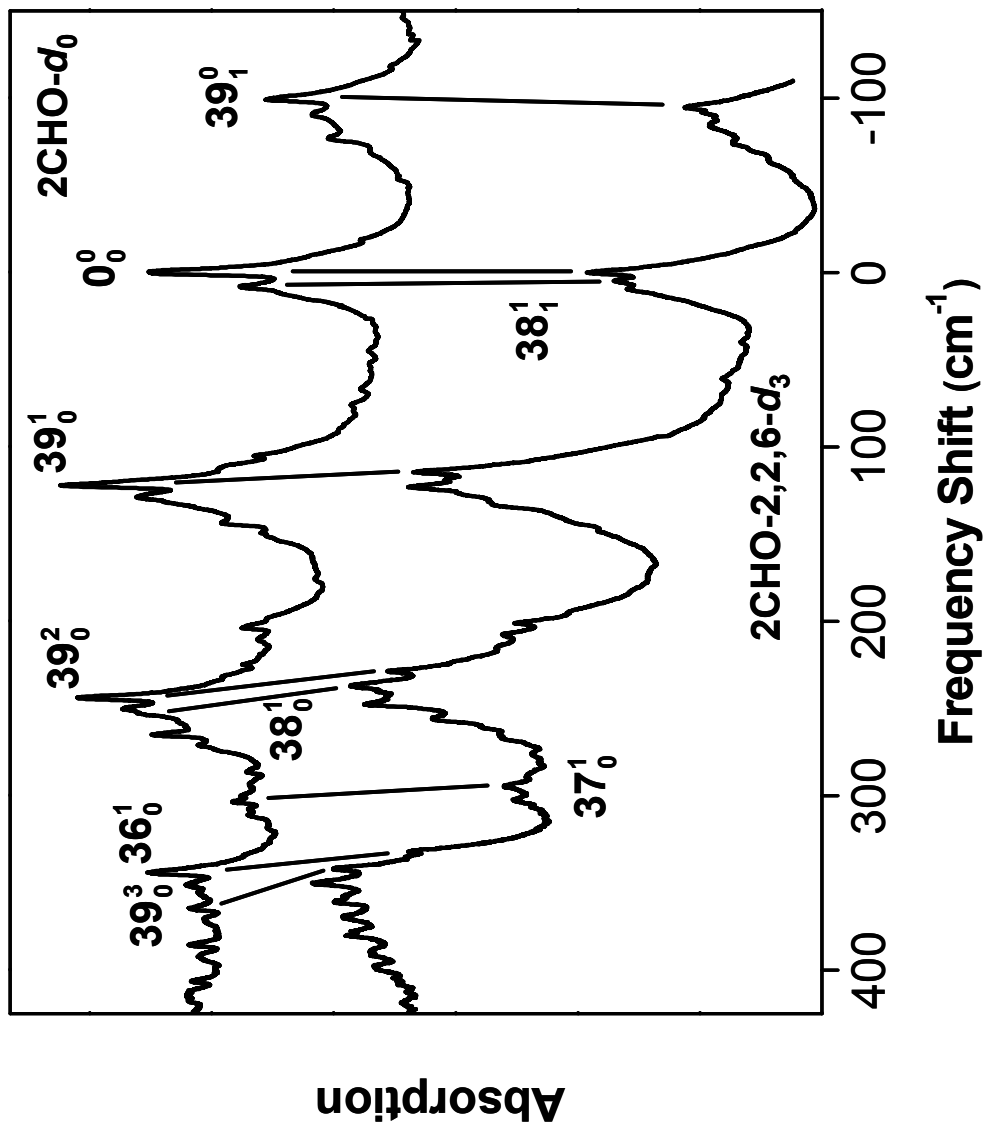


Figure 26. Comparison of CRD spectra for $\text{CHO}-d_0$ and $\text{CHO}-d_3$. Frequencies are relative to the respective $S_1 \leftarrow S_0$ band origins, 26,081.3 cm^{-1} for $\text{CHO}-d_0$ and 26075.3 cm^{-1} for $\text{CHO}-d_3$.

Table 12: CRD transition frequencies^a (in cm⁻¹) and assignments for 2CHO

Observed	Inferred ^b	Calculated ^c	Assignment	
-303.2	-303.2	308	37 ₁ ⁰	
-294.8	-293.9		39 ₃ ⁰	
-243.0	-243.8	241	38 ₁ ⁰	251.9 – 8.1
-197.0	-197.0		39 ₂ ⁰	
-191.7	-190.5		38 ₁ 39 ₂ ⁰	251.9 – 442.2
-99.2	-99.0 ^d	103	39 ₁ ⁰	
-90.5	-91.7		38 ₁ 39 ₁ ⁰	251.9 – 343.6
-76.9	-74.9		39 ₂ ¹	122.1 – 197.0
8.1	8.1		38 ₁ ¹	251.9 – 243.8
29.0	29.0		38 ₁ 39 ₁ ¹	372.6 – 343.6
44.9	46.8		39 ₂ ²	243.8 – 197.0
52.5	50.6		38 ₁ 39 ₂ ²	492.8 – 442.2
55.9 sh	54.9		38 ₀ 39 ₂ ⁰	251.9 – 197.0
122.1	122.1	121	39 ₀ ¹	
128.8	128.8		38 ₁ 39 ₀ ¹	372.6 – 243.8
143.5	144.8		39 ₁ ²	243.8 – 99.0
151.0	149.2		38 ₁ 39 ₁ ²	492.8 – 343.6
152.9 sh	152.9		38 ₀ 39 ₁ ⁰	251.9 – 99.0
168.6	167.5		39 ₂ ³	364.5 – 197.0
203.5	204.3		37 ₀ 39 ₁ ⁰	303.3 – 99.0
243.8	243.8		39 ₀ ²	
243.8	244.9		36 ₀ 39 ₁ ⁰	343.9 – 99.0
250.0	249.0		38 ₁ 39 ₀ ²	492.8 – 243.8
251.9	251.9	250	38 ₀ ¹	
264.9	265.5		39 ₁ ³	364.5 – 99.0
270.9 sh	269.2		38 ₁ 39 ₁ ³	612.8 – 343.6
273.9 sh	273.6		38 ₀ 39 ₁ ¹	372.6 – 99.0
303.3	303.3	298	37 ₀ ¹	
343.9	343.9	342	36 ₀ ¹	
364.5	364.5		39 ₀ ³	

Table 12: (Continued)

Observed	Inferred ^b	Calculated ^c	Assignment	
371.1	369.0		$38_1^1 39_0^3$	612.8 – 243.8
385.3	385.4		39_1^4	484.4 – 99.0
425.4 sh	425.4		$37_0^1 39_0^1$	
465.9	465.9		$36_0^1 39_0^1$	
485.3 sh	484.4 ^d		39_0^4	
487.5	488.2		$36_0^1 39_1^2$	587.2 – 99.0
492.8	492.8		$38_0^1 39_0^2$	
502.2 sh	504.6		39_1^5	603.6 – 99.0
587.2	587.2		$36_0^1 39_0^2$	
603.6	603.6		39_0^5	
607.8	608.5		$36_0^1 39_1^3$	707.5 – 99.0
612.8	612.8		$38_0^1 39_0^3$	
687.0	687.0		36_0^2	
707.5	707.5		$36_0^1 39_0^3$	
721.5	721.5		39_0^6	

^a Frequencies are relative to the $S_1 \leftarrow S_0$ electronic origin at $26,081.3 \text{ cm}^{-1}$. Uncertainty in the relative frequency is $\pm 0.5 \text{ cm}^{-1}$.

^b Inferred values are based on the energy level diagram in Figure 27.

^c Calculated using B3LYP/6-311+G(d,p) level of theory.

^d The inferred frequencies for the 39_1^0 and 39_0^4 bands were determined from patterns established by other observed ν_{39} overtones. The inferred values for these two bands were used in the ν_{39} potential energy function determinations. The observed band maxima in these cases lead to poorer potential energy fits, most likely because the rotationless band centers (unavailable at the present spectral resolution) are not necessarily coincident with the maxima.

Table 13: CRD transition frequencies^a (in cm⁻¹) and assignments for 2-CHO-*d*₃

Observed	Inferred ^b	Calculated ^c	Assignment	
-300.0	-300.0	-302	37 ₁ ⁰	
-232.3	-232.3	-224	38 ₁ ⁰	
-187.6	-187.6		39 ₂ ⁰	
-94.7	-94.7	-97	39 ₁ ⁰	
-74.2	-73.2		39 ₂ ¹	114.4 – 187.6
4.6	4.6		38 ₁ ¹	236.9 – 232.3
26.6	26.6		38 ₁ ¹ 39 ₁ ¹	350.4 – 323.8
40.0	41.0		39 ₂ ²	228.6 – 187.6
48.1 sh	49.3		38 ₀ ¹ 39 ₂ ⁰	236.9 – 187.6
114.4	114.4	114	39 ₀ ¹	
118.9	118.1		38 ₁ ¹ 39 ₀ ¹	350.4 – 232.3
133.1	133.9		39 ₁ ²	228.6 – 94.7
143.0 sh	142.2		38 ₀ ¹ 39 ₁ ⁰	236.9 – 94.7
154.1 sh	154.2		39 ₂ ³	341.8 – 187.6
201.0	199.9		37 ₀ ¹ 39 ₁ ⁰	294.6 – 94.7
228.6	228.6		39 ₀ ²	
236.9	236.9	236	38 ₀ ¹	
236.9	237.3		36 ₀ ¹ 39 ₁ ⁰	332.0 – 94.7
247.6	247.1		39 ₁ ³	341.8 – 94.7
256.0	255.7		38 ₀ ¹ 39 ₁ ¹	350.4 – 94.7
294.6	294.6	289	37 ₀ ¹	
332.0	332.0	332	36 ₀ ¹	

Table 13: (Continued)

Observed	Inferred ^b	Calculated ^c	Assignment
341.8	341.8		39_0^3
350.4	350.4		$38_0^1 39_0^1$
407.7	407.7		$37_0^1 39_0^1$
446.2	446.2		$36_0^1 39_0^1$
466.1	465.3		$36_0^1 39_1^2$ 560.0 – 94.7
560.0	560.0		$36_0^1 39_0^2$
665.2	665.2		36_0^2
673.4	673.4		$36_0^1 39_0^3$

^a Frequencies are relative to the $S_1 \leftarrow S_0$ electronic origin at 26,075.3 cm^{-1} .
Uncertainty in the relative frequency is $\pm 0.5 \text{ cm}^{-1}$.

^b Inferred values are based on the energy level diagram in Figure 28.

^c Calculated using B3LYP/6-311+G(d,p) level of theory

the corresponding fundamental vibrational frequencies in the ground state. Frequencies and deuterium shifts predicted from the DFT calculation (discussed below) also support these assignments.

The ν_{38} out-of-plane ring mode has the second-lowest fundamental frequency, 243.0 cm^{-1} in the S_0 state and 251.9 cm^{-1} in the S_1 state for the d_0 isotopomer. At room temperature the $v''_{38} = 1$ ground-state level has an appreciable Boltzmann factor (0.3), allowing the 38_1^1 sequence band to appear with relatively large intensity in the CRD spectrum. This band appears at 8.1 cm^{-1} relative to the origin in the d_0 spectrum, consistent with the value of 8.9 cm^{-1} obtained from the $38_0^1 - 38_1^0$ combination difference. In the d_3 spectrum this combination difference is 4.6 cm^{-1} and is reproduced exactly by the 38_1^1 band observed at 4.6 cm^{-1} relative to the origin.

Several of the prominent bands in the CRD spectra, including 38_1^1 and 36_0^1 , serve as origins for the 122-cm^{-1} (d_0) or 114-cm^{-1} (d_3) progression in the upper-state inversion mode, ν_{39} . The frequencies of these progressions are listed in Tables 12 and 13.

Potential energy functions for ring inversion

Figures 27 and 28 present energy maps for the lower energy quantum states of 2CHO and the d_3 isotopomer. The data for ν_{39} for CHO in the S_0 ground state were previously used to determine its potential energy function. Similar data for the CHO- d_3 will be used in the present work to calculate the quantum states for this isotopomer in the S_0 state. The $S_1(n,\pi^*)$ data in Figures 27 and 28 for both isotopomers will then be used to determine the potential energy functions for the excited state.

In order to determine the ring-inversion potential energy functions, the kinetic energy (reciprocal reduced mass) expansion must first be calculated. This is based on the structure of the molecule which was calculated by DFT methods using the B3LYP/6-311+G(d,p) level for both the S_0 ground state and the $S_1(n,\pi^*)$ electronic excited state. Figure 29 compares the calculated structures for these two states. As can be seen, the excitation to a π^* anti-bonding orbital increases the C=C and C=O bond distances as

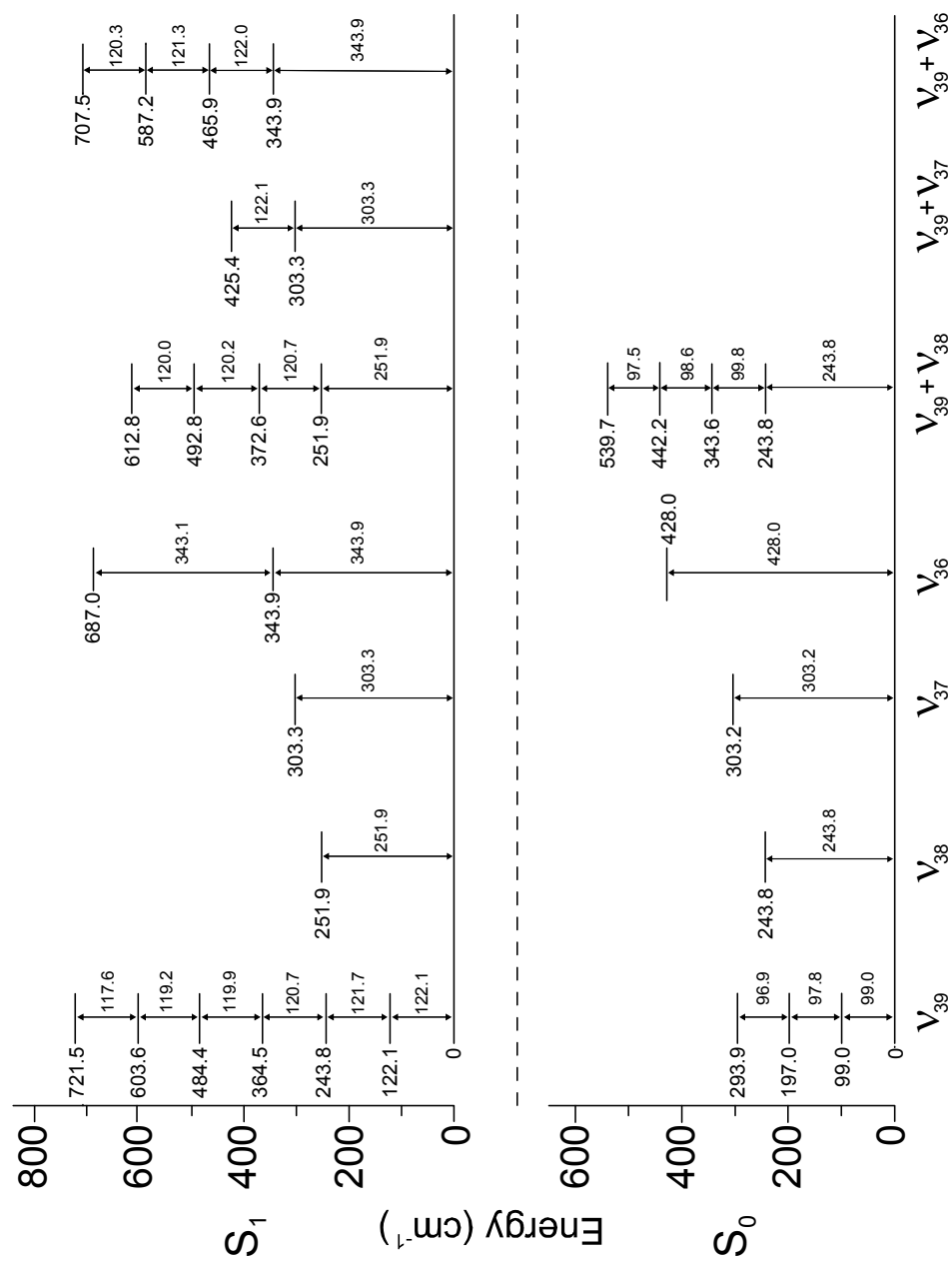


Figure 27. Energy map for 2CHO in its S_0 and $S_1(n,\pi^*)$ electronic states.

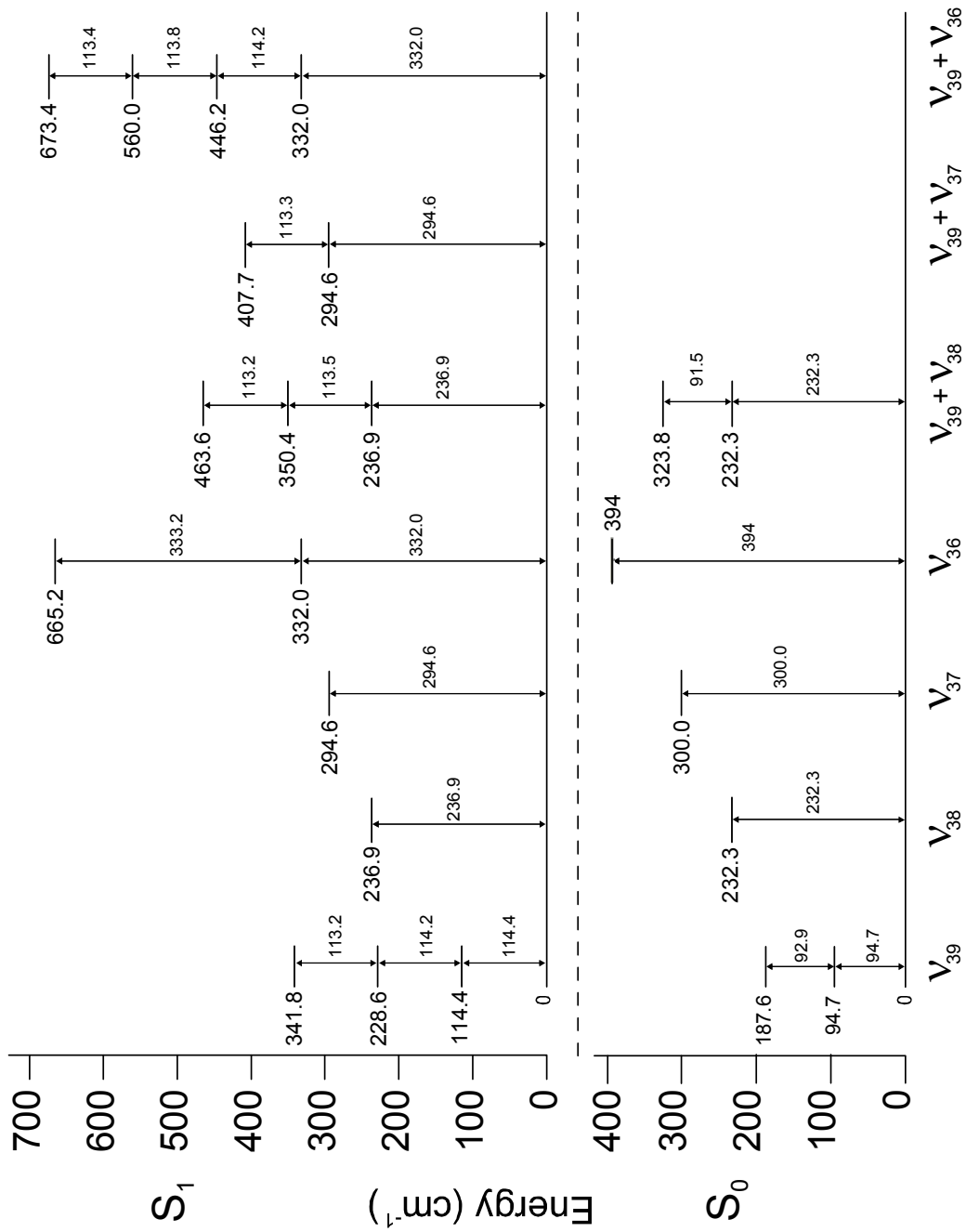


Figure 28. Energy map for 2CHO- d_3 in its S_0 and $S_1(n, \pi^*)$ electronic states.

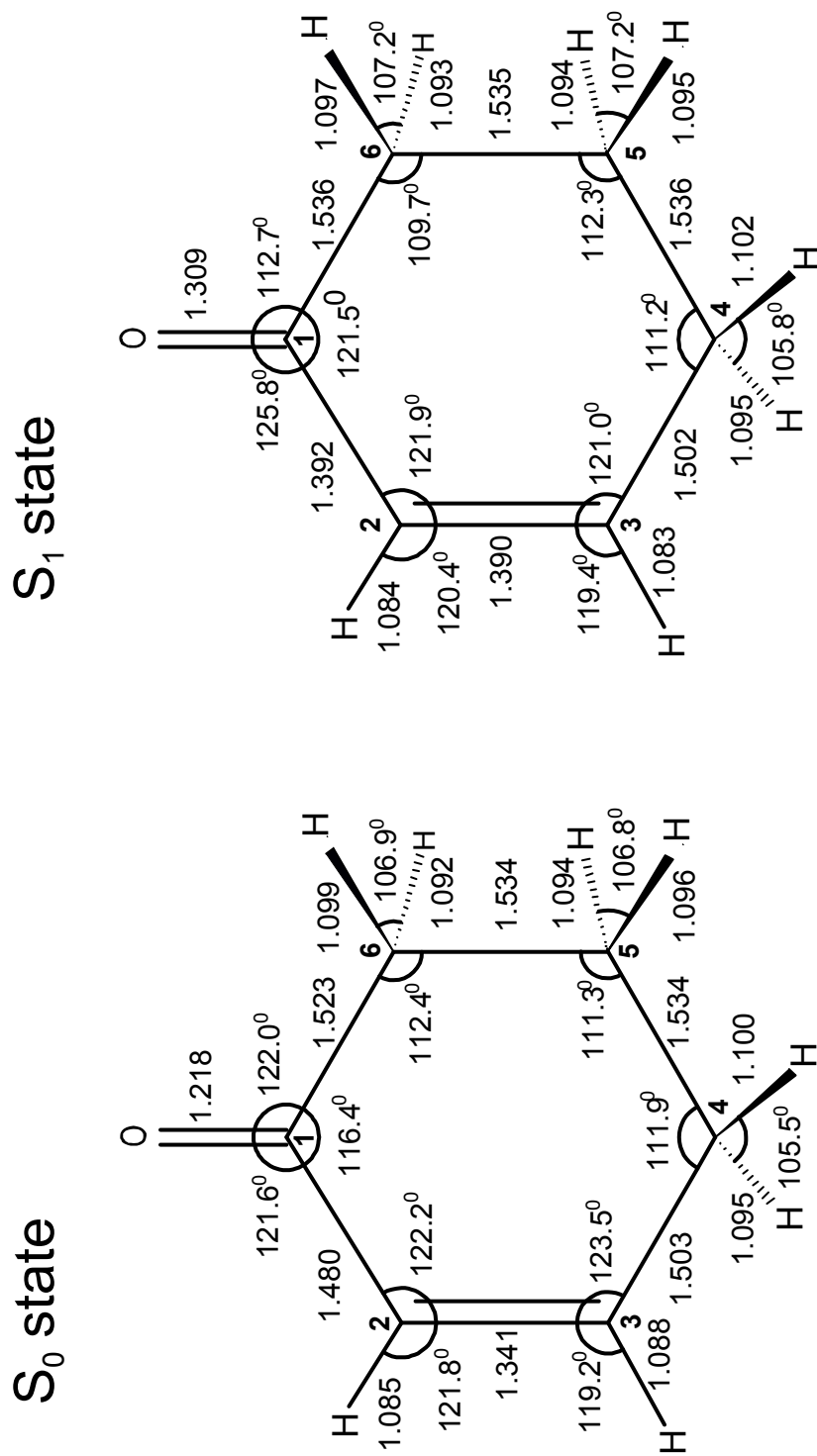


Figure 29. Calculated structures for 2CHO in its S₀ and S₁(n,π*) electronic states.

expected. However, the =C-C(O) bond distance between carbon atoms 1 and 2 decreases from 1.480 to 1.392 Å. Similar changes occur in the 2CPO molecule as a result of $\pi^* \leftarrow n$ excitation.^{20,21} In those cases the bond shortening was explained on the basis of the character of the π^* molecular orbitals involved in the conjugation. A qualitative picture of this orbital is shown in Figure 30 for both molecules. As can be seen the C=C and C=O linkages increase in antibonding character whereas the C1-C2 linkage has bonding character in this π^* orbital.

The ring-inversion coordinate S was previously defined^{66,67} and for S_0 involves mostly carbon atoms 6 (next to the C=O group) and 5 moving out of plane. The displacements of carbon atoms 1, 4, 5, and 6 are shown in Table 14 for both S_0 and $S_1(n, \pi^*)$ states based on the DFT calculation. For S_1 an increased out of plane displacement of C4 can be seen as the conjugation is weakened with the $n \rightarrow \pi^*$ transition. For this coordinate the kinetic energy expansion $g_{44}(S)$ was calculated for both 2CHO and 2CHO- d_3 for both S_0 and $S_1(n, \pi^*)$ states and the coefficients are shown in Table 15. The expansion has the form

$$g_{44}(S) = g_{44}^{(0)} + g_{44}^{(2)}S^2 + g_{44}^{(4)}S^4 + g_{44}^{(6)}S^6 \quad (7.1)$$

where the $g_{44}^{(j)}$ are the coefficients in Table 15. With the availability of the $g_{44}(S)$ expressions, the Hamiltonian

$$\mathcal{H} = -\frac{\hbar^2}{2m} \frac{d}{dS} g_{44}(S) \frac{d}{dS} + V(S) \quad (7.2)$$

Where

$$V(S) = aS^4 - bS^2 \quad (7.3)$$

was used to determine the potential energy parameters a and b which provide the best fit for the experimental data. The potential function for the ground state of 2CHO is

$$V(\text{cm}^{-1}) = 7.459 \times 10^2 S^4 - 2.378 \times 10^3 S^2 \quad (7.4)$$

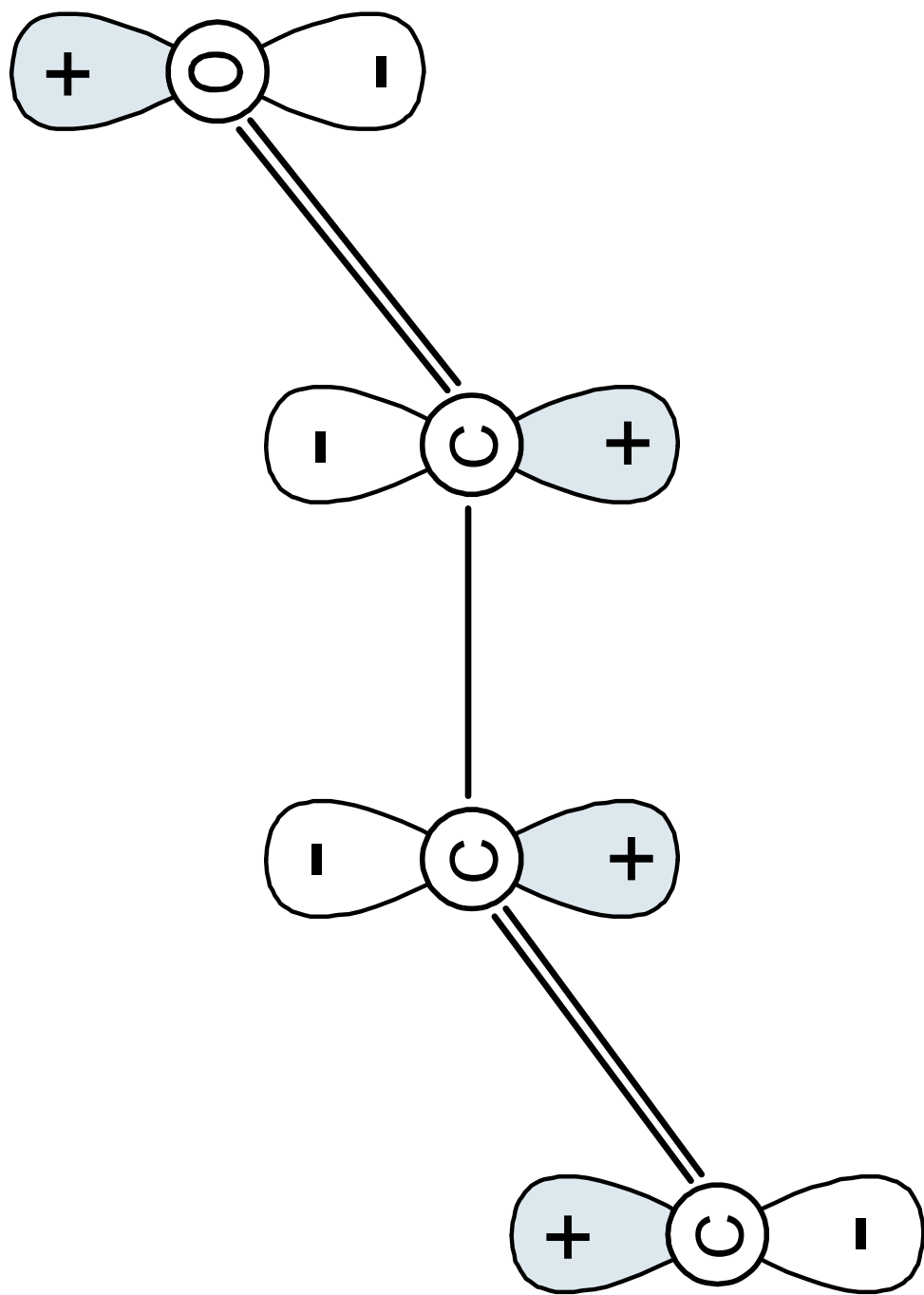


Figure 30. Qualitative picture of the π^* orbital involved in the $n \rightarrow \pi^*$ transition of 2CHO and 2CPO.

Table 14: Calculated^a relative out-of-plane displacements (Å) of C1, C4, and C6 atoms of 2CHO in its S₀ and S₁(n,π^{*}) states

	S ₀	S ₁
C1	0.017523	0.014228
C4	0.130933	0.202797
C5	-0.339025	-0.340520
C6	0.269044	0.200370

^a Calculated using B3LYP/6-311+G(d,p) level of theory

Table 15: Calculated^a kinetic energy coefficients of 2CHO and 2CHO-*d*₃

		$g_{44}^{(0)}$	$g_{44}^{(2)}$	$g_{44}^{(4)}$	$g_{44}^{(6)}$
S ₀	2CHO	0.03119	-0.04782	-0.11530	0.14896
	2CHO- <i>d</i> ₃	0.02588	-0.02238	-0.14263	0.13538
S ₁	2CHO	0.03211	-0.05834	-0.13086	0.22699
	2CHO- <i>d</i> ₃	0.02775	-0.03713	-0.14440	0.16731

^a Coefficients are uÅ^{-j} for each $g_{44}^{(j)}$

which is reported in the previous chapter and this provides an excellent fit for the S_0 data. The barrier to inversion is 1895 cm^{-1} . This same function should in principle also reproduce the d_3 data when using the correct reduced mass ratio between the d_0 and d_3 isotopomers. This ratio is calculated to be 1.205 (Table 15), but this value results in calculated frequencies which are about 4% too low when Eq. (7.4) is used. This is not too surprising since the one-dimensional vibrational model ignores the interactions of the ring-inversion with the other 38 vibrations of the molecule. To obtain a satisfactory fit using Eq. (7.4) for the d_3 calculation the reduced mass ratio was adjusted to 1.094. Table 16 compares the observed and calculated energy separation for $2\text{CHO-}d_0$ and $-d_3$ based on Eq. (7.4) and the adjusted reduced mass ratio. Figure 31 shows this function along with the observed transitions. As discussed previously, the barrier height value is obtained by extrapolation and its accuracy is only $\pm 300\text{ cm}^{-1}$.

Using the data in Tables 14 and 15 and Figure 29 similar calculations were carried out for 2CHO and $2\text{CHO-}d_3$ for the $S_1(n,\pi^*)$ state. The potential function was determined to be

$$V(\text{cm}^{-1}) = 8.586 \times 10^2 S^4 - 3.493 \times 10^3 S^2 \quad (7.5)$$

and the observed and calculated frequencies are shown in Table 16. In this case the calculated reduced mass ratio of 1.157 differs only slightly from the observed value of 1.146, which was used for the computation. If the higher value for the ratio is used, a frequency error of less than 1% would result. Figure 32 shows this function and the observed ν_{39} quantum spacings in the $S_1(n,\pi^*)$ state for both isotopomers. As can be seen for 2CHO the observed transitions extend to about 800 cm^{-1} above the energy minimum so the barrier of 3552 cm^{-1} is again obtained by extrapolation. Its uncertainty is estimated to be $\pm 500\text{ cm}^{-1}$.

Table 16: Observed and calculated frequencies (in cm^{-1}) for the ν_{39} vibration of $2\text{CHO-}d_0$ and $2\text{CHO-}d_3$ in their S_0 state

Separation	$2\text{CHO-}d_0$		$2\text{CHO-}d_3$	
	Experimental ^a	Calculated	Experimental ^a	Calculated
0-2	99.0	99.0	94.7	94.7
2-4	98.0	98.0	92.9	93.8
4-6	96.9	96.9		

^a $V (\text{cm}^{-1}) = 7.459 \times 10^2 S^4 - 2.378 \times 10^3 S^2$

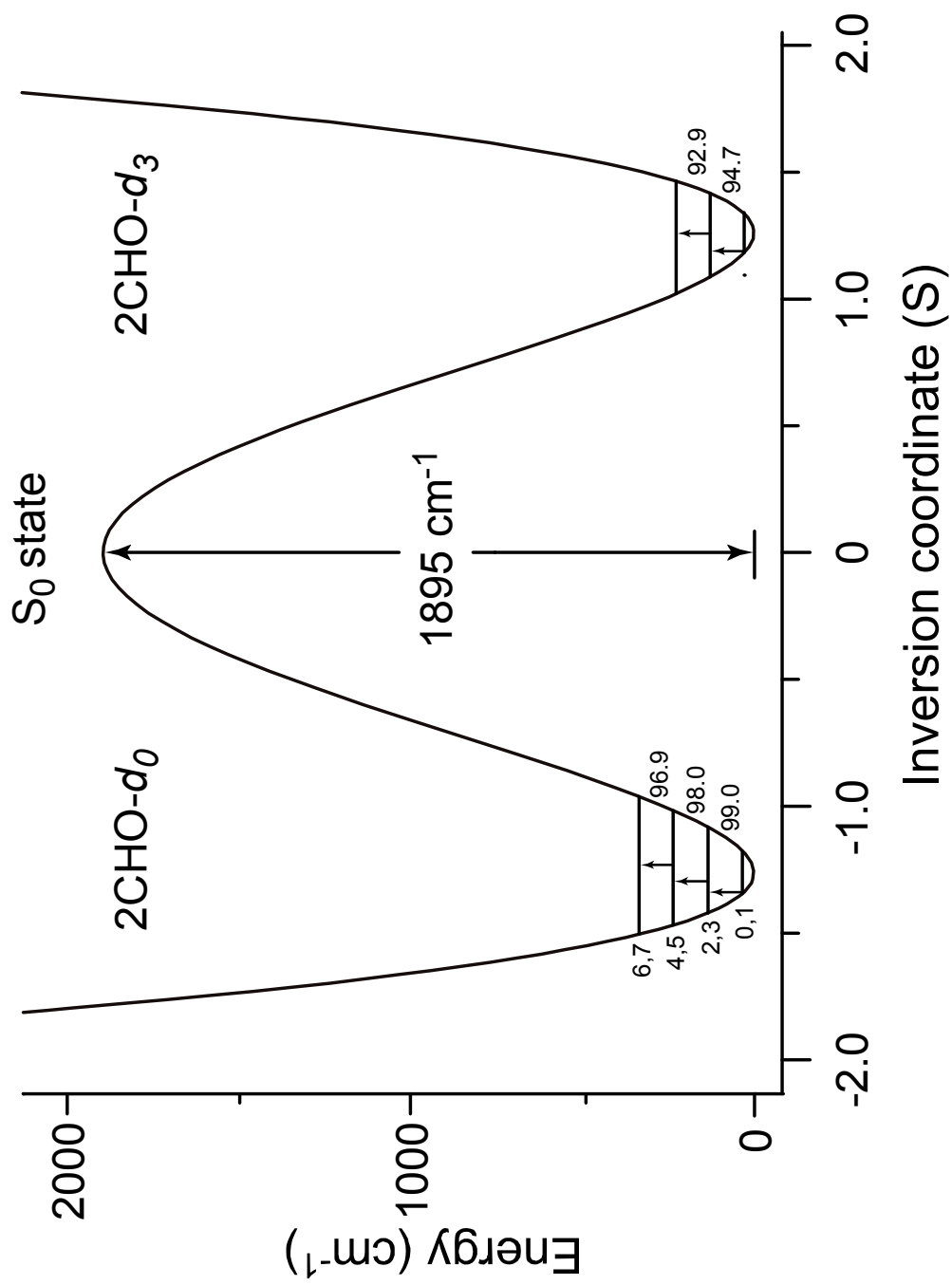


Figure 31. Ring-inversion potential energy function for 2CHO and 2CHO- d_3 in their S_0 state.

Table 17: Observed and calculated frequencies (in cm^{-1}) for the ν_{39} vibration of $2\text{CHO-}d_0$ and $2\text{CHO-}d_3$ in their $S_1(\pi, \pi^*)$ state

Separation	$2\text{CHO-}d_0$		$2\text{CHO-}d_3$	
	Experimental ^a	Calculated	Experimental ^a	Calculated
0-2	122.1	122.2	114.4	114.4
2-4	121.7	121.4	114.2	113.7
4-6	120.7	120.5	113.2	113.1
6-8	119.9	119.8		
8-10	119.2	119.1		
10-12	117.9	118.5		

$$^a V (\text{cm}^{-1}) = 8.586 \times 10^2 S^4 - 3.493 \times 10^3 S^2$$

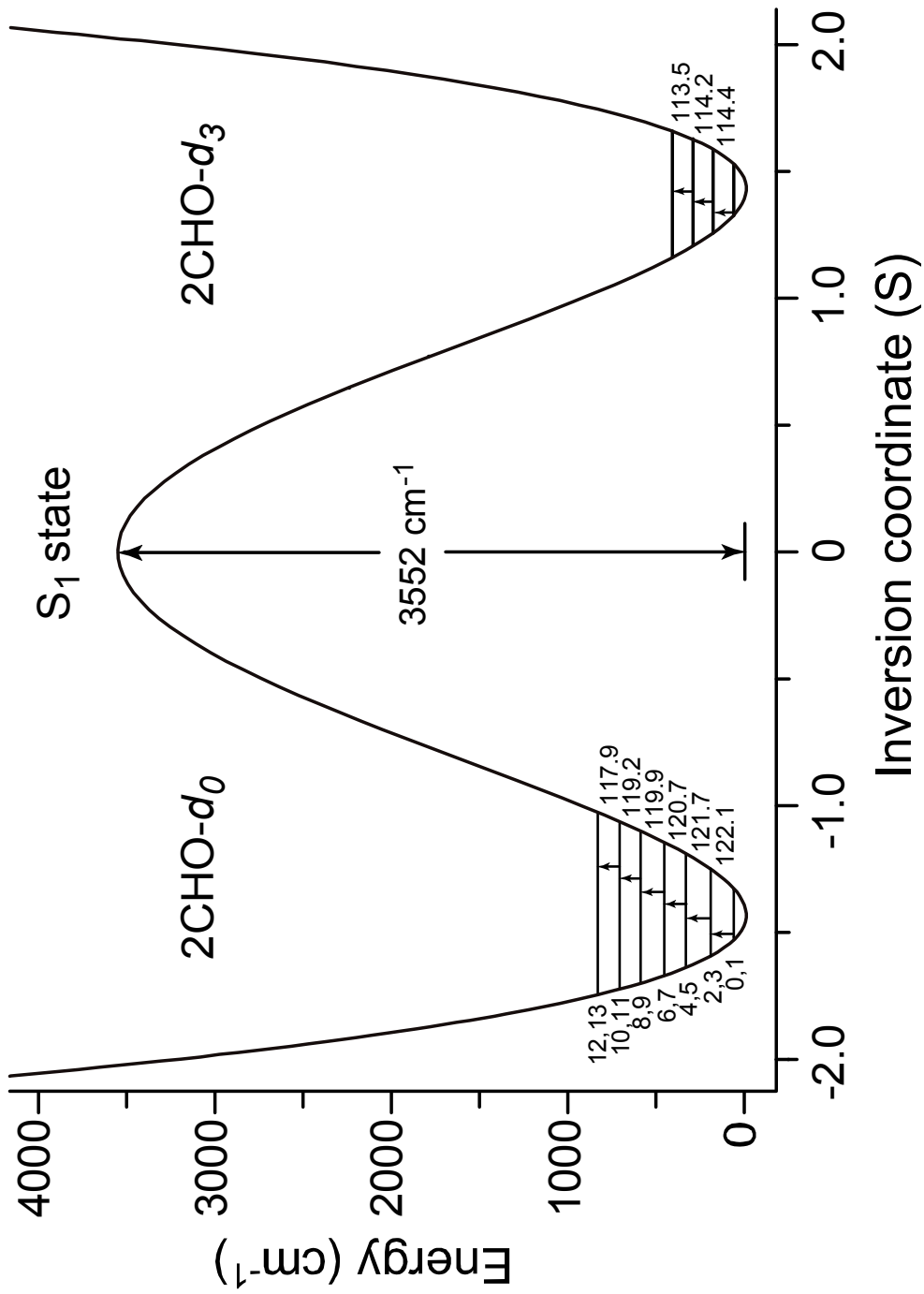


Figure 32. Ring-inversion potential energy function for 2CHO and 2CHO- d_3 in their $S_1(n, \pi^*)$ state.

Comparisons with DFT results

The DFT calculation using the B3LYP/6-311+G(d,p) basis set predicts a barrier of 2265 cm^{-1} for the $S_1(n,\pi^*)$ state, a value considerably lower than that in Figure 32. The DFT calculation also by definition places the energy minima at $S = \pm 1.0\text{ \AA}$ while Figure 32 has these at $\pm 1.4\text{ \AA}$. The conclusion then is that while the DFT calculation predicts a higher barrier for the $S_1(n,\pi^*)$ state than for S_0 , it clearly underestimates the barrier and degree of out-of-plane distortion. Most likely, however, our extrapolated experimental barrier is an overestimation. Nonetheless, it is clear that the excited state value is substantially higher than that in the electronic ground state. Figure 33 compares the two experimental potential energy curves.

Although the ν_{39} barrier height from the DFT calculation does not agree quantitatively with the S_1 potential fit, the DFT calculated ν_{39} fundamental frequency (122.1 cm^{-1}) agrees exceptionally well with that obtained from the CRD spectrum (121 cm^{-1}). The agreement is also excellent (typically within 2 cm^{-1} or less) for the other low-frequency fundamentals in the S_1 state.

CONCLUSIONS

The 2CHO molecule, like many conjugated enones, has nearly zero fluorescence quantum yield following photoexcitation to its $S_1(n,\pi^*)$ state. Therefore this excited state is most amenable to spectroscopic probes based on absorption rather than emission. The high sensitivity of the CRD absorption technique has allowed us to detect the relatively weak absorption spectra corresponding to transitions to the vibronic levels of the $S_1(n,\pi^*)$ state in 2CHO. The data allow the first several quantum states of ν_{39} , the ring-inversion vibration, in this electronic excited state as well as of several other low-frequency modes to be determined. The $S_1(n,\pi^*)$ barrier to inversion is found by extrapolation of the potential energy curve to be $3550 \pm 500\text{ cm}^{-1}$ as compared to $1900 \pm 300\text{ cm}^{-1}$ in the S_0 ground state. DFT calculations also predict the barrier in S_1 to be larger, but to a lesser degree. The increase in barrier height likely arises from the decreased conjugation allowing the six-membered ring to distort even further from a planar configuration.

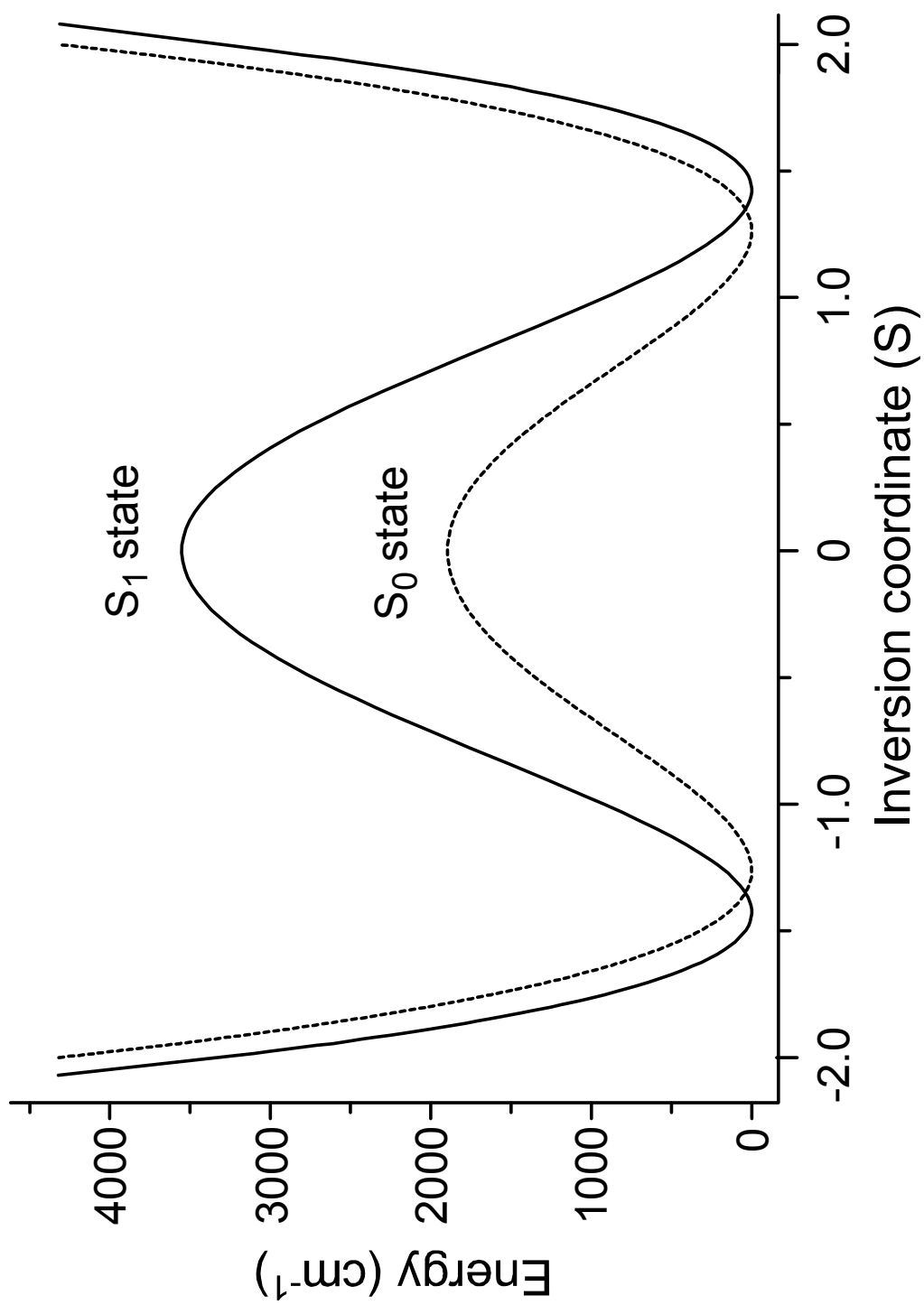


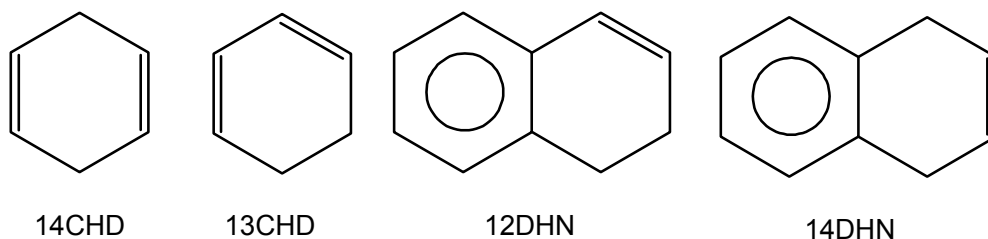
Figure 33. Comparison of the S_0 and $S_1(n,\pi^*)$ ring-inversion potential energy functions.

CHAPTER VIII

THE RING-PUCKERING POTENTIAL ENERGY FUNCTION OF 1,4-DIHYDRONAPHTHALENE IN ITS GROUND AND $S_1(\pi,\pi^*)$ ELECTRONIC STATES

INTRODUCTION

In 1971 Laane and Lord³ showed that 1,4-cyclohexadiene (14CHD) could be thought of as a pseudo four-membered ring molecule with respect to its ring-puckering vibration. The far-infrared spectrum of this molecule showed it to be planar although a previous electron diffraction study had postulated a puckered molecule.²⁵ In 1988 Strube and Laane²⁶ calculated the kinetic energy expression for this large-amplitude vibration and determined a quantitative vibrational potential energy function for the ring-puckering mode, again confirming that the molecule was planar. In 2001 Autrey et al.⁶⁶ reported the Raman and far-infrared spectra and ring-twisting potential energy function for 1,3-cyclohexadiene (13CHD) and showed this molecule to be twisted with a barrier to planarity of 1160 cm^{-1} . More recently the low-frequency vibrations of number of molecules^{12-14,72} including 1,2-dihydronaphthalene (12DHN)⁶⁷ in both their S_0 ground and $S_1(\pi,\pi^*)$ excited states were studied using laser induced fluorescence (LIF) and ultraviolet absorption spectra. One and two-dimensional potential energy functions were determined for many of these molecules. 12DHN has high barriers to planarity and twisted structures in both its S_0 and S_1 states.



The study presented in this chapter reports the ring puckering potential energy function of 14DHN in its S_0 and $S_1(\pi,\pi^*)$ electronic states determined by jet-cooled LIF,

single vibronic level fluorescence (SVLF), and room temperature ultraviolet absorption spectra. The structure of this molecule is closely related to those of 12DHN and 14CHD. The LIF spectra of 14DHN have been previously studied by Chakraborty et al. but the reported results did not provide sufficient data or wavenumber accuracy needed to calculate reliable puckering potential energy functions.³³ In fact, as will be seen later in this chapter, their conclusion that there is a barrier to planarity in both the S_0 and S_1 states is incorrect.

EXPERIMENTAL

14DHN was purchased from TCI America and purified by vacuum transfer, but the sample used for the spectral studies still contained a few percent of 12DHN. However, since the 12DHN was previously thoroughly studied⁶⁷ and since its electronic excitation is about 2700 cm^{-1} lower than that for 14DHN, it was easy to recognize the weak bands present from the impurity. The ultraviolet absorption spectra of the 14DHN sample (0.2 to 1 torr at 25 to 40 °C) were recorded in a 15 cm glass cell with quartz windows using a BOMEM DA8.02 Fourier transform spectrometer. The LIF spectra were recorded using the apparatus previously described⁷³⁻⁷⁹ based on a Continuum Sunlite OPO laser system.

EXPERIMENTAL RESULTS

Figure 34 shows the jet-cooled fluorescence excitation spectra (FES) along with the UV absorption spectra for 14DHN in the 0 to 250 cm^{-1} region above the electronic absorption 0_0^0 at $36,788.6\text{ cm}^{-1}$. The better resolved FES bands can be seen to be of type B with the missing Q branch corresponding to $B_2 \leftrightarrow A_2$ electronic transitions. The figure labels several of the spectral bands important for determining the ring-puckering quantum states for both S_0 and S_1 . Figure 35 shows the UV spectra below the 0_0^0 band and compares it to the SVLF spectra from the 0_0^0 and 54_0^2 ($0_0^0 + 157.2\text{ cm}^{-1}$) excitations.

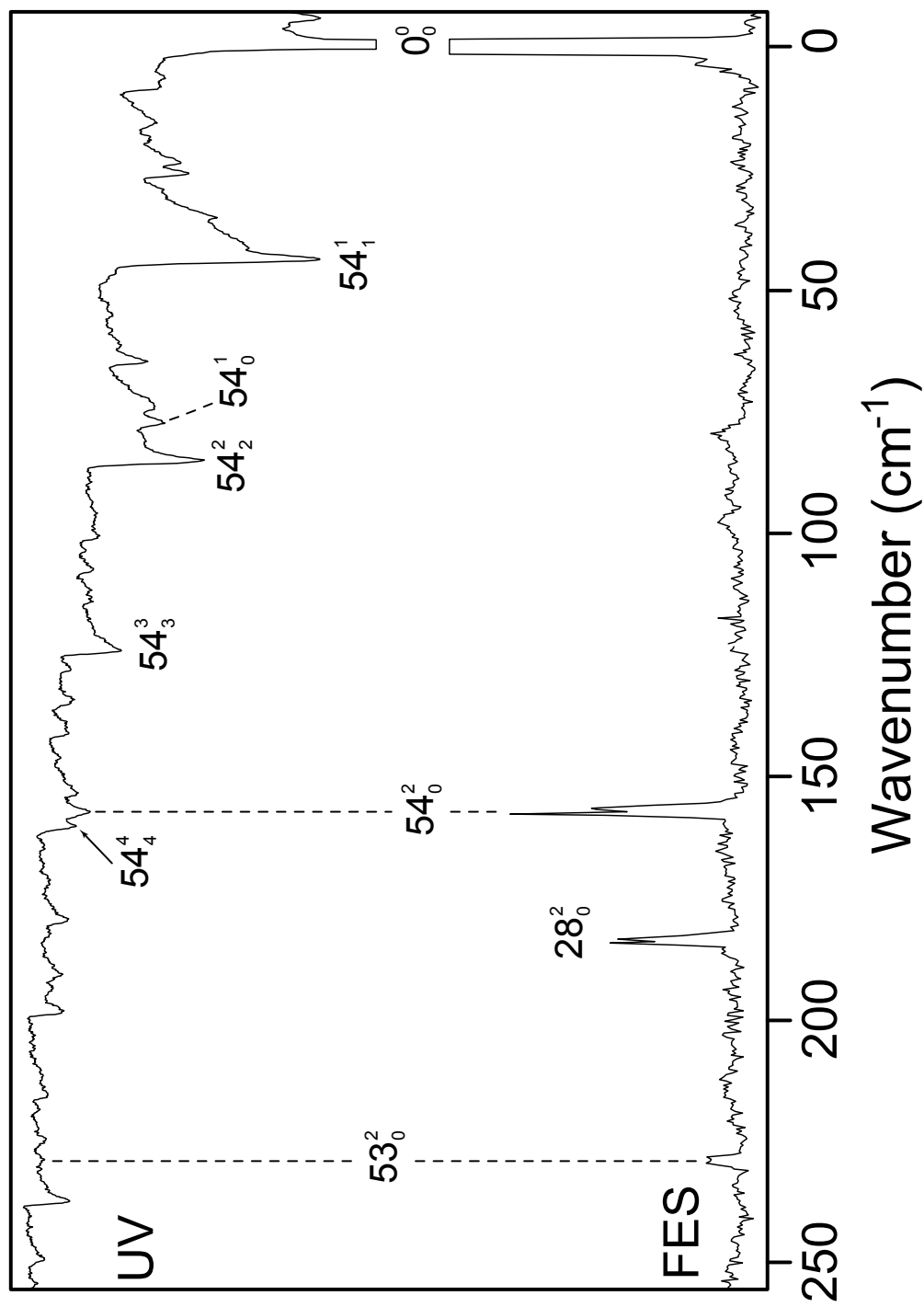


Figure 34. Fluorescence excitation (bottom) and ultraviolet absorption spectra (top) of 14DHN. The wavenumbers are relative to the 0_0^0 band at $36,788.6 \text{ cm}^{-1}$.

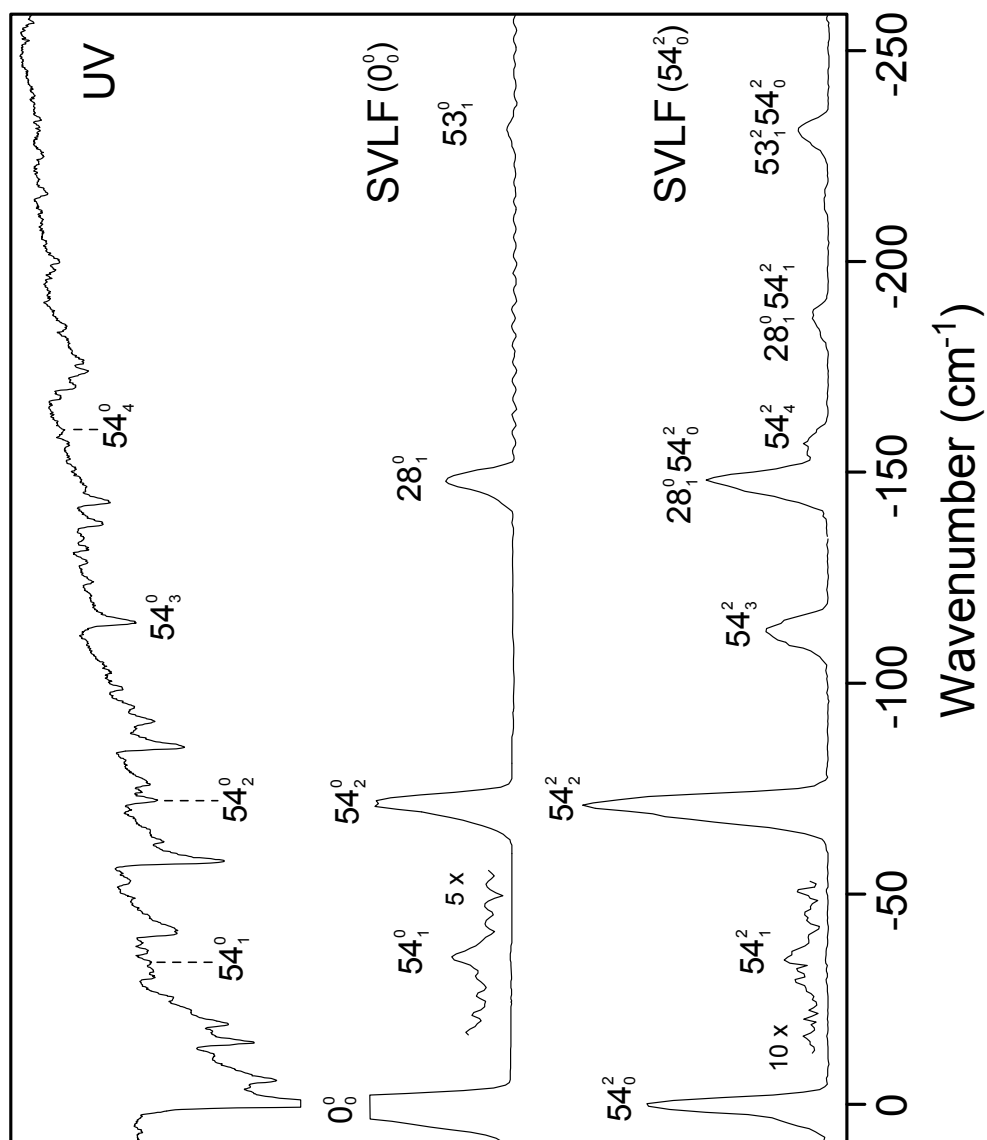


Figure 35. SVLFL spectra of 14DHN from 0_0^0 and 54_0^2 excitation bands compared to the UV spectra in the same region. The 54_0^2 SVLFL spectrum has been offset by 157 cm^{-1} to allow easier comparison with other spectra.

The observed frequencies and assignments are tabulated in Table 18 and compared to the results of Chakraborty et al.³³. From these data the first several puckering levels for the S_0 and S_1 states were determined from several transitions and these were used for the potential energy calculations described below. As Table 18 shows, the correspondence between the observed UV, SVLF and FES values (whose resolutions are 0.25, 2, and 1 cm^{-1} , respectively) and the inferred puckering levels is excellent. The jet-cooled LIF spectra show only transitions from the lowest vibrational state, whereas the ambient temperature UV spectra also show transitions from higher puckering levels. The out-of-plane ring-puckering vibration has B_2 symmetry for the C_{2v} molecule assumed to lie in the xy plane. Hence the ring-puckering transitions with $\Delta v_p = 0, 2, \dots$ transitions for the puckering quantum number v_p are expected to be considerably more intense than those with odd quantum number changes. This is evident in Figure 34 and Table 18 where a strong series of $\Delta v_p = 0$ bands corresponding to the $1 \rightarrow 1, 2 \rightarrow 2, 3 \rightarrow 3, \dots$ transitions are evident. Nonetheless, weak $\Delta v_p = \pm 1$ transitions can also be seen. As listed in Table 18 Chakraborty and co-workers³³ also observed the stronger transitions in their work but with less wavenumber accuracy. Their $4 \rightarrow 0$ assignment at -150 cm^{-1} in the SVLF spectra to 54_4^0 is mistaken as this fairly strong band corresponds to 28_1^0 for the ring twisting. A shoulder on the high frequency side is actually 54_4^0 and its band center in the UV is at 160.1 cm^{-1} . It should also be noted that in the earlier work³³ the authors labeled their quantum states as $0^+, 0^-, 1^+, 1^-, 2^+ \dots$ based on the erroneous assumption that the molecule had a barrier to inversion. The energy levels presented here are labeled as 0, 1, 2, 3, 4, The spectra in Figures 34 and 35 also allow the assignment of the low-frequency ring-twisting (ν_{28}) and ring-flapping (ν_{53}) vibrations. For S_0 state these are at 148 and 231 cm^{-1} , respectively, while for $S_1(\pi, \pi^*)$ these drop to 92 and 115 cm^{-1} . These assignments are supported by the *ab initio* calculations which place these at 146 and 235 cm^{-1} for S_0 and 69 and 97 cm^{-1} for $S_1(\pi, \pi^*)$. As is usually the case, the excited state calculated values are somewhat less accurate but they do show that the frequencies have dropped substantially.

Table 18: Fluorescence excitation (FES) and ultraviolet (UV) absorption bands (in cm^{-1}) of 14DHN involving the ring-puckering (ν_{54}) vibration^a

	Transition ^b	FES	SVLF		UV	Inferred ^c	CDL ^d
			0_0^0	54_0^2			
Ring-puckering	54_4^0	----	----	-157 m	-160.1 vw	-160.1	-150 ^e
	54_3^0	----	----	-112 s	-114.4 ms	-114.4	----
	54_2^0	----	-71 m	-71 vvs	-72.2 s	-72.2	-72
	54_1^0	----	-35 vvW	-35 vvW	-33.8 w	-33.8	----
	0_0^0	0 vvs	0 vvs	0 vvs	0 ^f vvs	0	----
	54_1^1	----	----	----	43.7 vs	43.6	44
	54_2^2	----	----	----	85.0 s	85.0	85
	54_3^3	----	----	----	124.1 ms	124.0	----
	54_4^4	----	----	----	160.2 m	160.7	----
	54_0^1	----	----	----	77.2 m	77.4	----
	54_0^2	157 s	----	----	157.2 ms	157.2	156
	54_0^3	----	----	----	----	238.4	----
	54_0^4	----	----	----	320.8 w	320.8	----
	Other vibrations	28_0^2	184 ms	----	----	----	----
53_0^2		229 m	----	----	228.6 vw	----	----
28_1^0		----	-148 m	-148 vs	----	----	----
53_1^0		----	-231 w	-231 s	----	----	----
$28_1^0 54_1^0$		----	----	-187 ms	----	----	----

^a v – very, s – strong, m – medium, w - weak

^b The transitions are labeled with respect to UV, FES and 0_0^0 SVLF spectra

^c Inferred from assignments in Table 2.

^d FES or SVLF values for reference 33.

^e This band at -148 cm^{-1} corresponds to 28_1^0 , the ring-twisting

^f 0_0^0 level at $36,788.6 \text{ cm}^{-1}$

COMPUTATIONS

Figure 36 shows the definition of the ring-puckering coordinate x , previously used to define the puckering motion in the related 14CHD molecule,³ and the corresponding ring-puckering angle τ . For the present work, the puckering angle τ is chosen as the better coordinate for defining this large amplitude motion.

In order to calculate the ring-puckering potential energy function, first the kinetic energy dependence on the coordinate needed to be calculated. The planar structures of 14DHN for the S_0 and S_1 states were calculated using MP2/CC-PVTZ and CIS/6-311++G(d,p) levels of theory, respectively. These calculated structures are illustrated in Figure 37. Comparison of the two structures shows that the C-C bond lengths of the benzene ring of the S_1 state increases due to the excitation of an electron from the π to π^* molecular orbital. The program previously described for tetralin⁸⁰ was used for the kinetic energy calculation. This was accomplished by placing the two hydrogen atoms of the tetralin CH_2 groups at the carbons atoms across from the benzene ring into the plane of the full molecule and assuming each to have one-half the mass of a hydrogen atom so that the =C-H atom motions could be reproduced. The kinetic energy expansions calculated for the S_0 and S_1 states are

$$S_0: g_{44}(\tau) = 0.0410615 - 0.0030281\tau^2 - 0.00726122\tau^4 + 0.00535904\tau^6 \quad (8.1)$$

$$S_1: g_{44}(\tau) = 0.0406933 - 0.0033311\tau^2 - 0.00674431\tau^4 + 0.00505166\tau^6 \quad (8.2)$$

where g_{44} is the reciprocal reduced mass for the puckering in terms of the puckering angle τ . Using these functions, the potential energy functions for the two states were calculated to be

$$S_0: V(\text{cm}^{-1}) = 2.58 \times 10^2 \tau^2 + 1.31 \times 10^3 \tau^4 \quad (8.3)$$

$$S_1: V(\text{cm}^{-1}) = 2.10 \times 10^3 \tau^2 + 1.96 \times 10^3 \tau^4 \quad (8.4)$$

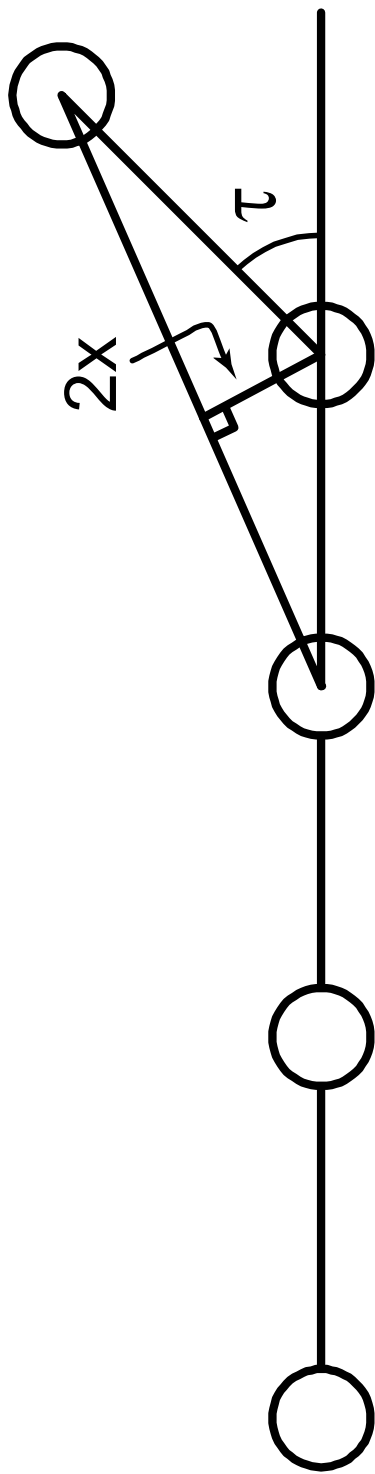


Figure 36. Definition of the ring-puckering coordinate x and the ring-puckering angle τ . The benzene ring is on the left.

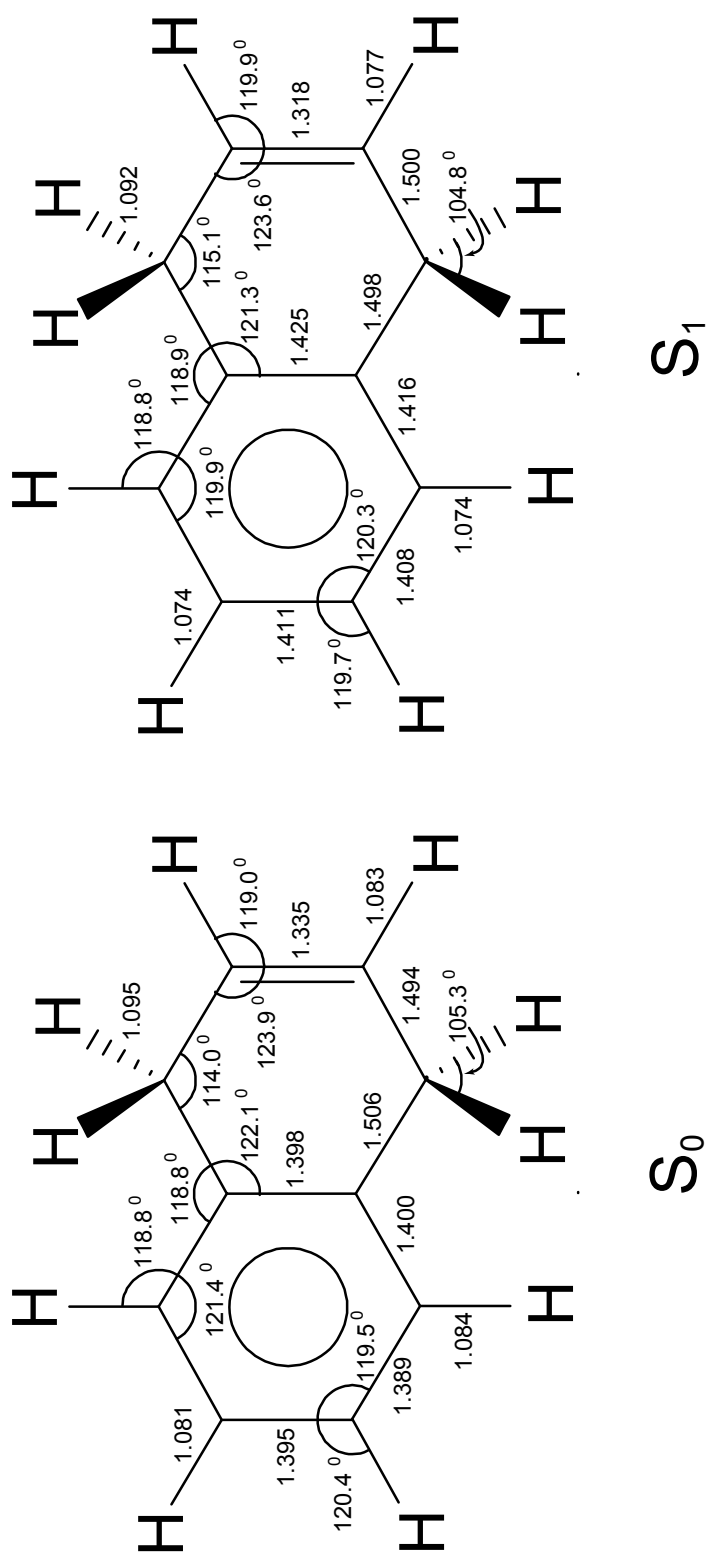


Figure 37. Calculated structures of 14DHN in its ground (S_0) and $S_1(\pi, \pi^*)$ electronic states.

The calculations were carried out as previously described.⁷³⁻⁷⁹ Table 19 compares the observed and calculated energy separations for both of these electronic states and Figure 38 shows the potential energy functions along with the quantum levels for both states. As is obvious, the energy minima correspond to puckering angles of $\tau = 0^\circ$ and the molecule has a planar equilibrium structure. However, the puckering motion is very floppy so that the molecular amplitudes reach $\pm 30^\circ$ of puckering even at relatively low energies. As is evident from Eqs. (8.3) and (8.4) and from the energy separations between the quantum states in Figure 38, the 14DHN potential function for the S_0 state is dominated by the quartic term whereas for S_1 it becomes more nearly harmonic. The quartic contribution typically arises from angle strain contributions. The potential energy functions in Figure 38 clearly show that the molecule becomes more rigid and stiffer in its electronic excited state. This is shown directly in Figure 39 where the two potential energy curves are compared to each other and also to 1,4-cyclohexadiene (14CHD). This figure demonstrates that the bicyclic 14DHN is much floppier than the 14CHD. The latter molecule possesses two full carbon-carbon double bonds while the 14DHN has, across from its double bond, a bond with the benzene ring of bond order 1.5. Thus, this change in angle strain likely is the cause of reducing the rigidity of the non-aromatic ring. In the S_1 state, however, the 14DHN becomes more rigid, and is in fact stiffer than the 14CHD molecule in its ground state. This is similar to what was observed for the bicyclic molecule coumaran⁷⁸ which has a five-membered ring containing an oxygen atom next to the benzene ring. For coumaran the molecule has a barrier to planarity of 154 cm^{-1} in the ground state, but in the $S_1(\pi, \pi^*)$ state the five-membered ring becomes more rigid and the barrier drops to 34 cm^{-1} .

Table 19: Observed and calculated^a ring-puckering transitions (in cm^{-1}) of 14DHN in its S_0 ground and $S_1(\pi, \pi^*)$ excited states

	Transition	Observed	Calculated	Δ	CDL ^b
S_0	$0 \rightarrow 1$	33.8	33.6	0.2	31.2
	$1 \rightarrow 2$	38.4	38.7	-0.3	40.5
	$2 \rightarrow 3$	42.2	42.4	-0.2	39.5
	$3 \rightarrow 4$	45.7	45.4	0.3	40.4
S_1	$0 \rightarrow 1$	77.4	77.7	-0.3	72
	$1 \rightarrow 2$	79.8	79.4	0.4	78
	$2 \rightarrow 3$	81.2	81.1	0.1	82
	$3 \rightarrow 4$	82.4	82.6	-0.2	91

^a $V(S_0) = 2.58 \times 10^2 \tau^2 + 1.31 \times 10^3 \tau^4$, $V(S_1) = 2.10 \times 10^3 \tau^2 + 1.96 \times 10^3 \tau^4$

^b Ref. 33, calculated energy separations

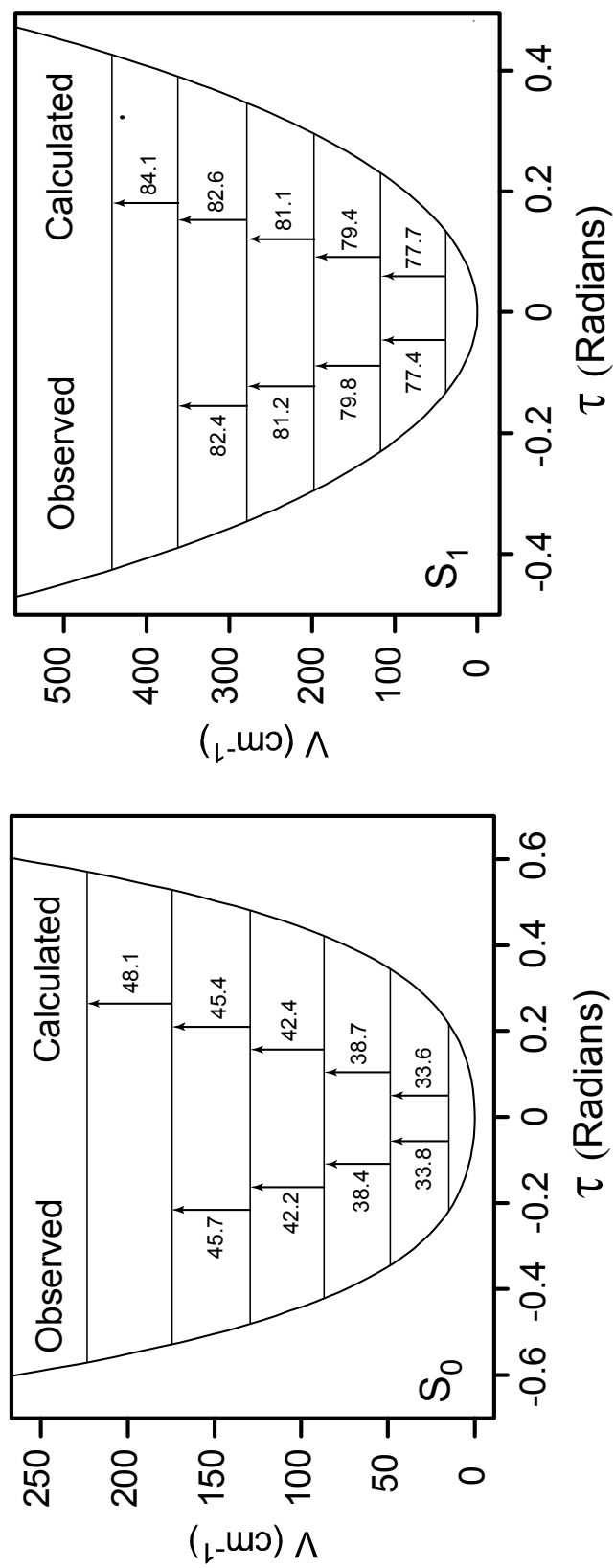


Figure 38. Ring-puckering potential functions for 14DHN in its ground (left) and $S_1(\pi, \pi^*)$ excited (right) states.

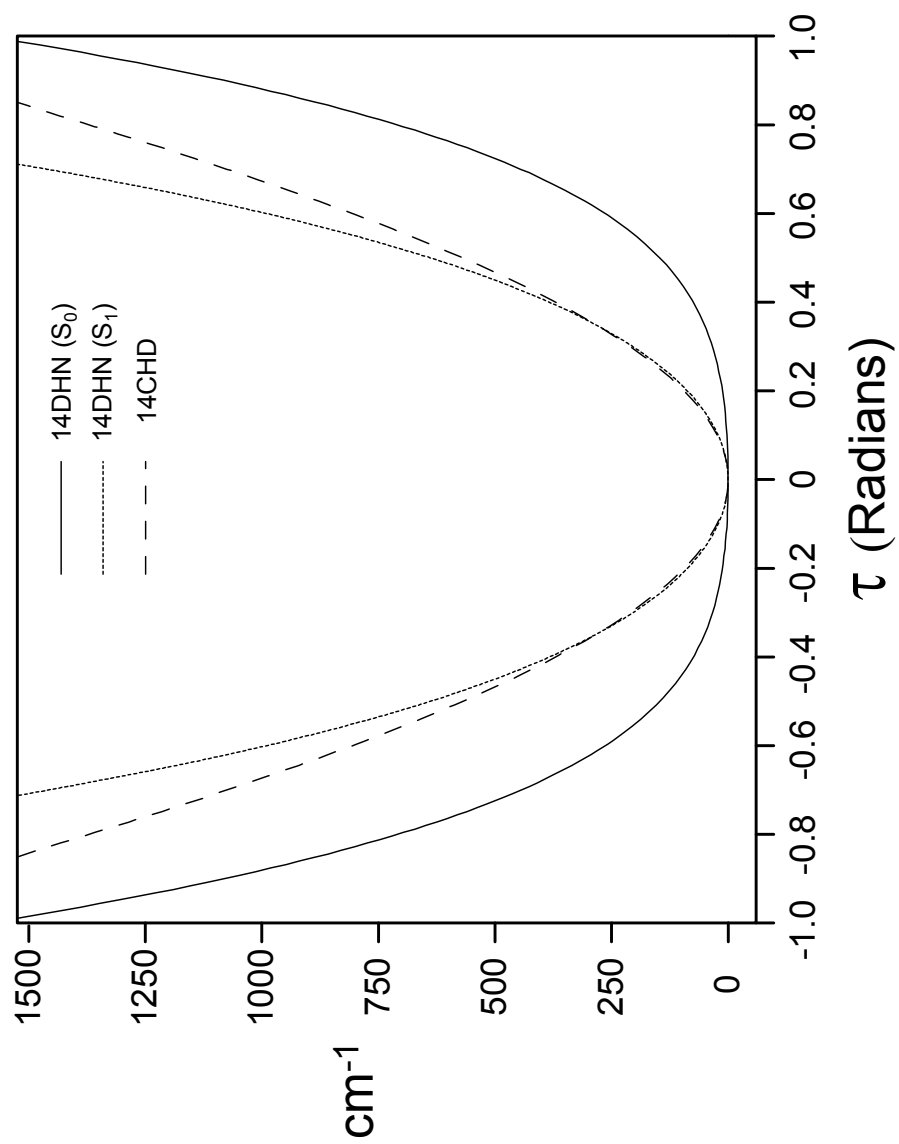


Figure 39. Comparison of the 14DHN S_0 and S_1 potential energy functions with the 1,4-cyclohexadiene (14CHD) function.

CONCLUSIONS

The FES, SVLF, and especially the ultraviolet absorption spectra have been used to determine the ring-puckering potential functions for 14DHN in its S_0 and $S_1(\pi,\pi^*)$ states. The molecule is planar in both states but becomes considerably more rigid in the electronic excited state. Chakraborty et al.³³ previously analyzed their FES and SVLF spectra and proposed a barrier of 0.5 kcal/mole ($\sim 175 \text{ cm}^{-1}$) for the ground state and also a small barrier for the excited state. However, as shown in Table 18, their lack of frequency accuracy which was obtained from the UV absorption spectra in this work, led them to believe that they had an irregular series of energy spacings whereas they are in fact quite regular. Discussion on this molecule will continue in the next chapter which presents the spectral and theoretical investigation of 14DHN in detail in order to understand the changes of frequencies of vibrational modes between the ground and excited states and also to analyze the coupling of ring-puckering with the other vibrational modes.

CHAPTER IX

VIBRATIONAL ASSIGNMENTS OF 1,4-DIHYDRONAPHTHALENE IN ITS GROUND AND $S_1(\pi,\pi^*)$ STATES

INTRODUCTION

As discussed in Chapter VIII the spectroscopic investigation of 1,4-dihydronaphthalene (14DHN) utilizing ultraviolet (UV) and laser induced fluorescence (LIF) made it possible to determine the ring-puckering potential energy function of this molecule in its ground and excited $S_1(\pi,\pi^*)$ electronic states. The structure of 14DHN was found to be planar in states, and the study revealed that the partially saturated ring becomes more rigid in the excited state. However, Chapter VIII presented only that portion of the UV and LIF spectra which was necessary to determine the levels of the low-frequency vibrational modes (ν_{54} , ν_{28} , and ν_{53}). 14DHN has 54 vibrational normal modes and analyzing these as possible is important for understanding the full structural features of the molecule. This chapter will therefore present a more complete discussion of the UV and LIF spectra together with infrared and Raman spectra which are necessary for a complete vibrational assignment of 14DHN for both the S_0 ground and the singlet $S_1(\pi,\pi^*)$ singlet excited electronic states. In addition to this, high level *ab initio* and density functional theory calculations were also carried out to facilitate these assignments.

EXPERIMENTAL

The experimental procedures for the acquisition of LIF and UV spectra have been described in the previous chapter. The Raman spectra of 14DHN were acquired on an SA Jobin-Yvon U-1000 spectrometer equipped with a liquid-nitrogen cooled CCD (charge couple device) detector. Raman scattering was achieved using the Coherent Radiation Innova 20 argon ion laser with an excitation at 514.5 nm. The liquid-phase spectra were recorded at room temperature with a lasing power of 0.6 W. Vapor-phase Raman spectra were collected in the previously described vapor Raman cell at a

temperature of 300⁰ C.³⁵ A laser power of 5 W was used for this purpose. The liquid mid-infrared spectra were collected on the Bruker Vertex 70 FT-IR spectrometer and a thin capillary film of the pure sample between two KBr discs was used. A total of 256 scans with a resolution of 1 cm⁻¹ were recorded.

COMPUTATIONS

All of the computations were done using the Gaussian 03 quantum mechanical package.⁴⁵ The vibrational frequencies, infrared and Raman intensities, and depolarization ratios of 14DHN in its S₀ state were calculated using the B3LYP/6-311++G(d,p) level of theory. Calculated frequencies were scaled by a factor of 0.964 for values over 1800 cm⁻¹ and a factor of 0.985 for those below 1800 cm⁻¹, as from previous work.⁵⁰⁻⁵³ The S₁(π,π^*) state calculations were done at the CIS/6-311++G(d,p) level of theory again for the planar C_{2v} structure. The scaling factor was 0.895 which had also been used for 12DHN.⁶⁷ The CIS (or configuration interaction-singles) is an inexpensive *ab initio* method which can be applied for excited electronic state calculations. It is comparable to the Hartree-Fock method used for the ground state and therefore does not take the electron correlation effects fully into account. More rigorous computational methods such as time-dependent density functional theory and CIS(D) (or CIS with second-order correction) were also carried out to determine the excited state structure and vibrational frequencies. However, all of these methods failed to calculate the minimum energy structure. Nevertheless, CIS calculations have provided fairly reasonable results and this will be noted later.

Although this work reports the frequencies calculated only for the planar structure (C_{2v}) of 14DHN, computations were also done for C_s (bent) and C₁ (structure with no symmetry) point groups as well. The calculated values for the C_s and C₁ structures were very much similar to those of the C_{2v} structure and therefore are not presented here. The approximate descriptions of the vibrational normal modes were determined by the GaussView 3.0 molecular visualization program.⁶³

RESULTS AND DISCUSSION

Infrared and Raman spectra

The potential energy functions of 14DHN showed that this molecule has a planar structure with C_{2v} symmetry in both the ground and $S_1(\pi,\pi^*)$ electronic states. Therefore the distribution of the 54 vibrational modes of 14DHN can be expressed as

$$18A_1 + 10A_2 + 17B_1 + 9B_2 \quad (9.1)$$

This classification is very useful in assigning the spectral data as the vibrational and electronic transitions are governed by selection rules which are based on the symmetry of the molecule. For example vibrational modes with A_2 symmetry are infrared forbidden and should not actually be seen in an infrared spectrum. The importance of this classification will be emphasized further later in this chapter. Figures 40 and 41 compare the infrared and Raman spectra of 14DHN to the computed scaled spectra using the DFT-B3LYP/6-311++G(d,p) level of calculation. Table 20 lists the values of the experimental and calculated vibrational frequencies and their relative intensities sorted by their symmetry. Although most of the predicted bands by theoretical calculations can be observed in the experimental spectra, there are still a number of bands whose frequencies and intensities do not agree with the computed ones. However, close analysis revealed that these unassigned peaks belong to those of 1,2-dihydronaphthalene (12DHN), an isomer of 14DHN, whose vibrational spectra have previously been assigned.⁶⁷ The most intense peaks of 12DHN reported previously are at 782 and 1224 cm^{-1} in the infrared and Raman spectra respectively, can be clearly observed in the spectra illustrated here also. The matching of frequencies and intensities of other impurity peaks very well with the reported bands of 12DHN confirms that the main impurity present with 14DHN is 12DHN. This information is useful as no information about the impurities present in the commercial 14DHN were provided by the manufacturer or by anyone who used the same source of sample before.³³ Figure 40

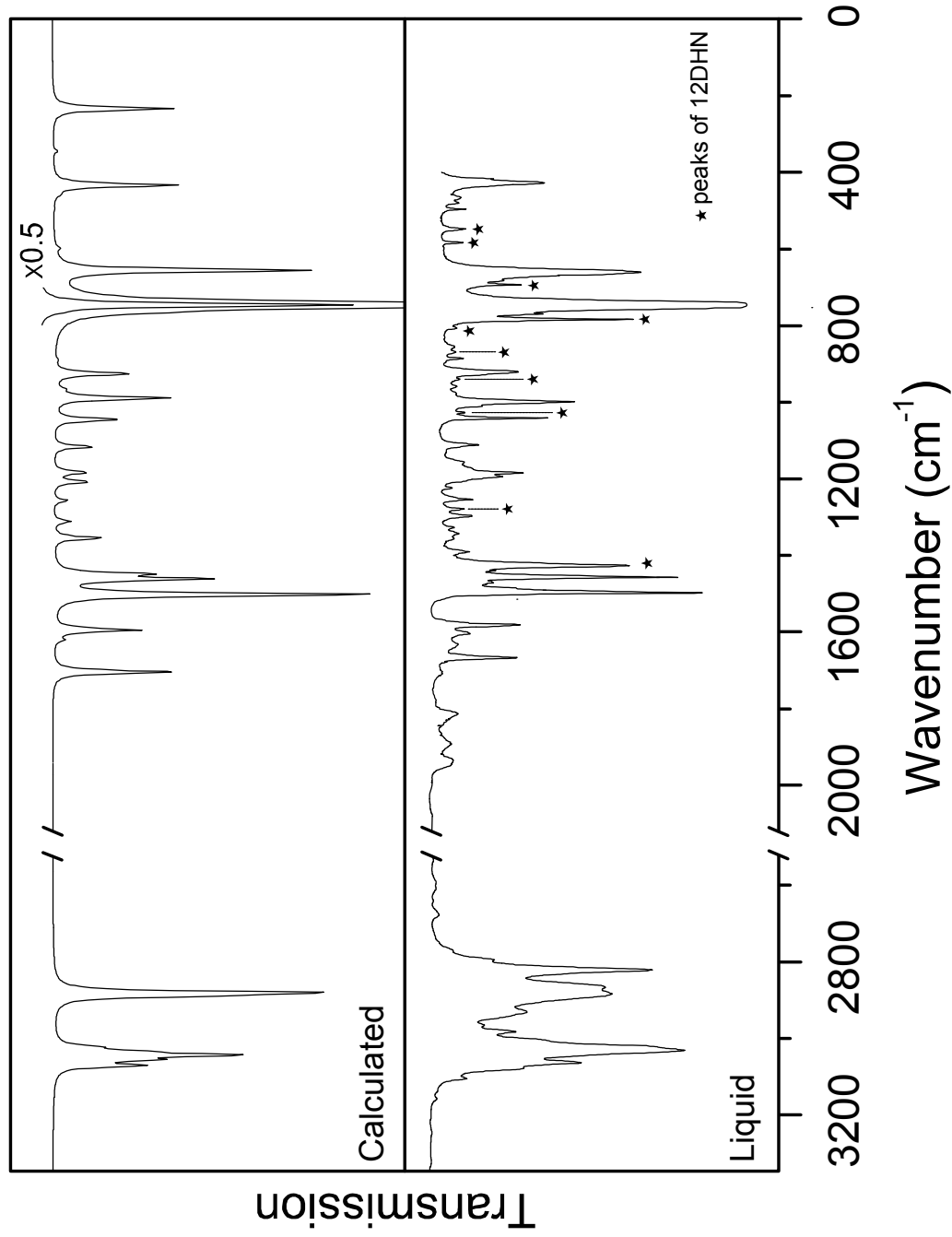


Figure 40. Liquid-phase infrared spectra of 14DHN compared to its calculated DFT spectrum.

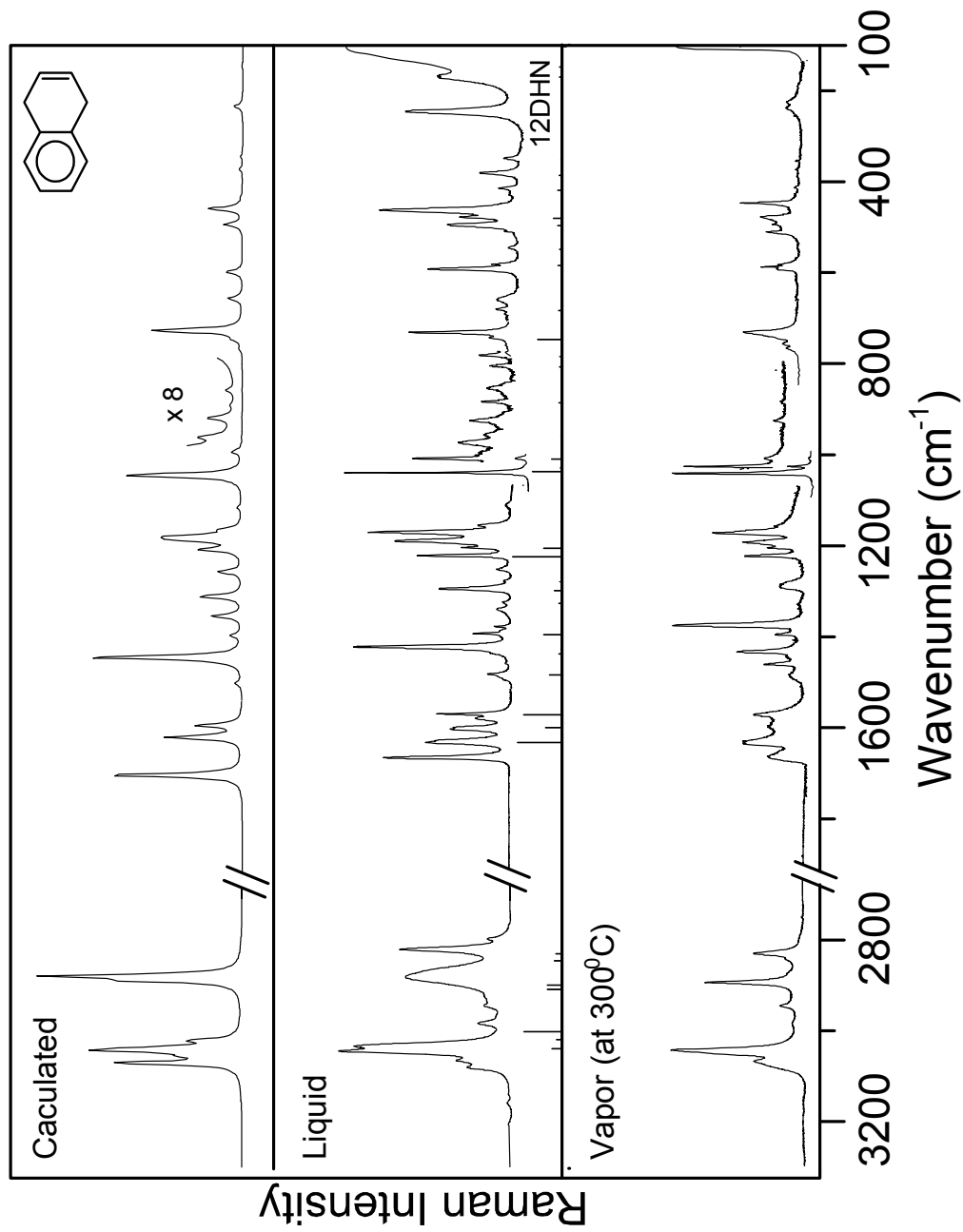


Figure 41. Liquid and vapor-phase Raman spectra of 14DHN compared to its calculated DFT spectrum. The liquid-phase Raman spectrum of 12DHN is also shown for comparison as vertical bars.

Table 20: Vibrational assignment (in cm^{-1}) of 1,4-dihydronaphthalene^a

Sym.	C_{2v}	ν	Approx. Description	IR		Raman		FES ^b	Calculated	
				Liquid	Liquid ^c	Vapor ^d	S_0^e		$S_1(\pi, \pi^*)^f$	
A ₁	1	Benzene C-H stretch	3077 sh	3080 (89, 0.26)	3067 (372)	-----	3071 (241, 656)	3015		
	2	=C-H stretch	-----	3045 (329, 0.10)	3042 (898)	-----	3044 (498, 635)	2994		
	3	Benzene C-H stretch	-----	(3045)	(3042)	-----	3037 (9, 358)	2973		
	4	CH ₂ stretch	-----	(2882)	2893 (695)	-----	2880 (18, 1000)	2785		
	5	C=C stretch	1667 ms	1668 (176, 0.05)	1663 (85)	-----	1705 (87, 879)	1674		
	6	Benzene C-C stretch	1581 ms	1572 (18, 0.25)	1571 (30)	-----	1595 (62, 295)	1625		
	7	Benzene C-H ip wag	1497 vs	1497 sh	-----	-----	1504 (223, 41)	1518		
	8	CH ₂ deform	-----	1425 (190, 0.33)	1433 (123)	-----	1447 (0.05, 1000)	1417		
	9	CH ₂ wag	1342 w	1342 (10, 0.54)	-----	1400 ms	1356 (32, 104)	1396		
	10	Benzene C-C stretch	1297 m	1298 (69, 0.16)	1288 (54)	1337 ms	1313 (12, 277)	1336		
	11	Benzene C-C stretch	-----	-----	-----	1167 vs	1188 (4, 368)	1153		
	12	=C-H wag	1173 sh	1172 (137, 0.20)	1172 (159)	1149 m	1181 (1, 396)	1142		
	13	Benzene C-H ip wag	1156 w	1157 (34, 0.56)	1156 (38)	1130 m	1166 (0.1, 107)	1129		
	14	Benzene C-C stretch	1041 s	1042 (1000, 0.06)	1041 (1000)	951 vs	1047 (47, 808)	960		
A ₂	15	Sat. ring C-C stretch	-----	-----	-----	873 w	919 (1, 7)	878		
	16	Sat. ring C-C stretch	(746)	734 (451, 0.08)	730 (377)	689 vs	728 (4, 601)	669		
	17	Ring angle bend	-----	596 (51, 0.15)	586 (107)	459 ms	599 (3, 107)	517		
	18	Ring angle bend	-----	-----	446 (149)	449 s	460 (3, 225)	434		
	19	CH ₂ stretch	-----	(2882)	(2893)	-----	2890 (0, 471)	2789		
	20	CH ₂ twist	-----	-----	-----	-----	1213 (0, 11)	1163		
	21	=C-H out-of-plane wag	976 sh	976 (9, 0.73)	-----	-----	995 (0, 63)	996		
	22	Benzene C-H oop wag	-----	-----	-----	-----	974 (0, 0.4)	904		
	23	CH ₂ rock	-----	958 (1, 0.49)	-----	-----	961 (0, 6)	813		

Table 20: (Continued)^a

Sym.	C_{2v}	ν	Approx. Description	IR		Raman		FES ^b		Calculated	
				Liquid	Liquid ^c	Vapor ^d	FES ^b	S_0^e	$S_1(\pi, \pi)^{*,f}$		
A ₂	24	Benzene C-H oop wag	855 w	856 (6, 0.64)	-----	-----	-----	859 (0, 2)	630		
	25	Benzene ring twist	-----	703 (1, 0.00)	-----	-----	-----	708 (0, 0.03)	447		
	26	Benzene ring twist	-----	513 (7, 0.27)	510 (74)	-----	-----	499 (0, 0.1)	360		
	27	C=C twist	-----	384 (16, 0.67)	373 (10)	310 mw	-----	373 (0, 22)	288		
	28	Ring twist at the bridge	-----	-----	-----	(92)	-----	146 (0, 3)	70		
B ₁	29	Benzene C-H stretch	3064 ms	3065 (114, 0.30)	3073 sh	-----	-----	3056 (234, 185)	3004		
	30	Benzene C-H stretch	3031 vs	3034 (305, 0.19)	(3042)	-----	-----	3034 (169, 12)	2988		
	31	=C-H stretch	(3031)	(3034)	(3042)	-----	-----	3022 (97, 226)	2950		
	32	CH ₂ stretch	2884 ms	2882 (181, 0.17)	2874 sh	-----	-----	2881 (732, 23)	2779		
	33	Benzene C-C stretch	1603 m	1605 (100, 0.62)	-----	-----	-----	1621 (6, 512)	1415		
	34	Benzene C-C stretch	1456 s	1462 (4, 0.25)	1460 (66)	-----	-----	1463 (102, 8)	1406		
	35	CH ₂ deform	1426 s	-----	-----	-----	-----	1449 (58, 21)	1375		
	36	=C-H in-plane wag	1389 mw	1381 (25, 0.15)	1375 (267)	-----	-----	1398 (0.01, 69)	1369		
	37	CH ₂ wag	1355 w	-----	-----	-----	-----	1356 (2, 97)	1320		
	38	Benzene C-H ip wag	1254 m	1255 (15, 0.67)	-----	-----	-----	1258 (10, 156)	1145		
	39	Sat. ring C-C stretch	1184 ms	-----	-----	-----	-----	1184 (20, 4)	1112		
	40	Benzene C-H ip wag	1111 ms	1112 (7, 0.70)	-----	-----	-----	1118 (27, 29)	1036		
	41	Sat. ring C-C stretch	998 s	-----	-----	967 ms	-----	990 (82, 8)	947		
	42	Ring angle bend	885 m	-----	-----	867 w	-----	891 (2, 1)	851		
	43	Ring angle bend	769 m	762 (11, 0.08)	765 (74)	-----	-----	769 (25, 14)	707		
	44	Ring angle bend	496 m	498 (23, 0.68)	493 (28)	439 m	-----	495 (0.4, 124)	424		
	45	Ring angle bend	-----	351 (6, 0.65)	354 (11)	328 m	-----	346 (3, 13)	312		

Table 20: (Continued)^a

Sym.	C_{2v}	ν	Approx. Description	IR		Raman		FES ^b	Calculated	
				Liquid	Vapor ^d	Liquid ^c	Vapor ^d		S_0^e	$S_1(\pi,\pi)^f$
B_2	46	CH_2 stretch	(2884)	(2874)	(2882)	(2874)	-----	2889 (337, 17)	2788	
	47	CH_2 wag	1193 mw	1192 (100)	1192 (98, 0.1)	1192 (100)	-----	1209 (24, 261)	1163	
	48	Benzene C-H oop wag	959 w	-----	-----	-----	-----	967 (5, 0.5)	910	
	49	CH_2 rock	920 ms	-----	-----	925 (19)	-----	927 (53, 0.02)	711	
	50	Benzene C-H oop wag	746 vs	-----	746 (17, 0.15)	-----	-----	747 (1000, 42)	653	
	51	=C-H out-of-plane wag	660 vs	-----	661 (9, 0.61)	661 (8)	-----	657 (178, 97)	593	
	52	Benzene ring oop vibration	427 ms	-----	430 (1, 0.68)	-----	298 ms	435 (89, 7)	261	
	53	Sat. ring flapping	-----	-----	248 (59, 0.64)	231 (46)	(115)	235 (85, 59)	90	
	54	Sat. ring puckering	-----	-----	-----	-----	79 vw	36 (8, 10)	72	

^a s-strong, m-medium, w-weak, v-very, sh-shoulder, ip-in-phase, oop-out-of-phase.

^b The values in the parentheses are approximate expected values.

^c The relative Raman intensities and the depolarization ratios are shown in the parentheses.

^d The relative Raman intensities are shown in the parentheses.

^e Calculated using B3LYP/6-311++G(d,p) level of theory. The relative infrared and Raman intensities are shown in the parentheses. The original calculated values were scaled by a factor of 0.985 for frequencies below 2000 cm^{-1} and by a factor of 0.964 cm^{-1} for those above 2000 cm^{-1} .

^f Calculated using CIS/6-311++G(d,p) level of theory. The scaling factor used was 0.895.

highlights the most intense impurity 12DHN bands present in the liquid infrared spectra of 14DHN and Figure 41 shows a line spectrum derived from the reported original liquid Raman spectrum of 12DHN. These illustrations make the comparison of calculated and experimental spectra of 14DHN easier. The agreement between the calculated and experimental data for 14DHN is very good and it demonstrates that computations are very useful in assigning the observed frequencies to the correct vibrational mode. The experimental depolarization ratios (ρ values) of the liquid Raman spectra are also listed in Table 20 together with their relative intensities. These values were calculated by taking the ratio of intensities of each band measured at perpendicular and parallel polarization. Most of the vibrational modes which are totally symmetric with A_1 symmetry have very low ρ values (i.e. polarized) while many of the other modes which are non-totally symmetric (with A_2 , B_1 and B_2 symmetries) have higher ρ values, some closer to 0.75 (i.e. depolarized). However for a more accurate determination of ρ values, a calibration of detector response (i.e. determination of absolute intensities) at all the wavelengths is required and the ρ values obtained after such a calibration would be more reliable. Nevertheless, the depolarization ratios listed in Table 20 are still indications of the correct vibrational assignments. The calculated frequencies of the $S_1(\pi, \pi^*)$ electronic states using the CIS/6-311++G(d,p) level of theory are also listed in Table 20 along with some of the experimental values of the FES spectra. The comparison of calculated and observed frequencies of the excited state will be presented later in this chapter.

FES spectra

This section presents a more complete assignment of FES spectra than what was done in the previous chapter. Figure 42 shows the FES spectrum of 14DHN with respect to the 0_0^0 origin which also includes some major assignments. Table 21 lists the wavenumbers of the bands and the corresponding values observed in the UV spectra together with the calculated frequencies using the CIS/6-311++G(d,p) level

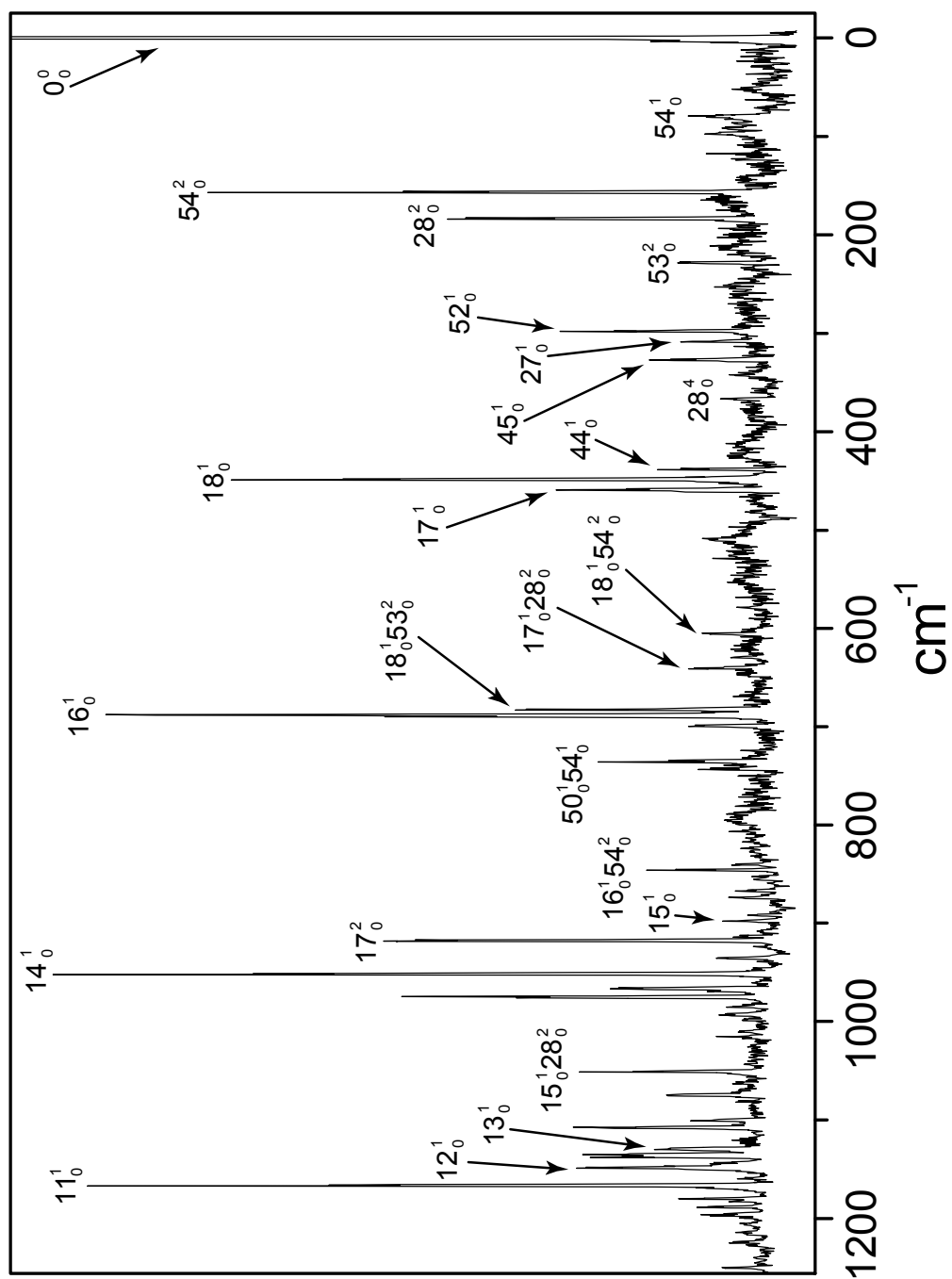


Figure 42. FES spectrum of I4DHN with some assignments.

Table 21: FES spectrum of 14DHN compared to some selected UV bands

FES	UV	Assignment (Sym.)	Calculated ^a	Inferred ^b
79 vw	77.2 m	54_0^1 (B ₂)	72	
157 s	157.2 ms	54_0^2 (A ₁)		
184 ms	182.2 w	28_0^2 (A ₁)		
229 m	228. 8 w	53_0^2 (A ₁)		
298 ms	299.2 w	52_0^1 (B ₂)?	261	
310 mw	-----	27_0^1 (A ₂)?	288	
328 m	327.1 vw	45_0^1 (B ₁)	312	
367 w	366.7 w	28_0^4 (A ₁)		
439 m	438.5 w	44_0^1 (B ₁)	424	
449 s	448.4 m	18_0^1 (A ₁)	434	
459 ms	461.0 mw	17_0^1 (A ₁)	517	
459 ms	461.0 mw	53_0^4 (A ₁)		2 × 229
606 w	606.9 vw	$18_0^1 54_0^2$ (A ₁)		449 + 157
630 vw	630.7 w	$18_0^1 28_0^2$ (A ₁)		449 + 184
640 w	639.5 vw	$17_0^1 28_0^2$ (A ₁)		459 + 184
682 ms	681.8 ms	$18_0^1 53_0^2$ (A ₁)		449 + 229
689 vs	687.6 m	16_0^1 (A ₁)	669	
699 m	698.5 vw	?		
735 m	732.4 ms	$50_0^1 54_0^1$ (A ₁)?		(653) + 79
846 m	846.0 w	$16_0^1 54_0^2$ (A ₁)		689 + 157
867 w	866.7 mw	42_0^1 (B ₁)	851	
873 w	874 .4 vw	15_0^1 (A ₁)	878	
873 w	874 .4 vw	$16_0^1 28_0^2$ (A ₁)		689 + 184
897 mw	895.5 w	18_0^2 (A ₁)		2 × 449
918 s	917.4 ms	17_0^2 (A ₁)		2 × 459
918 s	917.4 ms	$16_0^1 53_0^2$ (A ₁)		689 + 229
935 m	935.5 mw	?		
951 vs	951.2 vs	14_0^1 (A ₁)	960	
967 ms	967.1 mw	41_0^1 (B ₁)	947	

Table 21: (Continued)

FES	UV	Assignment (Sym.)	Calculated ^a	Inferred ^b
975 s	975.1 mw	?		
1051 ms	1050.9 mw	$15_0^1 28_0^2 (A_1)$		873 + 184
1075 m	1074.3 mw	$17_0^2 54_0^2 (A_1)$		918 + 157
1100 w	1100.5 vw	$15_0^1 53_0^2 (A_1)$		873 + 229
1108 m	1108.4 ms	$14_0^1 54_0^2 (A_1)$		951 + 157
1130 m	1131.9 mw	$13_0^1 (A_1)$	1129	
1135 m	1134.0 w	$14_0^1 28_0^2 (A_1)$		951 + 184
1149 m	1147.3 m	$12_0^1 (A_1)$	1142	
1167 vs	1166.2 ms	$11_0^1 (A_1)$	1153	
1180 w	1179.8 w	$14_0^1 53_0^2 (A_1)$		951 + 229
1323 m	1322.2 w	$11_0^1 54_0^2 (A_1)$		1167 + 157
1337 ms	1335.7 mw	$10_0^1 (A_1)$	1336	
1341 ms	1340.7 w	$18_0^3 (A_1)$		3 × 449
1350 m	1350.0 vw	$11_0^1 28_0^2 (A_1)$		1167 + 184
1355 m	1355.0 vw	$13_0^1 53_0^2 (A_1)$		1130 + 229
1373 m	-----	$17_0^3 (A_1)$		3 × 459
1376 mw	-----	$16_0^2 (A_1)$		2 × 689
1395 vw	-----	$11_0^1 53_0^2 (A_1)$		1167 + 229
1400 ms	-----	$9_0^1 (A_1)$	1396	

^a Calculated using CIS/6-311++G(d,p) level of theory.

^b Inferred from the already assigned fundamental values or from the calculated values.

of theory. Most of the observed bands listed in Table 21 are of the energy levels with A_1 symmetry in the S_1 state. This is very clear since FES transitions originate from the ground vibrational level of the S_0 state which has an A_1 symmetry and therefore expect to end up at vibronic levels also with A_1 symmetry. This enabled us to assign many of the A_1 fundamental levels in the S_1 state (e.g. ν_{18} , ν_{17} , ν_{16} etc.) whose observed values agree very well with those of the calculated ones. The validity of such assignments are emphasized further by the observation of bands corresponding to the combinations of these fundamental A_1 modes with the overtones of the lowest three vibrational modes, e.g. $18_0^1 54_0^2$, $15_0^1 53_0^2$, $14_0^1 28_0^2$ etc. which are also totally symmetric. There are only a few assignments which have symmetries other than A_1 . Most of these are relatively weak compared to the totally symmetric vibrations. Table 21 also reports some of the UV bands which match with the corresponding FES bands. All of these must be “cold bands” originating from the ground vibration level of the S_0 state, which were assigned with the aid of FES spectra. However, UV transitions can originate from higher vibrational levels as well and therefore can provide information on both the S_0 and S_1 states. Therefore other transitions observed in the UV spectra will be presented later.

SVLF spectra

SVLF or dispersed fluorescence spectra can also be used to determine the vibrational levels of the S_0 state. The advantage of utilizing SVLF is that it can also elucidate the higher vibrational quantum states ($v = 2, 3, 4, \dots$). Overtone bands can sometimes also observed by infrared and Raman spectra, but their intensities may be too weak. Therefore SVLF can confirm the fundamentals already observed in the infrared and Raman spectra and also determine many of the overtone and combination levels. Figure 43 shows the labeling scheme used for SVLF transitions. As explained in Chapter II the molecule can be excited to the ground vibrational or to an excited vibronic level of the S_1 using FES. The fluorescent radiation or dispersed fluorescence originating from this transition will have a series of wavenumbers. The dispersed fluorescence with

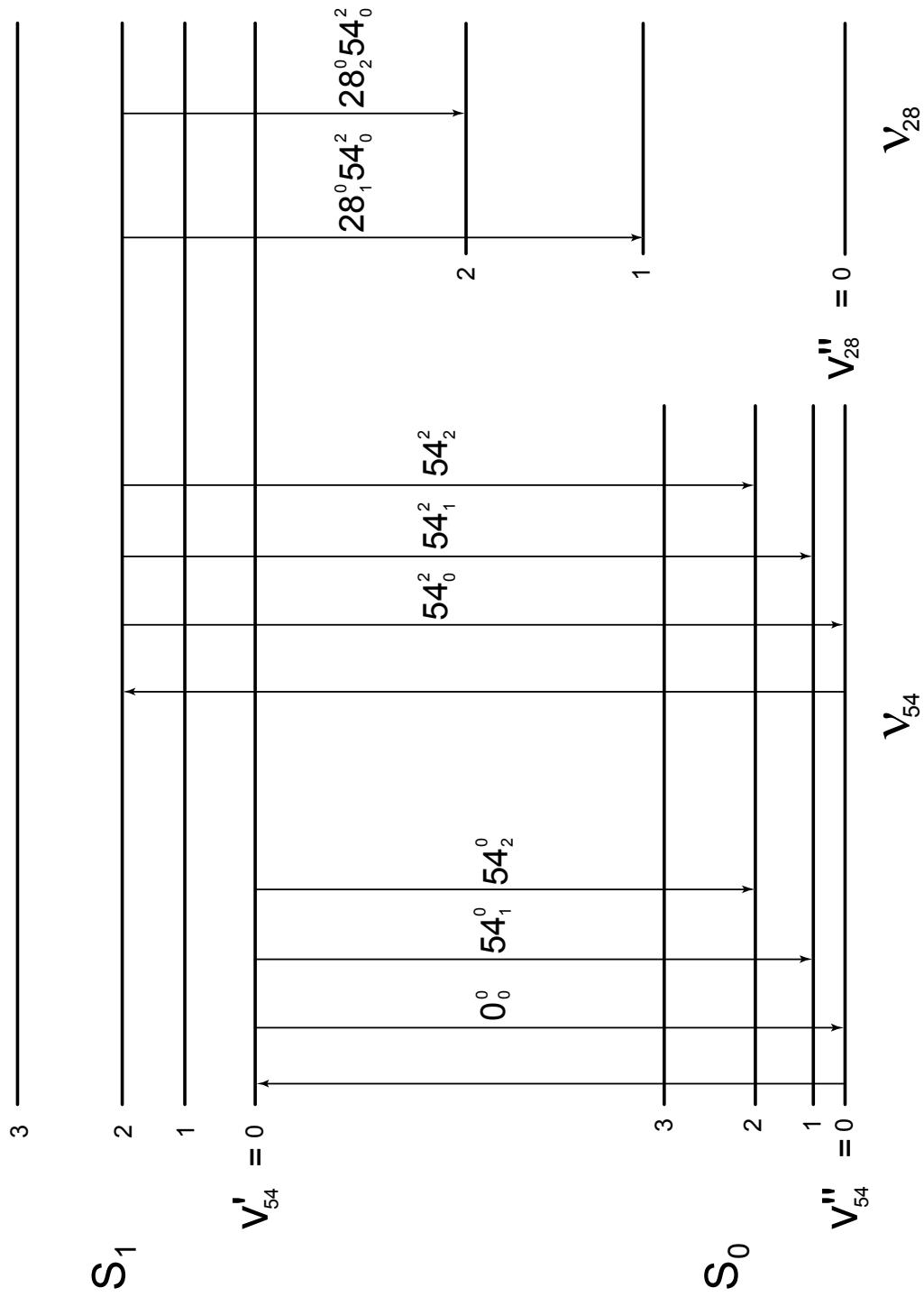


Figure 43. Labeling scheme for SVLF spectra acquired by different excitations.

the same wavenumber as that used for the excitation is the band origin. Figure 43 shows that the vibrational levels of the ground state can be determined by comparing wavenumbers of the transitions relative to the band origin.

The SVLF spectrum (from 0 to -1600 cm^{-1}) of 14DHN originating from the 0_0^0 excitation is illustrated in Figure 44. Analysis of the spectrum shows that the bands with totally symmetric transitions (i.e. $A_1 \rightarrow A_1$) are much more intense than those with non-totally symmetric transitions. Therefore, most of the vibrational modes with A_1 symmetry can be clearly seen here, and their frequency values agree very well with those reported in Table 20. Two A_1 modes (ν_{15} and ν_{11}) which were not detected in the infrared or Raman spectra were observed in SVLF and these match perfectly with the calculated frequencies. However, some non-totally symmetric transitions are also observed, and a notable one is the peak at -148 cm^{-1} . This is assigned to 28_1^0 which originated from a forbidden $A_1 \rightarrow A_2$ transition. This cannot be assigned to any other mode or combination. The calculated value of 148 cm^{-1} for ν_{28} also matches well with the observed frequency. The floppy nature of 14DHN ring in its ground electronic state may deform the ring from its planar structure and perturb the symmetries of some of its vibrational levels. Hence, some forbidden transitions may be partially allowed. However, the 28_0^1 transition, which is expected near 92 cm^{-1} in FES is not observed so clearly. Since the ring is much stiffer in the S_1 state, the transitions may be more restricted by the selection rules of the planar C_{2v} structure. This is even clearer when the FES and 0_0^0 SVLF spectra are compared where the latter shows many non-totally symmetric transitions while the former has very few.

Figure 45 shows the SVLF spectrum recorded from the 54_0^2 ($0_0^0 + 157\text{ cm}^{-1}$) excitation. Some assignments of this spectrum were already presented in the previous chapter but more detail is presented here. This spectrum has enabled us to determine many levels of the ring puckering mode (ν_{54}) of the S_0 state. This was very helpful for determining the potential energy function of 14DHN in the S_0 state.

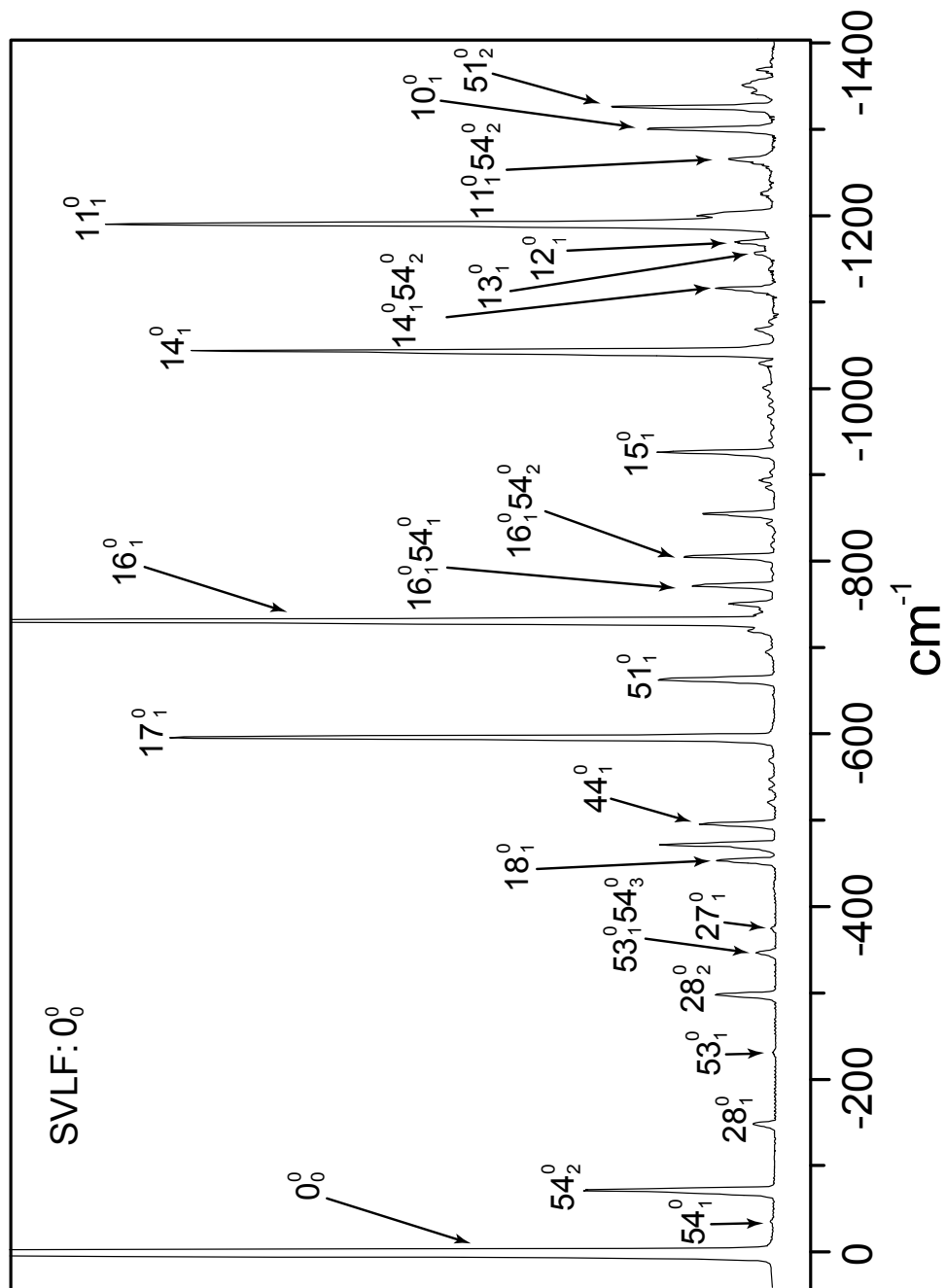


Figure 44. SVLF spectra of 14DHN from 0_0^0 excitation with some assignments.

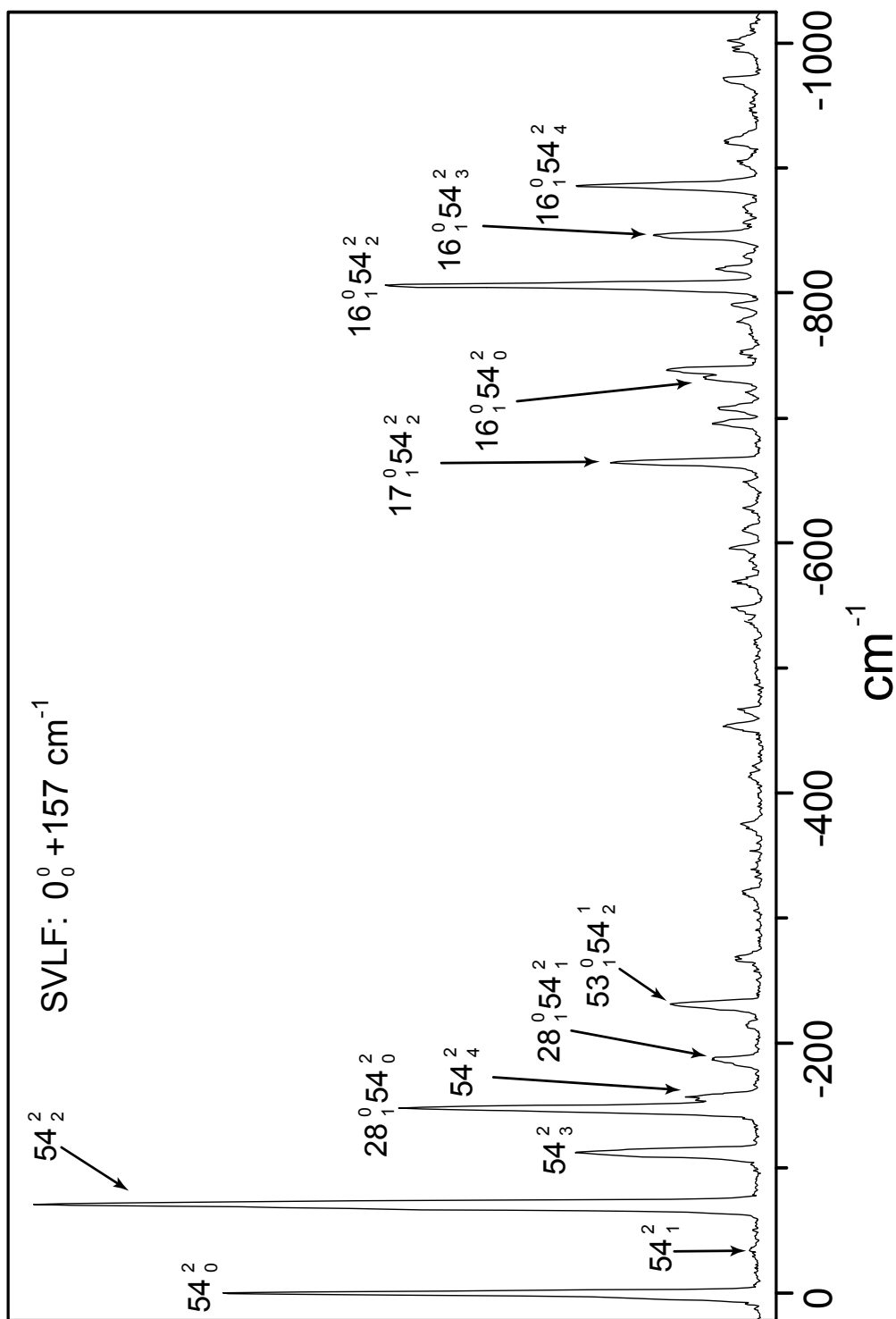


Figure 45. SVLF spectra of 14DHN from 54_0^2 excitation with some assignments.

Figure 46 and 47 depict two other SVLF spectra originating from the 28_0^2 ($0_0^0 + 184 \text{ cm}^{-1}$) and 53_0^2 ($0_0^0 + 229 \text{ cm}^{-1}$) excitations, respectively. These two provide somewhat less information than the previous SVLF spectra. However, the very intense band at -298 cm^{-1} in Figure 46 is clearly the 28_2^2 transition which confirms the assignment of 184 cm^{-1} to 28_0^2 in the FES spectra. The absence of 28_1^2 peak at -148 cm^{-1} peak is a little surprising which was observed in the SVLF of the previous two excitations. The 53_0^2 excitation also gives a weak band at -465 cm^{-1} which is assigned to 53_2^2 . The very strong peak at -268 cm^{-1} clearly belongs to the $53_1^2 54_1^0$ transition, a combination level of $\nu_{53} + \nu_{54}$. Table 22 lists the frequency values and their assignments of the SVLF spectra acquired by the four excitations discussed above. Nine of the eighteen A_1 vibrational modes (ν_{18} to ν_{10}) have been determined with certainty for the S_0 state and their frequencies match remarkably well with those reported in Table 20. In addition, some combinations of these modes with ν_{54} also have been observed confirming the accuracy of the assignments. Although the majority of the transitions are totally symmetric, there are a few observed bands with other symmetries. Some of these have considerable intensities (e.g. ν_{44} and ν_{51}). This again verifies our explanation that the molecule is flexible in the S_0 state with very loose C_{2v} symmetry, and hence some forbidden transitions for a planar structure can be allowed to a certain extent.

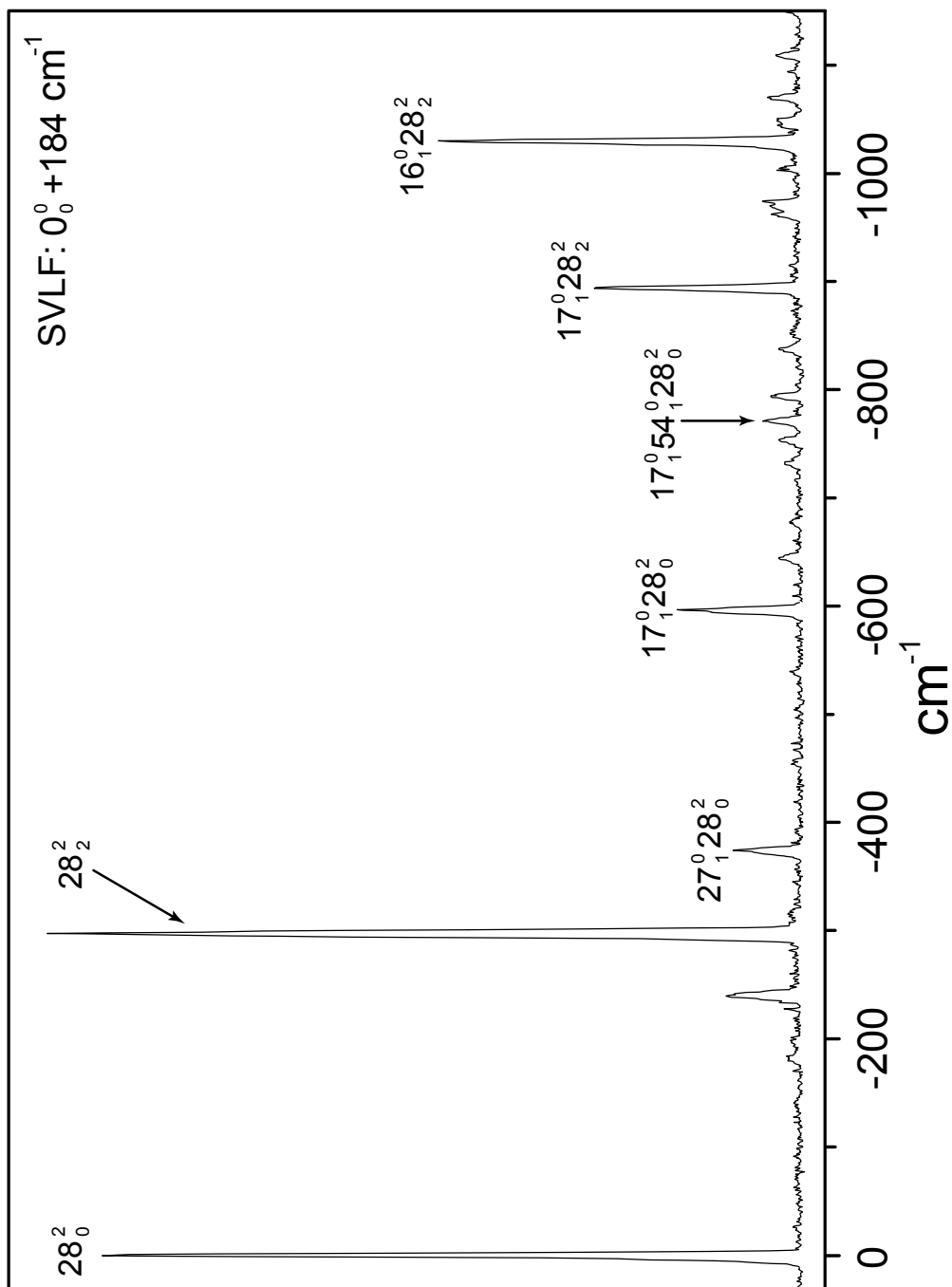


Figure 46. SVLF spectra of 14DHN from 28_0^2 excitation with some assignments.

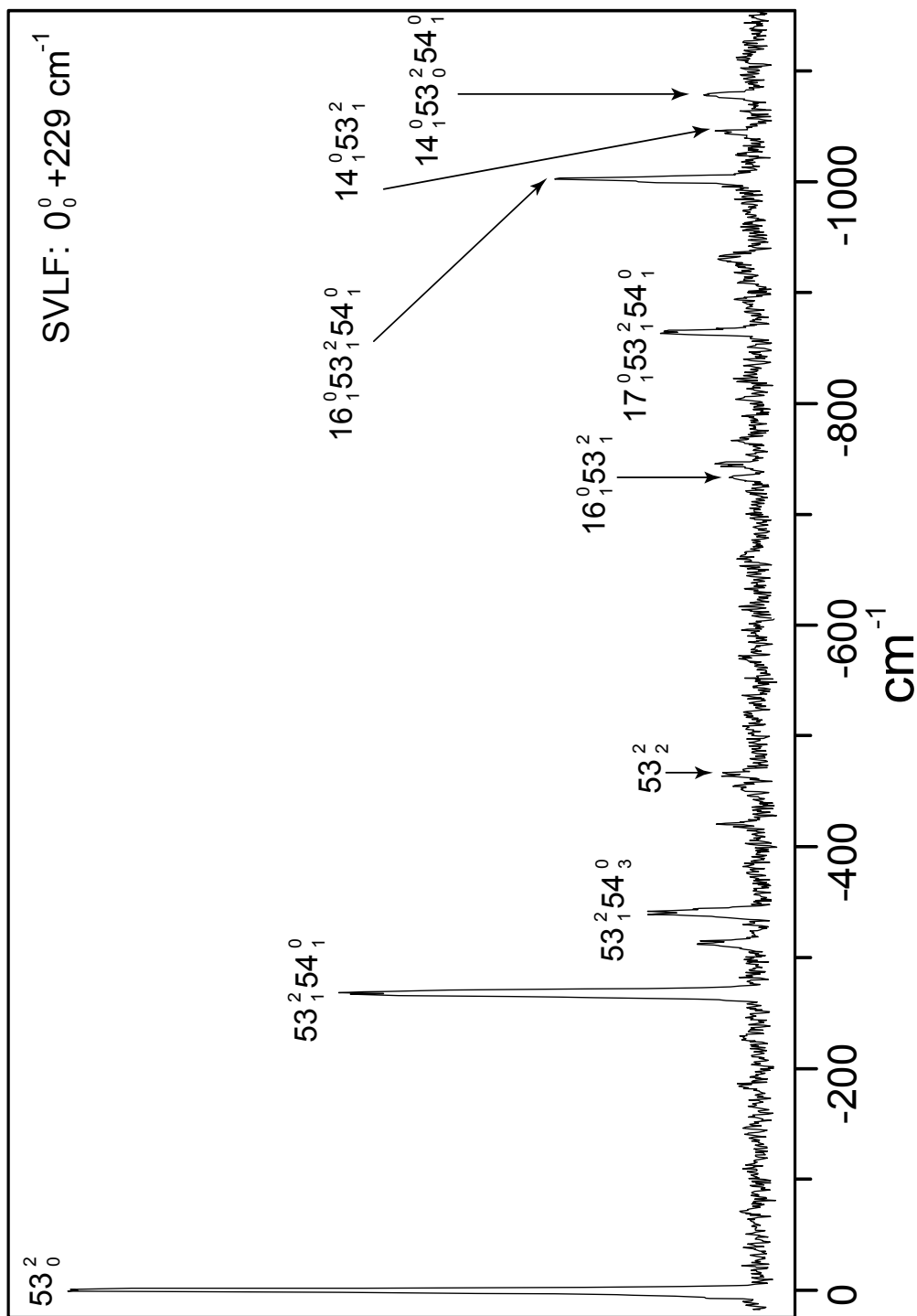


Figure 47. SVLF spectra of 14DHN from 53_0^2 excitation with some assignments.

Table 22: SVLF bands (in cm^{-1}) observed from some excitations of 14DHN^a

Excitation: 0_0^0		54_0^2		28_0^2		53_0^2	
FES bands: 0_{vvs}		+157 s		+184 m		+229 s	
-35 vvw	54_1^0 (B ₂)	-35 vvw	54_1^2				
-71 m	54_2^0 (A ₁)	-71 vvs	54_2^2				
		-112 s	54_3^2				
-148 w	28_1^0 (A ₂)	-148 vs	$28_1^0 54_0^2$				
		-157 m	54_4^2 (A ₁)				
		-187 m	$28_1^0 54_1^2$ (B ₁)	-183 vvw	$28_1^2 54_1^0$		-(148 + 35)
		-215 mw	$28_1^0 54_2^2$ (A ₂)				-(148 + 71)
-231 vvw	53_1^0 (B ₂)	-231 ms	$53_1^0 54_0^2$				
				-240 m			
-298 mw	28_2^0 (A ₁)	-268 mw	$53_1^0 54_1^2$ (A ₁)			-268 vs	$53_1^2 54_1^0$
				-298 vvs	28_2^2		
-346 w	$53_1^0 54_3^0$ (A ₁)					-315 m	?
-375 vvw	27_1^0 (A ₂)?	-375 w	$27_1^0 54_0^2$?			-341 ms	$53_1^2 54_3^0$
-453 m	18_1^0 (A ₁)	-453 mw	$18_1^0 54_0^2$ (A ₁)				
		-466 mw	$53_2^0 54_0^2$ (A ₁)			-452 vvw	$18_1^0 53_0^2$
-472 m	?					-465 w	53_2^2
-496 m	44_1^0 (B ₁)						
-596 vs	17_1^0 (A ₁)	-596 mw	$17_1^0 54_0^2$				
				-596 ms	$17_1^0 28_0^2$		
							$2 \times -(231)$

Table 22: (Continued)^a

Excitation: 0_0^0		54_0^2		28_0^2		53_0^2		
FES bands: 0 vvs		+157 s		+184 m		+229 s		
-663 m	$17_1^0 54_2^0 (A_1)$	-610 w	$18_1^0 54_4^2 (A_1)$	-661 vw	$17_1^0 53_0^2 54_2^2$	-661 vw	$17_1^0 53_0^2 54_2^2$	-453 + 157)
		-664 s	$17_1^0 54_2^2$					-596 + 71)
		-696 mw	$53_3^0 54_0^2 (B_2)$					$3 \times -(231)$
		-707 mw	$17_1^0 54_3^2$					-596 + 114)
-731 vvs	$16_1^0 (A_1)$	-732 m	$16_1^0 54_0^2$	-731 w	$16_1^0 28_0^2$	-732 vw	$16_1^0 53_0^2$	
		-738 m	$53_3^0 54_1^2 (A_1)$					-698 + 35)
-750 mw	$18_1^0 28_2^0 (A_1)$	-752 vw	$18_1^0 28_2^0 54_0^2$	-753 w	$18_1^0 28_2^2$			-453 + 298)
-772 m	$16_1^0 54_1^0 (B_2)$	-772 mw	$16_1^0 54_1^2$	-771 mw	$16_1^0 28_0^2 54_1^2$			-731 + 35)
-805 m	$16_1^0 54_2^0 (A_1)$	-806 vs	$16_1^0 54_2^2$					-731 + 71)
-843 vvw	$16_1^0 54_3^0 (B_2)$	-845 s	$16_1^0 54_3^2$					-731 + 112)
-855 m	?							
-885 w	$16_1^0 54_4^0 (A_1)$	-885 vs	$16_1^0 54_4^2$			-864 m	$17_1^0 53_1^2 54_1^0 (A_1)$	-596 + 268)
-893 w	$17_1^0 28_2^0 (A_1)$			-894 vs	$17_1^0 28_2^2$			-731 + 157)
-906 w	$18_2^0 (A_1)$							-596 + 298)
-926 m	$15_1^0 (A_1)$							
		-971 mw	$18_2^0 54_2^2 (A_1)$					-906 + 71)
-1029 w	$16_1^0 28_2^0 (A_1)$			-1029 vs	$16_1^0 28_2^2$	-1002 ms	$16_1^0 53_1^2 54_1^0 (A_1)$	-731 + 268)
								-731 + 298)

UV spectra and the energy level diagrams

The assignment of the UV data is more complicated than the assignment of all the other spectra discussed so far. Unlike FES, UV is recorded at room temperature or at elevated temperatures. Therefore, in addition to the ground vibrational level, higher levels can also be significantly populated from which the UV transitions can originate. Hence, wavenumbers measured with respect to the origin can give energies of the vibrational levels of both the ground and excited electronic states. Use of UV spectra alone may lead to many erroneous assignments because of the uncertainty of the levels from which the UV bands originate. However, with the aid of the FES and SVLF spectra, a very clear picture of the energies of the vibrational levels of the molecule can be elucidated which can give a wealth of information on the molecule.

Figure 48 shows the energy diagram which depicts the vibrational energy levels of 14DHN in its S_0 and S_1 states. This was derived by the previous assignments made using the FES, UV, SVLF, infrared and Raman spectra. The exact energies of some levels in the excited state are not determined as the excitations to these are restricted by symmetry. Therefore, approximate values for the expected frequencies are shown in parentheses. Table 23 lists the assignments of some of the bands observed in the UV spectra consistent with this energy level diagram. Although this table doesn't include a complete list of the wavenumbers of the bands observed, many peaks listed in this table are anticipated by the energy level diagram portrayed in Figure 48. This confirms that the energy level diagram presented here is accurate. The frequencies determined by UV spectra are more precise than what were determined by LIF since they have a higher resolution (0.25 cm^{-1}). In addition the wavenumbers are calibrated with respect to the He-Ne laser of the Bomem DA8.02 FT-spectrometer. Therefore, the analysis of the UV spectra definitely helps to determine the vibrational and vibronic levels more accurately. However, there are still some UV bands which remained unassigned and further analysis may be helpful.

The infrared and Raman spectra showed the presence of 12DHN as an impurity in the 14DHN sample. This was again confirmed by the UV spectra which showed

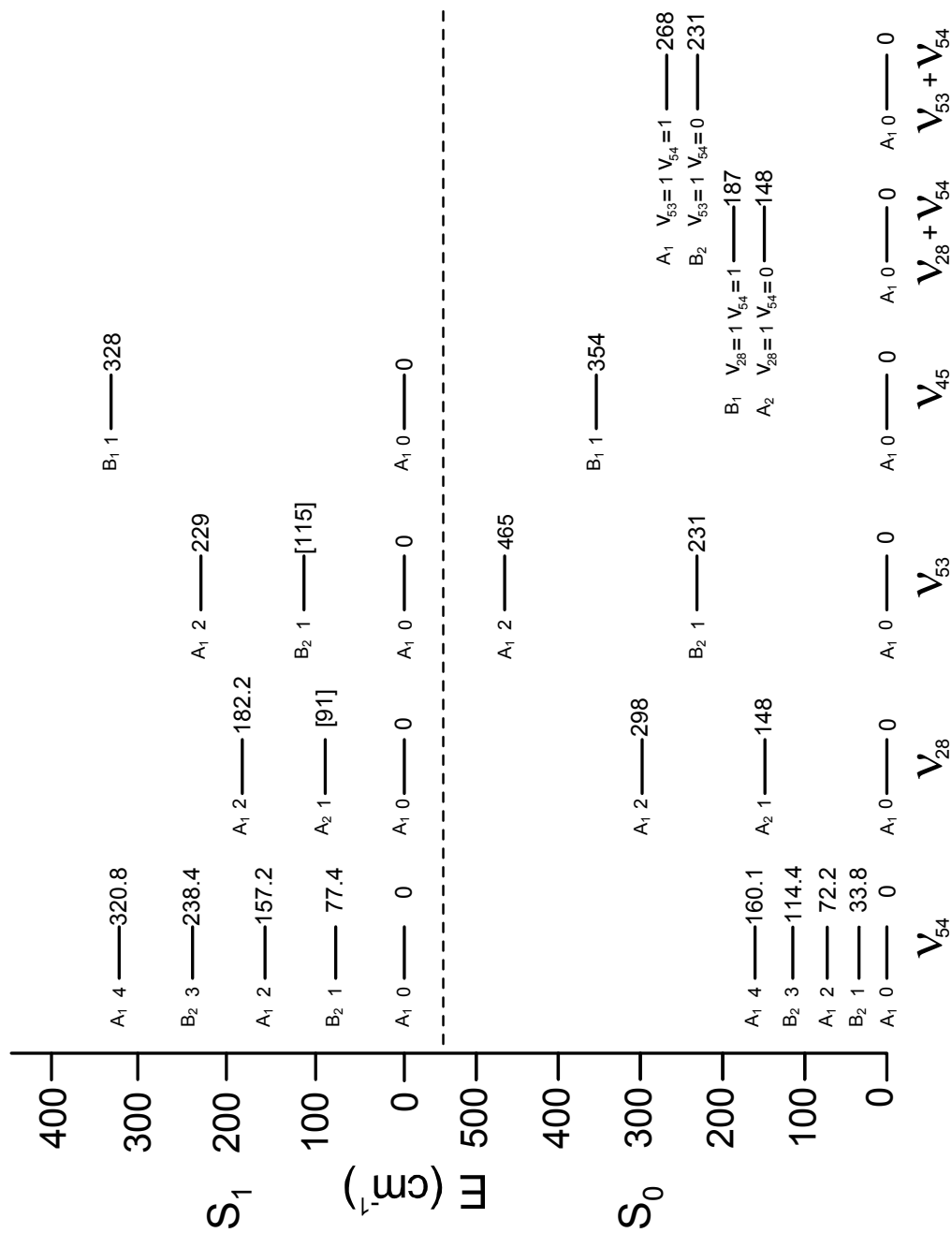


Figure 48. Energy level diagram of 14DHN which depicts the vibrational levels involving some of the low-frequency modes.

Table 23: Some selected UV bands (in cm^{-1}) of 14DHN

UV	Assignment	Inferred ^a	
-153.2 vw	$53_1^0 54_0^1$	-153.6	77.4 - 231
-142.9 ms	$28_2^0 54_0^2$	-140.8	157.2 - 298
-114.3 ms	53_1^1	(-116)	[115] - 231
-81.7 w	54_4^1	-82.7	77.4 - 160.1
-85.0 s	$28_0^2 53_0^1 54_0^1$	-85.8	182.2 - 268
-72.2 s	54_2^0		
-57.8 vs	28_1^1	(-56)	[92] - 148
-36.5 m	54_3^1	-37.0	77.4 - 114.4
-19.2 m	$28_1^1 54_1^1$	(-17.6)	[169.4] - 187
-4.1 vvw	54_4^2	-2.9	157.2 - 160.1
6.4 w	54_2^1	5.2	77.4 - 72.2
8.2 w	$53_1^0 54_0^3$	7.4	238.4 - 231
23.9 ms	$28_2^0 54_0^4$	22.8	320.8 - 298
43.7 vs	54_1^1		
77.2 s	54_0^1		
85.0 vs	54_2^2		
111.6 w	$28_0^2 54_2^0$	110.0	182.2 - 72.2
124.1 s	54_3^3		
153.4 m	$53_0^2 54_2^0$	156.8	229 - 72.2
160.2 m	54_4^4	160.7	320.8 - 160.1
237.2 ms	54_0^3	238.4	

^a inferred from the energy level diagram shown in Figure 48.

a series of very low-intense bands whose origin is at $34,093\text{ cm}^{-1}$. This value perfectly agrees with the previously reported value for the 0_0^0 band of 12DHN.⁶⁷ Since the band origins for 12DHN and 14DHN (with 0_0^0 is at $36,788.6\text{ cm}^{-1}$) are about 2700 cm^{-1} apart, the two spectra are readily distinguished.

CONCLUSIONS

Spectroscopic analysis of 14DHN using FES, SVLF, UV, infrared and Raman techniques allowed us to determine the energies of many vibrational and vibronic levels of this molecule in its ground and excited $S_1(\pi,\pi^*)$ electronic states. The DFT and *ab initio* calculations were very helpful for assigning the experimentally observed frequencies correctly. The calculated values for the excited state were especially helpful as they made it possible to assign many experimentally observed frequencies to the correct normal modes of this state. The frequencies of the ground state vibrational modes determined by infrared and Raman spectra agree very well with those observed by SVLF spectra. SVLF also determined the energies of many higher vibrational levels and also of levels arising from the combination of different modes. Many vibronic levels of the excited state also were determined by FES spectra together with UV. The present work provides a complete vibrational assignment of 14DHN molecule in both its electronic ground and singlet excited states for the first time. The identification of 12DHN impurity present in the commercial source of 14DHN may also be helpful for future research work.

CHAPTER X

STRUCTURE AND VIBRATIONAL FREQUENCIES OF 2-METHYL-2-CYCLOPENTEN-1-ONE IN ITS ELECTRONIC GROUND STATE

INTRODUCTION

2-Methyl-2-cyclopenten-1-one (2MCP) is an α,β -unsaturated ketone with a five-membered ring and a methyl group attached to it. The vibrational spectra of this molecule haven't previously been studied in detail. 2MCP was investigated by infrared and Raman spectroscopy as well as by *ab initio* and DFT calculations. Microwave studies done on the molecule 3-methyl-2-cyclopenten-1-one (3MCP) which is isomeric to 2MCP have revealed the existence of strong interaction between the ring-puckering and methyl torsion vibration.³⁴

COMPUTATIONS

The structure 2MCP was calculated using the MP2/CC-PVTZ level of theory. Vibrational frequencies together with IR and Raman intensities were calculated at the B3LYP/6-311++G(d,p) level of theory. The calculated frequencies were scaled by a factor of 0.985 for those below 1800 cm^{-1} and by a factor 0.964 for those above 1800 cm^{-1} , values found to be suitable for this level of computations from previous work.⁵⁰⁻⁵³ The symmetry of 2MCP can be either C_1 or C_s and therefore computations were carried out for both of these structures.

EXPERIMENTAL

2MCP was purchased from Aldrich and purified using vacuum transfer. The Raman spectra of 2MCP were acquired on the SA Jobin-Yvon U-1000 spectrometer. Raman scattering was achieved using a Coherent Verdi-V10 diode-pumped laser with an excitation line at 532 nm. The liquid-phase spectra were recorded at room temperature with a lasing power of 1 W. The liquid mid-infrared spectra were collected on the

Bruker Vertex 70 FT spectrometer. A total of 256 scans at 1 cm^{-1} resolution were recorded.

RESULTS AND DISCUSSION

Structure and conformations of 2MCP

The structures of 2MCP were calculated using second-order Möller-Plesset Perturbation Theory with the triple zeta basis set (MP2/CC-PVTZ). This calculation showed that the five-membered ring is planar. However it further revealed that depending upon the orientation of the methyl group, 2MCP can have three different conformations. These three conformations are shown in Figure 49. Two of these have C_s symmetry and one has no symmetry at all, i.e. C_1 . The C_1 structure was found to be the most stable. The other two structures have one of the hydrogen atoms of the methyl group lying in the plane of the ring. The $C_s(1)$ structure has this hydrogen “cis” with the carbonyl group while in the $C_s(2)$ group it is “cis” with the C=C group. The energies of the C_1 and $C_s(2)$ group are similar to each other while the $C_s(1)$ structure was about 300 cm^{-1} higher in energy. The frequency calculations for all three conformations showed that the $C_s(1)$ structure has an imaginary frequency for the methyl rotation. Therefore, this demonstrates that the conformation is not an energy minimum of the potential energy function of the internal rotation of the methyl group of 2MCP.

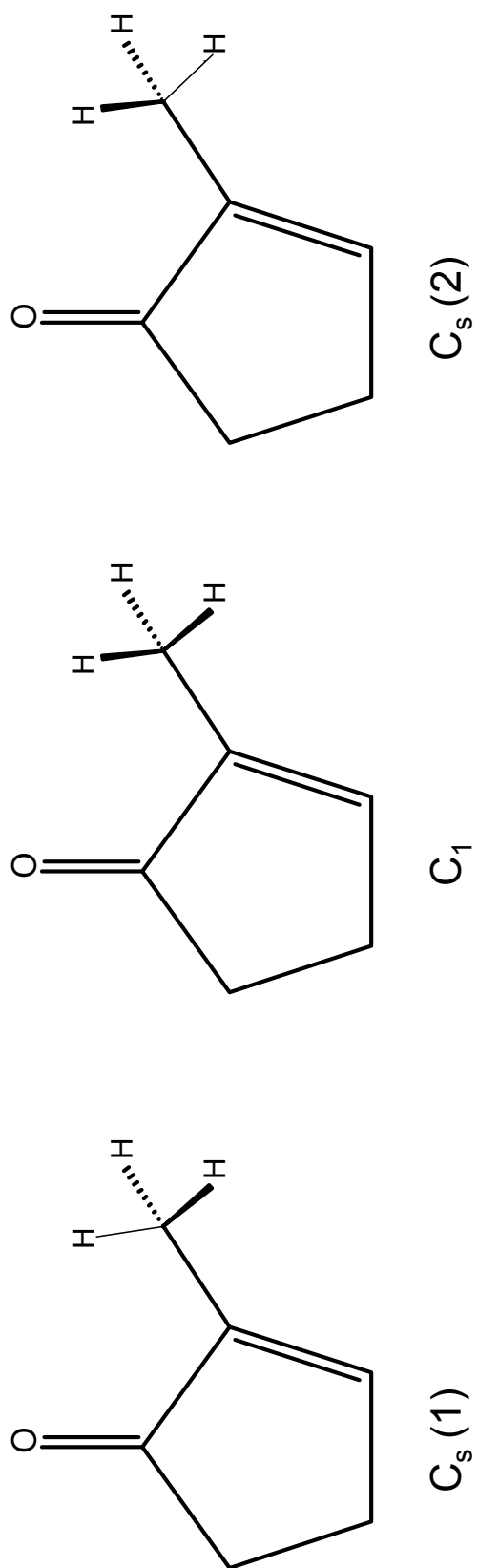


Figure 49. The three calculated conformers of 2MCP which show the orientation of the hydrogen atoms of its methyl group.

Vibrational frequencies

The vibrational frequencies and their infrared and Raman intensities were calculated for all three conformers of 2MCP using B3LYP/6-311++G(d,p) level of theory. For C_s symmetry the distribution of vibrational modes of 2MCP is

$$24A' + 15A'' \quad (10.1)$$

Figures 50 and 51 compare the liquid-phase infrared and Raman spectra of 2CHO to the calculated spectra. The agreement between the calculated and experimental frequencies and intensities is very good as also seen for other molecules discussed in previous chapters. However, since the spectra were recorded only for the liquid phase, the agreement of frequencies is not as close as what was seen for the vapor-phase spectra of other molecules. Table 24 lists the values of the experimental frequencies along with the calculated ones for the 3 conformers. The frequencies determined by infrared and Raman spectra match each other very closely but the infrared values are more accurate because they are from a FT-IR instrument which is accurately calibrated. The lowest frequency vibration (ν_{39}) was found to be the ring-bending while the methyl internal rotation is the next lowest (ν_{38}). The frequencies of these two modes are very close to each other and therefore a strong interaction between them can be expected as that was observed for 3MCP. The $C_s(1)$ conformer gives an imaginary frequency for ν_{38} . Therefore it does not correspond to an energy minimum for the internal rotation of the methyl group. The frequencies calculated for this structure are different by at least few wavenumbers for most of the normal modes from those calculated for other two conformers. This suggests that there is definitely an influence on the other vibrational modes of 2MCP by the internal rotation of methyl group, especially on the ring-bending mode (ν_{38}).

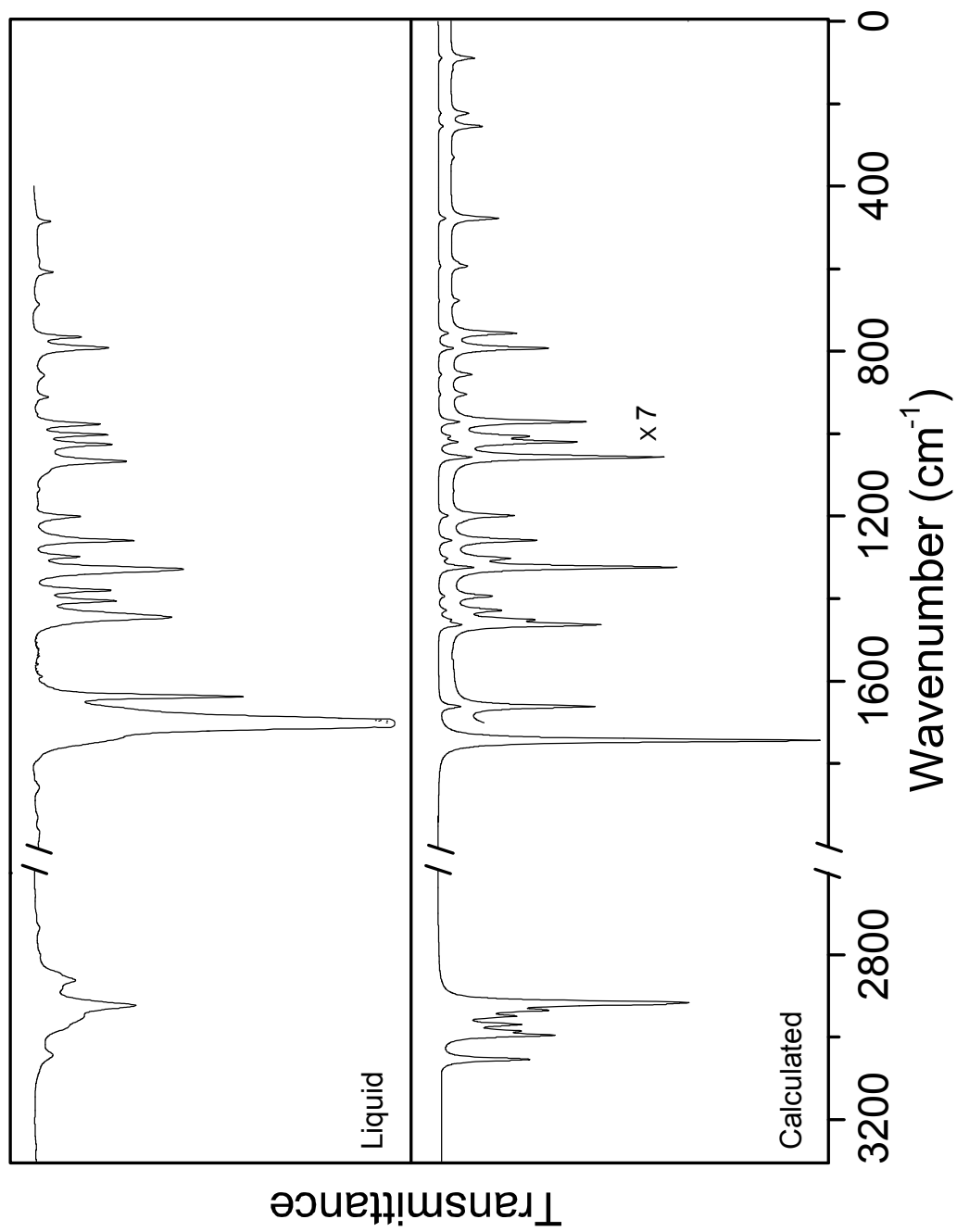


Figure 50. Liquid-phase infrared spectrum of 2MCP compared to its calculated DFT spectrum.

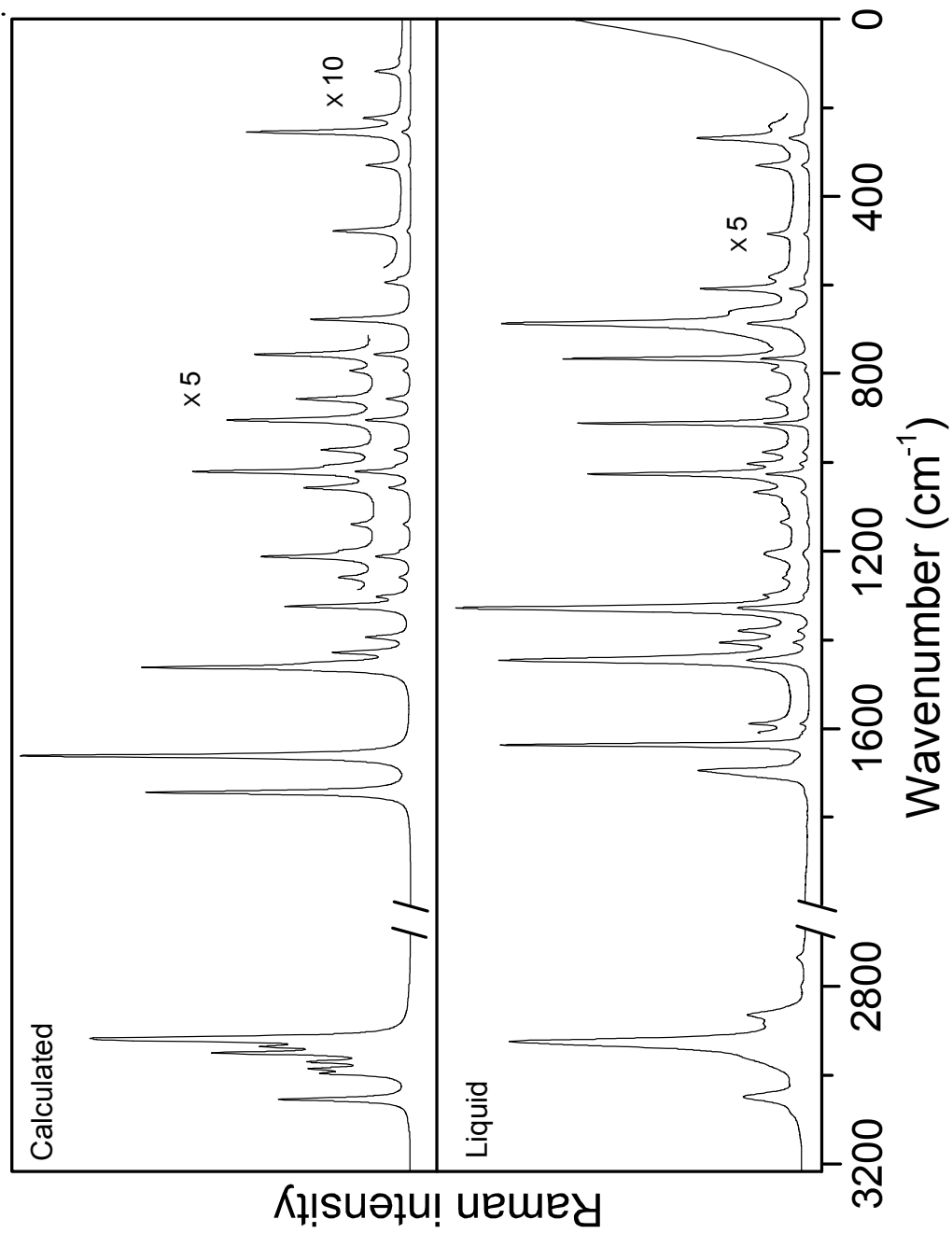


Figure 51. Liquid-phase Raman spectrum of 2MCP compared to its calculated DFT spectrum.

Table 24: Experimental and calculated vibrational frequencies (in cm^{-1}) of 2MCP^a

	Sym.		Liquid		Calculated ^b		
	C _s	C ₁	IR	Raman ^c	C _s (1)	C _s (2)	C ₁
1	A'	A	3044 m	3048 (18)	3052 (4,56)	3054 (4,58)	3054 (4,58)
2			-----	-----	3000 (1,28)	2998 (5,30)	2996 (5,31)
3			2947 sh	-----	2950 (3,74)	2950 (3,77)	2949 (3,77)
4			-----	-----	2922 (8,80)	2922 (6,83)	2921 (6,85)
5			2923 s	2923 (94)	2915 (9,100)	2916 (9,100)	2915 (9,100)
6			1700 vvs	1694 (36)	1743 (100, 73)	1743 (100, 68)	1744 (100, 68)
7			1638 m	1637 (100)	1655 (7, 100)	1662 (6, 100)	1662 (6, 100)
8			-----	-----	1465 (6, 20)	1464 (3, 60)	1464 (3, 64)
9			1445 ms	1446 (20)	1465 (2, 37)	1451 (2, 14)	1452 (3, 14)
10			-----	1406 (4)	1431 (2, 18)	1431 (2, 18)	1430 (2, 18)
11			1380 m	1379 (3)	1389 (2, 10)	1395 (2, 11)	1395 (2, 11)
12			1329 s	1328 (23)	1321 (8, 26)	1325 (9, 32)	1326 (9, 32)
13			1298 mw	1298 (2)	1305 (2, 7)	1305 (2, 7)	1304 (2, 7)
14			1260 ms	1260 (0.5)	1257 (4, 4)	1259 (3, 2)	1260 (3, 3)
15			1201 m	-----	1197 (4, 1)	1199 (3, 2)	1200 (3, 2)
16			1067 s	1066 (2)	1050 (14, 8)	1058 (9, 5)	1058 (9, 5)
17			1027 m	1026 (13)	1028 (3, 17)	1021 (5, 14)	1022 (5, 14)
18			977 m	976 (2)	977 (2, 2)	972 (5, 4)	973 (5, 4)
19			912 mw	911 (15)	907 (1, 13)	905 (1, 12)	906 (1, 11)
20			766 m	766 (16)	756 (3, 10)	757 (3, 9)	757 (3, 9)
21			686 vw	686 (19)	679 (0.3, 28)	678 (0.3, 26)	679 (0.3, 26)
22			608 w	608 (6)	599 (1, 6)	595 (1, 6)	595 (1, 6)
23			485 w	485 (2)	480 (2, 1)	479 (2, 1)	479 (2, 1)
24			-----	268 (6)	268 (2, 3)	255 (1, 2)	256 (1, 2)

Table 24: (Continued)^a

	Sym.		Liquid		Calculated ^b		
	C _s	C ₁	IR	Raman ^c	C _s (1)	C _s (2)	C ₁
25	A''	A	-----	-----	2986 (3,29)	2986 (3,34)	2985 (3,34)
26		2974 sh	-----	-----	2972 (5,32)	2969 (3,33)	2969 (3,35)
27		-----	-----	-----	2935 (4,32)	2937 (4,41)	2935 (4,44)
28		1445 ms	-----	-----	1476 (3, 14)	1466 (4,2)	1466 (3,2)
29		-----	-----	1205 (2)	1214 (0.2, 9)	1213 (0.2, 9)	1213 (0.2, 9)
30		1135 vw	-----	1134 (1)	1141 (0.03, 2)	1140 (0.04, 2)	1141 (0.1, 2)
31		-----	-----	-----	1043 (0.4, 0.4)	1052 (0.2, 0.3)	1052 (0.2, 0.3)
32		1003 m	-----	1003 (3)	1009 (2, 3)	1008 (3, 2)	1008 (3, 2)
33		858 w	-----	856 (2)	862 (1, 8)	858 (1, 6)	858 (1, 6)
34		792 ms	-----	791 (1)	795 (4, 2)	794 (4, 2)	794 (4, 2)
35		582 vw	-----	581 (1)	588 (0.2, 2)	586 (0.2, 2)	585 (0.2, 2)
36		-----	-----	330 (3)	334 (0.2, 1)	332 (0.1, 1)	331 (0.1, 0.5)
37		-----	-----	241 (2)	220 (1, 1)	223 (1, 1)	224 (1, 1)
38		-----	-----	-----	<i>i</i>	108 (0.01, 0.3)	119 (0.05, 0.4)
39		-----	-----	-----	98 (1, 0)	91 (1, 0.1)	90 (1, 0.03)

^a s-strong, m-medium, w-weak, sh-shoulder, v-very.

^b Calculated using B3LYP/6-311++G(d,p) level of theory. The values in the parentheses are relative infrared and Raman intensities respectively.

^c The values in the parenthesis are the relative Raman intensities.

CONCLUSION

This chapter discussed the conformers and the vibrational spectra of 2MCP. The theoretical calculations showed that the five-membered ring is planar, but it also revealed that depending upon the orientation of the methyl group, it can have three conformers. Two of these are very close in energy but the other lies about 300 cm^{-1} higher. The comparison of liquid-phase infrared and Raman spectra with the calculated spectra showed very good agreement between the experimental and theoretical data. Further experimental and theoretical work will be required to record the vapor phase spectra and to determine the description of each vibrational mode of 2MCP.

CHAPTER XI

CONCLUSIONS

The research work presented in this thesis focused on the investigation of structures, vibrational modes, and potential energy functions of several cyclic and bicyclic molecules in their ground and excited electronic states. A wide variety of spectroscopic and theoretical methods were utilized for this purpose.

The *ab initio* and DFT calculations carried out on 1,3-disilacyclobutane (13DSCB- h_4) and on its 1,1,3,3- d_4 isotopomer showed several highly unusual features of this molecule. First, the CSiC angles (90.0°) of the four-membered ring are larger than the SiCSi angles (87.6°) although this is opposite of expectations. Typically the force constant of the CSiC angle is much smaller than that of the SiCSi angle and hence the former should be able to accommodate the angle strain in the ring to a greater extent by lowering its value. The structure of 13DSCB determined by *ab initio* calculations showed that the partial negative charge on the carbon atoms (-0.49) of the ring is greater than the partial positive charge on the silicon atoms (+0.35). Hence, the carbon atoms will have a tendency to push each other further apart than do the silicon atoms, thereby expanding the CSiC angles. Second, the vibrational frequencies of the CH₂ wagging and twisting modes of 13DSCB are much lower than those typically observed. The calculated values for the CH₂ wagging using the B3LYP/6-311++G(d,p) level of theory are 988 and 996 cm⁻¹ for 13DSCB- h_4 and 986 and 991 cm⁻¹ for 13DSCB- d_4 . The CH₂ twisting values are 935 and 976 cm⁻¹ for 13DSCB- h_4 and 956 and 894 cm⁻¹ for 13DSCB- d_4 . These are about 200 cm⁻¹ lower than expected. The calculated structure of 13DSCB showed that the hydrogen atoms on the carbon atoms are positively charged while those on the silicon atoms are negatively charged. Therefore the attractive forces between these oppositely charged hydrogen atoms decreases the slope in the potential energy curves of the sideways motions of the CH₂ groups (i.e. twisting and wagging). This will lower the frequencies of these vibrational modes. The third unusual feature of 13DSCB is its change in structure in the solid phase. The theoretical calculations confirm the

previous conclusion that the individual molecules (vapor) have C_{2v} symmetry whereas in the solid the molecules become planar with D_{2h} symmetry. The vibrational coupling between the ring-angle bending mode and the SiH_2 in-phase rocking, which is present for the C_{2v} structure, is forbidden for D_{2h} and hence disappears.

The ring inversion potential energy functions of 2-cyclohexen-1-one (2CHO) and its 2,6,6- d_3 isotopomer (2CHO- d_3) were determined in their S_0 ground and singlet $S_1(n,\pi^*)$ electronic states using cavity ringdown spectroscopy (CRDS). The $S_1(n,\pi^*) \leftarrow S_0$ band origins for 2CHO and 2CHO- d_3 are at 26,081.3 and 26,075.3 cm^{-1} , respectively. The CRDS data allowed several of the quantum states of ν_{39} , the ring inversion vibrational mode, to be determined for both the ground and excited electronic states. The kinetic energy operator for the reduced mass calculation for the ring-inversion vibration of 2CHO was calculated by slightly modifying computer program used for 1,2-dihydronaphthalene (12DHN) molecule which has an inversion motion similar to that of 2CHO. The vibrational model assumed that the inversion vibration labeled S follows the out-of-plane displacements values calculated by density functional theory methods. The calculated kinetic functions of 2CHO are

$$g_{44}(S) = 0.03119 - 0.04782S^2 - 0.1153S^4 + 0.1490S^6 \quad (11.1)$$

for the S_0 state, and

$$g_{44}(S) = 0.03211 - 0.05834S^2 - 0.13086S^4 + 0.1490S^6 \quad (11.2)$$

for the S_1 state. These were utilized to calculate the one-dimensional potential energy functions which best fit the data. The determined potential energy functions of S_0 and S_1 electronic states of 2CHO are

$$V(cm^{-1}) = 7.459 \times 10^2 S^4 - 2.378 \times 10^3 S^2 \quad (11.3)$$

and

$$V(cm^{-1}) = 8.586 \times 10^2 S^4 - 3.493 \times 10^3 S^2 \quad (11.4)$$

respectively.

These same potential energy functions were used to fit the vibrational data of 2CHO- d_3 by adjusting the reduced mass ratio between these two isotopomers. The observed reduced mass ratios between CHO- d_3 and CHO were 1.094 for the S_0 state and 1.146 for the S_1 state. The barriers to inversion for the S_0 and $S_1(n,\pi^*)$ states were found to be 1900 ± 300 and 3550 ± 500 cm^{-1} , respectively. The DFT calculations predict barrier values of 2090 and 2265 cm^{-1} , respectively. In addition to the CRDS analysis, a complete vibrational assignment was also carried out for 2CHO and 2CHO- d_3 in its S_0 state using infrared and Raman spectroscopy which were facilitated by B3LYP/6-311++G(d,p) level of calculations. A remarkable agreement was seen between the calculated and experimental vibrational frequencies and their intensities.

The potential energy functions for the ring-puckering vibration of 1,4-dihydronaphthalene (14DHN) in its S_0 ground and singlet $S_1(\pi,\pi^*)$ electronic states were determined using laser induced fluorescence (LIF) and high-resolution ultraviolet (UV) spectra. The 0_0^0 transition observed in the UV spectra was 36,788.6 cm^{-1} . Several energy levels of the ring-puckering vibrational mode (ν_{54}) in the S_0 and S_1 states were determined by the transitions observed in LIF and UV and these data were used for the potential energy fit. The structures of 14DHN in the S_0 and S_1 states were calculated using MP2/CC-PVTZ and CIS/6-311++G(d,p) levels and these calculated structures were used to determine the kinetic energy functions for the ring puckering vibrations. These functions are

$$S_0: g_{44}(\tau) = 0.0410615 - 0.0030281\tau^2 - 0.00726122\tau^4 + 0.00535904\tau^6 \quad (11.5)$$

$$S_1: g_{44}(\tau) = 0.0406933 - 0.0033311\tau^2 - 0.00674431\tau^4 + 0.00505166\tau^6 \quad (11.6)$$

where τ is the puckering angle which is defined as the puckering coordinate. Using these functions, the potential energy functions for the two states were calculated to be

$$S_0: V(\text{cm}^{-1}) = 2.58 \times 10^2 \tau^2 + 1.31 \times 10^3 \tau^4 \quad (11.7)$$

$$S_1: V(\text{cm}^{-1}) = 2.10 \times 10^3 \tau^2 + 1.96 \times 10^3 \tau^4 \quad (11.8)$$

As shown by these functions, the energy minima correspond to puckering angles of $\tau = 0^\circ$ and the molecule has a planar equilibrium structure in both electronic states. The comparison of these two functions suggests that the molecule become more rigid in the excited state. In addition to the determination of potential energy functions, a full vibrational assignment of 14DHN was also carried out using the spectral data from LIF and UV together with infrared and Raman spectra. The calculated frequencies, especially those of the excited states were very helpful in assigning the observed frequencies to the correct vibrational mode.

The *ab initio* calculation carried out on the molecule 2-methyl-2-cyclopentenone (2MCP) showed that although the five-membered ring of this is planar, it can have three conformers depending on the orientation of the hydrogen atoms of the methyl group. Two of these conformers have a C_s symmetry while the other has C_1 symmetry. The conformer with C_1 symmetry was found to be the most stable. One of the C_s conformers has a methyl group hydrogen atom “cis” with the C=C group while in the other, this hydrogen atom is “cis” with the carbonyl group. The energy of the former was comparable to the C_1 conformer while the other one is about 300 cm^{-1} higher in energy. The frequency calculations were carried out on all three conformers using B3LYP/6-311++G(d,p) level of theory. These were compared with the experimental frequencies determined by liquid-phase infrared and Raman spectroscopy. There was good agreement between the experimental and the calculated values for the stable conformer.

REFERENCES

1. Carreira, L. A.; Lord, R. C.; Malloy Jr., T. B. *Topics in Current Chemistry* **1979**, *82*, 1-95.
2. Laane, J.; Lord, R. C. *J. Chem. Phys.* **1967**, *47*, 4941-4945.
3. Laane, J.; Lord, R. C. *J. Mol. Spectrosc.* **1971**, *39*, 340-344.
4. Bell, R. P. *Proc. R. Soc. London, Ser. A* **1945**, *183*, 328-337.
5. Danti, A.; Lafferty, W. J.; Lord, R. C. *J. Chem. Phys.* **1960**, *33*, 294-295.
6. Borgers, T. R.; Stauss, H. L. *J. Chem. Phys.* **1966**, *45*, 947-955.
7. Laane, J.; Lord, R. C. *J. Chem. Phys.* **1968**, *48*, 1508-1513.
8. Miller, F. A.; Capwell, R. J. *Spectrochim. Acta A* **1971**, *27*, 947-956.
9. Laane, J. *J. Quart. Rev.* **1971**, *25*, 533-553.
10. Laane, J. *J. Pure and Appl. Chem.* **1987**, *59*, 1307-1326.
11. Laane, J. In *Structures and Conformations of Non-Rigid Molecules*; Laane, J.; Dakkouri, M.; van der Veken, B.; Oberhammer, H., Eds.; Elsevier: Amsterdam, 1993; Chapter 4.
12. Laane, J. *J. Annu. Rev. Phys. Chem.* **1994**, *45*, 179-211.
13. Laane, J. *J. Intl. Rev. Phys. Chem.* **1999**, *18*, 301-341.
14. Laane, J. *J. Phys. Chem. A* **2000**, *104*, 7715-7733.
15. Irwin, R. M.; Cooke, J. M.; Laane, J. *J. Am. Chem. Soc.* **1977**, *99*, 3273-3278.
16. Kubota, T.; Ueda, K.; Tanaka, T.; Laane, J. *J. Mol. Spectrosc.* **1988**, *128*, 250-267.
17. Kubota, T.; Ueda, K.; Tanaka, T.; Laane, J. *J. Mol. Spectrosc.* **1985**, *114*, 234-235.
18. Irwin, R. M.; Laane, J. *J. Phys. Chem.* **1978**, *82*, 2845-2850.
19. Chao, T. H.; Laane, J. *J. Mol. Spectrosc.* **1973**, *48*, 266-276.
20. Cheatham, C. M.; Laane, J. *J. Chem. Phys.* **1991**, *94*, 7734-7743.
21. Pillsbury, N. R.; Choo, J.; Laane, J.; Drucker, S. *J. Phys. Chem. A* **2003**, *107*, 10648-10654.
22. Manley, S. A.; Tyler, J. K. *Chem. Commun.* **1970**, pp 382-383.

23. Carreira, L. A.; Towns, T. G.; Malloy Jr., T. B. *J. Chem. Phys.* **1979**, *70*, 2273-2275.
24. Smithson, T. L.; Wieser, H. *J. Chem. Phys.* **1980**, *73*, 2518-2519.
25. Oberhammer, H.; Bauer, S. H. *J. Am. Chem. Soc.* **1969**, *91*, 10-16.
26. Strube, M. M.; Laane, J. *J. Mol. Spectrosc.* **1988**, *129*, 126-139.
27. Shin, Y.-D.; Saigusa, H.; Zgierski, M. Z.; Zerbetto, F.; Lim, E. C. *J. Chem. Phys.* **1991**, *94*, 3511-3516.
28. Rabideau, P. W. *Acc. Chem. Res.* **1978**, *11*, 141-147.
29. Rabideau, P. W.; Mooney, J. L.; Hardin, J. N. *J. Org. Chem.* **1985**, *50*, 5737-5740.
30. Lipkowitz, K. B.; Rabideau, P. W.; Raber, D. J.; Hardee, L. E.; Schleyer, P. R.; Kos, A. J.; Kahn, R. A. *J. Org. Chem.* **1982**, *47*, 1002-1005.
31. Rabideau, P. W.; Dhar, R. K.; Fronczek, F. R. *Chem. Commun.* **1992**, pp 79-80.
32. Schaefer, T.; Sebastian, R.; Hruska, F. E.; *J. Chem. Phys.* **1992**, *96*, 1653-1654.
33. Chakraborty, T.; Del Bene, J. E.; Lim, E. C. *J. Chem. Phys.* **1993**, *98*, 8-13.
34. Palaez, F. J.; Lopez, J. C.; Alonso, J. L. *J. Mol. Struct.* **1987**, *159*, 19-29.
35. Haller, K.; Chiang, W.-Y.; del Rosario, A.; Laane, J. *J. Mol. Struct.* **1996**, *379*, 19-29.
36. O'Keefe, A.; Deacon, D. A. G. *Rev. Sci. Instrum.* **1988**, *59*, 2544-2551.
37. Scherer, J. J.; Paul, J. B.; O'Keefe, A.; Saykally, R. J. *Chem. Rev.* **1997**, *97*, 25-51.
38. Busch, K.; Busch, M. *Cavity Ring-down Spectroscopy. An Ultratrace-Absorption Measurement Technique*; ACS Symposium series (Vol. 720): 1999.
39. Berden, G.; Peeters, R.; Meijer, G. *Int. Rev. Phys. Chem.* **2000**, *19*, 565-607.
40. Foresman, J. B.; Frisch, A. *Exploring Chemistry with Electronic Structure Methods*, 2nd ed.; Gaussian Inc: Pittsburgh, 1996.
41. Cramer, C. J. *Essentials of Computational Chemistry*; John Wiley: West Sussex, 2002.
42. Jensen, F. *Introduction to Computational Chemistry*, 2nd ed.; John Wiley: West Sussex, 2007.

43. Labanowski, J. K.; Andzelm, J. W. *Density Functional Methods in Chemistry*; Springer-Verlag: New York, 1991.
44. Hassanein, A. A.; Evans, M. W. *Computational Methods in Quantum Chemistry*, Quantum Chemistry; World Scientific Publishing Co: Singapore, 1996; Vol. 2.
45. Frisch, M. J.; Trucks, G. W.; Schlegel, H. B.; Scuseria, G. E.; Robb, M. A.; Cheeseman, J. R.; Montgomery, Jr., J. A.; Vreven, T.; Kudin, K. N.; Burant, J. C.; Millam, J. M.; Iyengar, S. S.; Tomasi, J.; Barone, V.; Mennucci, B.; Cossi, M.; Scalmani, G.; Rega, N.; Petersson, G. A.; Nakatsuji, H.; Hada, M.; Ehara, M.; Toyota, K.; Fukuda, R.; Hasegawa, J.; Ishida, M.; Nakajima, T.; Honda, Y.; Kitao, O.; Nakai, H.; Klene, M.; Li, X.; Knox, J. E.; Hratchian, H. P.; Cross, J. B.; Bakken, V.; Adamo, C.; Jaramillo, J.; Gomperts, R.; Stratmann, R. E.; Yazyev, O.; Austin, A. J.; Cammi, R.; Pomelli, C.; Ochterski, J. W.; Ayala, P. Y.; Morokuma, K.; Voth, G. A.; Salvador, P.; Dannenberg, J. J.; Zakrzewski, V. G.; Dapprich, S.; Daniels, A. D.; Strain, M. C.; Farkas, O.; Malick, D. K.; Rabuck, A. D.; Raghavachari, K.; Foresman, J. B.; Ortiz, J. V.; Cui, Q.; Baboul, A. G.; Clifford, S.; Cioslowski, J.; Stefanov, B. B.; Liu, G.; Liashenko, A.; Piskorz, P.; Komaromi, I.; Martin, R. L.; Fox, D. J.; Keith, T.; Al-Laham, M. A.; Peng, C. Y.; Nanayakkara, A.; Challacombe, M.; Gill, P. M. W.; Johnson, B.; Chen, W.; Wong, M. W.; Gonzalez, C.; Pople, J. A. Gaussian 03, Revision C.02; Gaussian, Inc., Wallingford CT, 2004.
46. Laane, J.; Harthcock, M. A.; Killough, P. M.; Bauman, L. E.; Cooke, J. M. *J. Mol. Spectrosc.* **1982**, *91*, 286-299.
47. Schmude, R. W., Jr., Harthcock, M. A.; Kelly, M. B.; Laane, J. *J. Mol. Spectrosc.* **1987**, *124*, 369-378.
48. Tecklenburg, M. M.; Laane, J. *J. Mol. Spectrosc.* **1989**, *137*, 65-81.
49. Irwin, R. M.; Ph.D. Thesis, Texas A&M University, College Station, TX, 1978.
50. Yang J.; McCann K.; Laane J. *J. Mol. Struct.*, **2004**, *695-696*, 339-343.
51. Autrey, D.; Haller, K.; Laane, J.; Mlynek, C.; Hopf, H. *J. Phys. Chem. A*, **2004**, *108*, 403-408.

52. Autrey D.; Yang J.; Laane J. *J. Mol. Struct.*, **2003**, 661-662, 23-32.
53. Al-Saadi, A. A.; Laane, J. *J. Mol. Struct.* **2007**, 830, 46-57.
54. Lin-Vien, D.; Colthup, N. B.; Fateley, W. G.; Grasselli, J. G. *Infrared and Raman Characteristic Frequencies of Organic Molecules*; Academic Press: San Diego, 1991; pp 23 and 257.
55. Seidl, E. T.; Grev, R. S.; Schaefer III, H. F.; *J. Am. Chem. Soc.*, **1992**, 114, 3643-3650.
56. Walsh, A. D. *J. Chem. Soc.* **1953**, pp 2260-2266.
57. Brand, J. C. D., *J. Chem. Soc.* **1956**, pp 858-872.
58. Wilsey, S.; González, L.; Robb, M. A.; Houk, K.N. *J. Am. Chem. Soc.* **2000**, 122, 5866-5876.
59. Fang, W.-H. *Chem. Phys. Lett.* **2000**, 325, 683-692.
60. Johansson, P.; Tegenfeldt, J.; Lindgren, J. *J. Phys. Chem. A*, **2000**, 104, 954-961.
61. Guirgis, G. A.; Horn, A.; Klæboe, P.; Nielsen, C. J. *J. Mol. Struct.* **2006**, 825, 101-114.
62. Sundaraganesan, N.; Anand, B.; Joshua, B. D. *Spectrochimica Acta, A* **2007**, 67, 550-558.
63. GaussView, Version 3.09, Roy Dennington II, Todd Keith, John Millam, Ken Eppinnett, W. Lee Hovell, and Ray Gilliland, Semichem, Inc., Shawnee Mission, KS, 2003.
64. Nam, S. I.; Min, E. S.; Jung, Y. M.; Lee, M. S. *Bull. Korean Chem. Soc.* **2001**, 22, 989-993.
65. Choo, J.; Kim, S.; Drucker, S.; Laane, J. *J. Phys. Chem. A* **2003**, 107, 10655-10659.
66. Autrey, D.; Choo, J.; Laane, J. *J. Phys. Chem.*, **2001**, 105, 10230-10236.
67. Autrey, D.; Arp, Z.; Choo, J.; Laane, J. *J. Chem. Phys.*, **2003**, 119, 2557-2568.
68. (a) Turro, N. J. *Modern Molecular Photochemistry*; Benjamin/Cummings: Menlo Park, CA, 1978; Chapter 10-12. (b) Schuster, D. I; Lem, G.; Kaprinidis, N. A. *Chem. Rev.* **1993**, 93, 3-22.

69. García-Expósito, E.; Bearpark, M. J.; Ortuño, R. M.; Robb, M. A.; Branchadell, V. *J. Org. Chem.* **2002**, *67*, 6070-6077.
70. Reguero, M.; Olivucci, M.; Bernardi, F.; Robb, M. A. *J. Org. Chem.* **1997**, *62*, 6897-6902.
71. Zimmerman, H. E.; Nesterov, E. E. *J. Am. Chem. Soc.*, **2003**, *125*, 5422-5430.
72. Laane, J.; Takahashi, H.; Bandrauk, A. (eds.), *Structure and Dynamics of Electronic Excited States*; Springer: Berlin, Germany, 1999; pp 3-35.
73. Sakurai, S.; Meinander, N.; Morris, K.; Laane, J. *J. Amer. Chem. Soc.* **1999**, *121*, 5056-5062.
74. Sakurai, S.; Bondoc, E.; Laane, J.; Morris, K.; Meinander, N.; Choo, J. *J. Amer. Chem. Soc.* **2000**, *122*, 2628-2634.
75. Bondoc, E.; Sakurai, S.; Morris, K.; Chiang, W.-Y.; Laane, J. *J. Chem. Phys.*, **2000**, *112*, 6700-6706.
76. Arp, Z.; Laane, J.; Sakamoto, A.; Tasumi, M. *J. Phys. Chem.*, **2002**, *106*, 3479-3484.
77. Arp, Z.; Meinander, N.; Choo, J.; Laane, J.; *J. Chem. Phys.* **2002**, *116*, 6648-6655.
78. Yang, J.; Wagner, M.; Okuyama, K.; Arp, Z.; Choo, J.; Meinander, N.; Kwon, O.; Laane, J. *J. Chem. Phys.* **2006**, *125*, 034308.
79. Yang, J.; Wagner, M.; Laane, J. *J. Phys. Chem. A* **2006**, *110*, 9805-9815.
80. Yang, J.; Laane, J. *J. Mol. Struct.* **2006**, *798*, 27-33.

VITA

Name: Mohamed Zuhair Mohamed Rishard

Country of Citizenship: Sri Lanka

Permanent Address: No. 808, Aluthmawatha Road
Colombo-15, Sri Lanka

E-mail Address: rishiz74@yahoo.com

Marital Status: Married with one child

Education: B.Sc., Chemistry, University of Colombo
Colombo, Sri Lanka, May 2000

Ph.D., Chemistry, Texas A&M University
College Station, TX 77843, December 2007